2d DI-HADRON CORRELATION AT $\sqrt{S_{NN}} = 200$ GeV USING THE STAR EXPERIMENT

A Dissertation

Presented to

the Faculty of the Department of Physics

University of Houston

In Partial Fulfillment

of the Requirements for the Degree

Doctor of Philosophy

By

Lindamulage Chanaka De Silva

December 2012

2d DI-HADRON CORRELATION AT $\sqrt{S_{NN}} = 200$ GeV

USING THE STAR EXPERIMENT

Lindamulage Chanaka De Silva

APPROVED:

Prof. Rene Bellwied, Chairman
Dept. of Physics

Prof. Lawrence S. Pinskey
Dept. of Physics

Prof. Ed Hungerford
Dept. of Physics

Prof. Donald Kouri
Dept. of Physics

Prof. Carlos Ordonez
Dept. of Physics

Dean, College of Natural Sciences and Mathematics

Acknwoledgements

This dissertation marks the end of a twelve-year journey of pursuing a goal which was cultivated in my mind during high school time period. It was none other than graduating with a Ph.D in physics. I could have never reached the heights and explored the depths without the support, guidance and efforts of lot of people. My dream of achieving a physics Ph.D was initiated by reading an excellent book call "Matter and Radiation" by Dr. S.R.D. Rosa from the University of Colombo Sri Lanka.

My deepest gratitude goes first and foremost to the academic and non-academic staff in the department of physics, University of Colombo, Sri Lanka and especially to Dr. G. Bandarage from the Open University of Sri Lanka for making me more enthusiastic about physics. Arriving in the USA with a full graduate scholarship from the Wayne State University would have been only a dream without your support.

Seeing Prof. Rene Bellwied's Heavy ion Group's research website made me choose Wayne State University over other three graduate colleges that offered me scholarships in USA. Right after his seminar for new graduate students I talked with Rene for the first time back in 2006. Our conversation wasn't that of a success. It led me to think that I won't be able to talk to him ever again until he showed up at the 2006 physics Christmas party, which was our second meeting. The outcome of the second meeting was what made me more excited about achieving my goal. I cherish every bit of that discussion we had simply because he is an advisor that any graduate student would love to have. He is a mentor, a good friend and a person who is down to earth which makes him a lovable person among us. His ideas and suggestions

were always insightful, valuable and useful. I thank Rene for the scientific insight he cultivated in me, which I hope will escalate in the years to come and for all the opportunities he provided me through out my graduate student life to grow as an independent scientist. I want to thank you again for trusting and investing in me. Indeed I can be happy for the fact that we narrowed down on η/s in the QGP and I will do my best to deduce a value for the jet energy transport coefficient before we finish our PRC paper.

Further, I wish to express my sincere appreciation to to the STAR collaboration and it's colleagues. I had a pleasant environment to work as a graduate student at all times. It was absolutely awe-inspiring. The Wayne State heavy ion group was a pleasure to work with. I have to mention that I really enjoyed the company of Claude, Sergei, Sean, Anthony, Sarah, Monika, Larry, and everyone during my stay at Wayne State. I would also like to express my gratitude to my physics working group (jet correlations) and other collaborators for every single discussion we had. It was those discussions that laid the foundation for my current understanding of QCD and standard model physics.

I would like to express my heartfelt thanks to back bone of my work, my family for their continued support and enthusiasm during the period of study. Many thanks to you, My Mother and Father, for the utmost support given to me through out my journey being a physicist. Without you both I would have not existed and without your love and kindness I would have never succeeded in my life. Thank you for having faith in my abilities what has shaped me to be the person I am today. I hope this dissertation brings you happiness and pride, as much as it does for me.

Thank you my loving little wife, Ishani, for coming into my life and sharing your love with me. I am forever thankful for how understanding you are and being supportive during my final semester as a graduate student, ♡. At last, a huge thank you to all my Sri Lankan friends from Wayne State University to University of Houston, my teachers from kindergarten to high school, my relatives, in-laws, all my friends, colleagues and everyone in Sri Lanka for their advices, comments, companionship, love, support, understanding, and helping me in every way to achieve my goal!! I am blessed to have such an amazing team of people to assist me with my dissertation. Deepest gratitude to everyone! Thank You!

2d DI-HADRON CORRELATION AT $\sqrt{S_{NN}} = 200$ GeV USING THE STAR EXPERIMENT

An Abstract of a Dissertation

Presented to

the Faculty of the Department of Physics

University of Houston

In Partial Fulfillment

of the Requirements for the Degree

Doctor of Philosophy

By

Lindamulage Chanaka De Silva

December 2012

Abstract

The Relativistic Heavy Ion Collider (RHIC) at Brookhaven National Lab (BNL) in Long Island, New York, attempts to recreate the initial conditions at the birth of our universe. Heavy Au_{79}^{197} ions are accelerated up to 0.99995c and collided at $\sqrt{S_{NN}} = 200\ GeV$ (center of mass energy per nucleon) in order to recreate the initial moments ($\sim 10^{-6}s$) after the Big Bang. The theory of Quantum Chromo Dynamics (QCD) predicts the formation of a primordial nuclear matter phase know as Quark Gluon Plasma (QGP) under these experimental conditions. This dissertation focuses on studying this QCD medium using data from the Solenoidal Tracker At RHIC (STAR) detector.

The study of two-dimensional two-particle correlations of emitted charged particles contains valuable time integrated information of the dynamical QCD medium. Long range correlations between particles in angular and momentum space generally can be attributed to collective behavior not found in a superposition of elementary collisions. The focus of this thesis is to understand a novel, long-range correlation structure observed in pseudo-rapidity ($\Delta\eta$) as a function of $<p_T>$. Data from $\sqrt{S}$ = 200 GeV AuAu collisions are confronted with CuCu and pp collisions at the same energy to establish system size dependence. The interpretation is based on empirical models describing well established hydrodynamical collective flow phenomena and possible novel phenomena related to in medium parton fragmentation. The parameters extracted from the model fit can be used to constrain medium properties such as the initial gluon density, the shear viscosity and the partonic energy transport coefficient.

Contents

List of Figures

List of Tables

Chapter 1

Introduction to relativistic heavy ion collisions

History teaches us that human kind always wondered and explored to answer the question, "what is the physical world made of?". From the time of the ancient Greek philosophers to this day, human kind have advanced in their knowledge in answering this question. In ancient time, Greek philosopher Aristotle classified that the surrounding is composed of four main elements; earth, water, fire, and air [1]. This classification was based on observing the basic properties of matter that surrounds us. This observation process evolved as a scientific method with time and at present day we understand "quarks" and "leptons" are the basic building blocks of matter [2]. As our horizon in science expands, we also question the origin of the universe we live in. Present day science studies the Big Bang model in order to understand the universe evolution [3]. The scientists at the Relativistic Heavy Ion Collider (RHIC)

have built a machine that enables us to study the initial moments of the birth of our universe [4].

1.1 Early universe and evolution of matter

The most contemporary scientific studies have found evidence to support the Big Bang model, which predicts that the entire universe had an absolute beginning and originated from a Plank-scale quantum fluctuation followed by inflation and successive expansion. The main evidence for such a model is the Cosmic Microwave Background Radiation (**CMBR**) and cosmological red shift measurements.

1.1.1 Cosmic microwave background radiation

CMBR is thermal radiation which is the strongest in microwave range, detected in the space between stars and galaxies using sufficiently sensitive radio telescopes. This Nobel prize-winning search was carried out in 1964 by two American radio astronomers Penzias and Wilson. The following figure 1.1 is a recent measure of temperature anisotropies in **CMB** based on the **W**ilkinson **M**icrowave **A**nisotropy **P**robe (**WMAP**).

Anisotropy information is used to measure the universe's geometry, content and evolution. These measurements enable scientists to verify the Lambda-CDM model, which is the standard model of inflationary Big Bang theory (Fig 1.2). Scientists have discovered that **CMB** radiation is well explained as radiation left over from

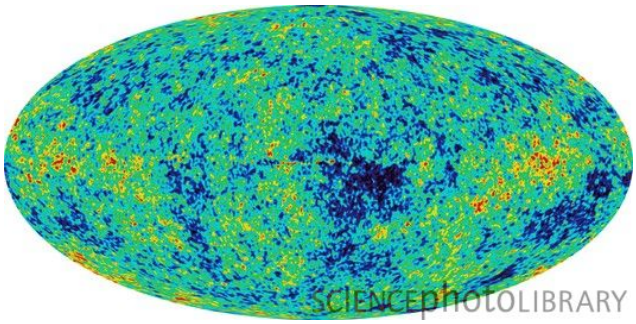

Figure 1.1: WMAP measurement of the present-day universe.

initial stages in the development of the universe [5].

1.1.2 Cosmological red shift

The successive evolution after cosmic inflation in the Big Bang model predicts a perpetually expanding universe. The observed Hubble expansion, which is also known as cosmological red shift, provides strong evidence to such a model as shown below (Fig 1.3).

As seen in Fig 1.3, if the light (electromagnetic radiation) received by the observer falls out of the visible spectrum (yellow) the source emitting the electromagnetic radiation is either moving away or towards the observer. As explained in the Doppler effect, the light will be blue in color if the source is moving towards and red in color if it is moving away from the observer. The observed cosmic microwaves from distance galaxies are "red shifted" and therefore move away from us. This observation is summed up in the Hubble law which states that the space time volume of the observed universe is expanding [6].

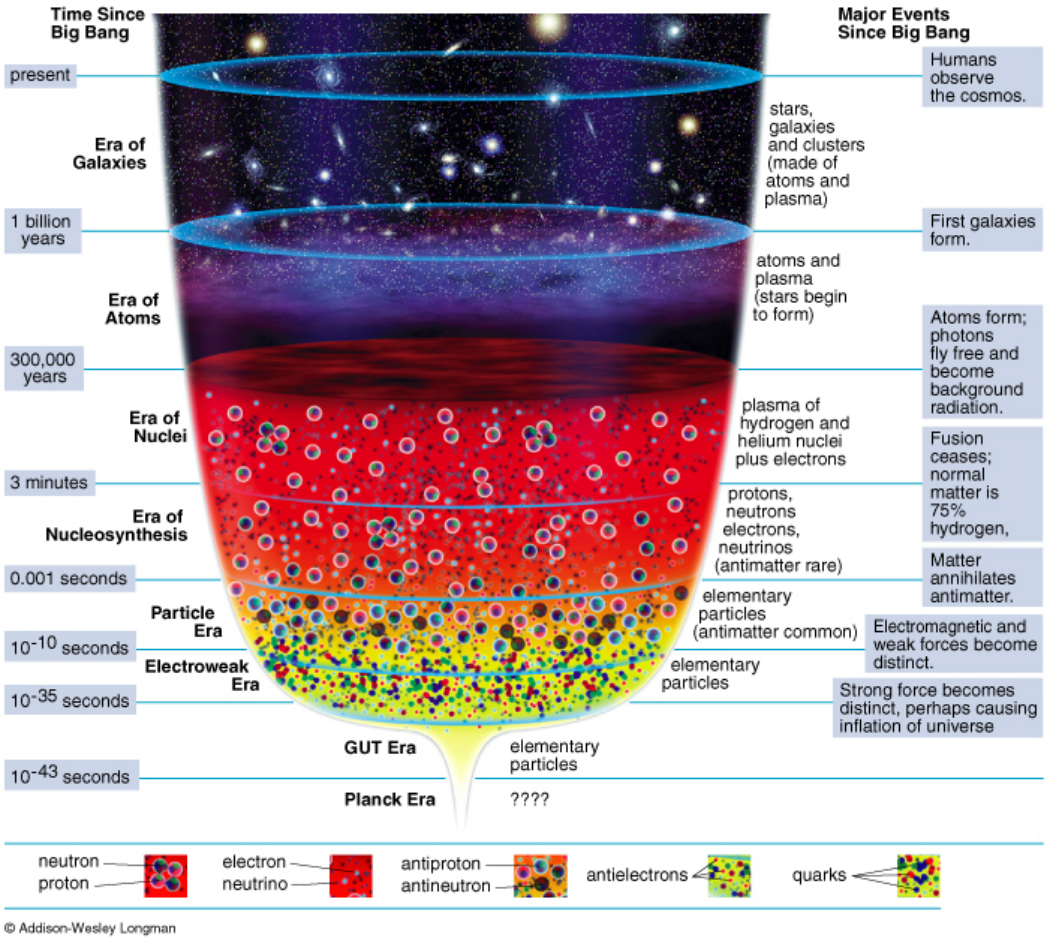

Figure 1.2: Big Bang model [166].

1.2 The symmetries of nature and Quantum Chromo Dynamics (QCD)

Projecting back in time according to Big Bang theory, the initial conditions of our present day universe existed around 13.7 billion years ago. Tracing down the expansion tells us that the initial "singularity" contained in an infinitesimal volume baring

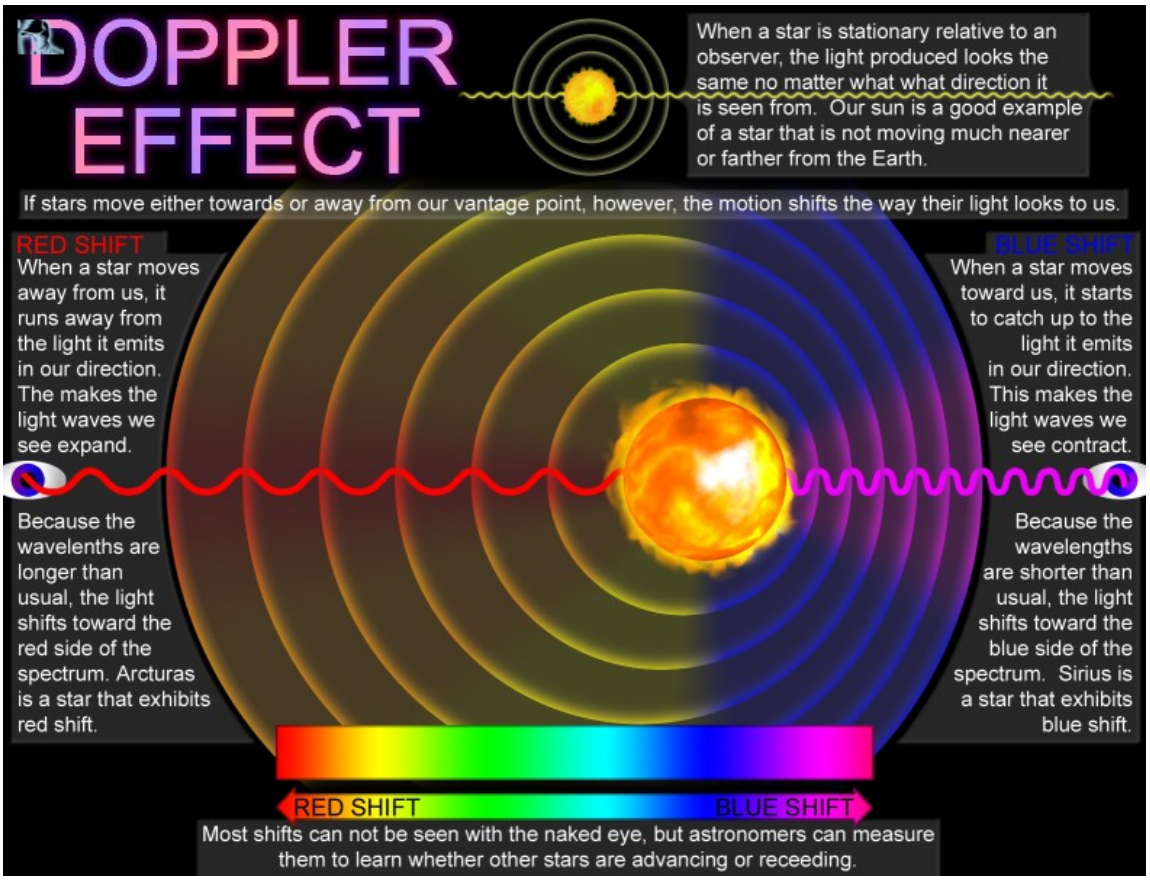

Figure 1.3: Cosmological red shift explained [167].

infinite temperatures and densities. A rapid expansion also known as cosmic inflation occurred from this initial state as a result of its cooling down [7, 8]. The closest we can get to this singularity is the end of Plank epoch which is $\sim 10^{-43}s$ after the Big Bang (see Fig 1.2). During this epoch, all four fundamental forces of nature we observe today were unified as one force and quantum effects of gravity were significant. This unstable or transitory hot dense initial state evolved giving rise to fundamental forces we observe today via a process known as symmetry breaking. As of today, we understand that such symmetry breaking processes took place successively giving

rise to the Grand unification epoch, the cosmic inflationary epoch and the rest of the Big Bang evolution that resulted in the present state of the universe [9].

1.2.1 Symmetries and symmetry breaking

The property of symmetry is associated with an observable quantity of a system. Symmetry guarantees that the observed quantity does not change (invariant) under a specific transformation. Noether's theorem further tells us that there is a conserved quantity associated with each symmetry of a physical system (*e.g.: Linear momentum conservation arises due to invariance of translation in space*). The transformations can be either discrete or continuous and mathematical groups can be associated for transformations (e.g.: Lie groups for continuous transformations). A breaking of a particular symmetry of a physical system arises due to critical infinitesimal fluctuations acting on a system. As a result, the system transforms in to a different state. Such transitions bring a system from a disordered state in to one of the two definite states, thus known as a symmetry breaking.

1.2.2 Spontaneous symmetry breaking and gauge theory

In Big Bang cosmology, what is important to us is the spontaneous symmetry breaking phenomenon. Spontaneous symmetry breaking processes keep the laws which describe the system invariant, but the system itself is not invariant. This is because what surrounds the system in question is a vacuum which is non invariant. Spontaneous symmetry breaking is parametrized by an order parameter. Moreover, in Big

Bang cosmology, the underlying transformations are between different field configurations that results in an observable quantity. As mentioned earlier, if the observed quantity is unchanged for different underlying field configurations (*not directly observed*), then the system preserves the symmetry under that specific transformation. In physics, we name such symmetries as gauge symmetries (gauge invariance), transformations as gauge transformations and the relevant theory as gauge theory. With the development of quantum field theory, scientists realized that fundamental interactions of nature arise from *local gauge symmetry* constraints. In the case of local gauge symmetries, transformations vary from point to point in space and time. Also in gauge theory, the Lagrangian of a system is invariant under a continuous group of local gauge transformations.

1.2.3 Gauge fields and standard model in physics

The Lagrangian of a system contains a certain number of degrees of freedom. Gauge can also be understood as the redundant number of degrees of freedom in a Lagrangian. Interestingly, the transformations between such gauges in a system forms a continuous mathematical group called a Lie group. This gauge group (*or symmetry group*) is associated to its group of generators through group algebra and each generator necessarily corresponds to a vector field which is named as the gauge field corresponding to that generator. The Lagrangian contains gauge fields in order to preserve the invariance under local gauge transformations. Quantized forms of gauge fields are known as gauge bosons. The gauge theory is called abelian or non-abelian depending on whether the symmetry group is commuting or non-commuting. The

present day standard model resembles a non-abelian gauge theory with the symmetry group **U(1)**x**SU(2)**x**SU(3)**. **U(1)** represents an abelian gauge theory which describes the electromagnetic field(interaction). **SU(2)** is a non abelian gauge theory describing the weak interaction. Finally **SU(3)** also a non abelian gauge theory describing the strong interaction. Those fields give rise to the gauge bosons: a photon, 3 weak bosons and 8 gluons respectively. In my thesis work, I will be focusing mainly on the the **SU(3)** non abelian gauge symmetry group which originates **QCD**. The following subsections will discuss briefly the strong interaction and how we can study the strong interaction in an experiment.

1.3 The strong interaction and the electroweak epoch

However, under this thesis work I focus on studying the possible consequences which arise in the Electroweak epoch ($\sim 10^{-36}s$ – $\sim 10^{-12}s$). The electroweak epoch follows the Grand unification epoch and at the transition ($\sim 10^{28}K$), the strong interaction separates from electromagnetic and the weak (electroweak) interactions. The corresponding symmetry breaking process is known as the chiral symmetry breaking which gives mass to quark flavors. It is also very important to understand that **cosmic inflation** (cosmic inflationary epoch:$10^{-36}s$ – $10^{-32}s$) occurred at a similar time period. Some theories even describe that electroweak epoch started $\sim 10^{-32}s$, after the cosmic inflation. It is during this time period the universe expanded exponentially and strong interaction started separating from electroweak interaction. Theory

incorporates a scalar field known as inflation field (having properties similar to Higgs field) in explaining this rapid expansion of the early universe. At the end of the inflationary epoch, the enormous potential energy of the inflation field was released filling the entire universe with a dense and hot quark gluon plasma. The high energetic collisions during this epoch were able to produce the $W^{\pm}$, Z^0 and Higgs bosons. The successive expansion and cooling down of the universe ceased the creation of W and Z bosons. The remaining ones decayed before going in to the Quark epoch ($10^{-12}s$ – $10^{-6}s$) where all four fundamental interactions have taken their present form. The end of the inflationary epoch (see Fig 1.2) is a significantly important time period for present day Big Bang studies. Scientist have experimentally verified the existence of W and Z gauge bosons describing the electroweak interaction that exists after the inflationary epoch.

1.3.1 Probing strong interaction at Relativistic Heavy Ion Collider (RHIC)

As the universe transits into the quark epoch (10^3 – 10^7 GeV), even though the fundamental interactions were in their present day form, the temperature of the universe was still too high for quarks to be bound into hadrons (protons and neutrons). As a result, the quark epoch universe was filled with high density and energetic quarks, gluons and leptons. This energy regime is what scientist hope to probe at RHIC. The epochs followed this era can also be studied in this facility at **B**rookhaven **N**ational **L**ab **BNL** (Hadron epoch: 0.1 – 10^3 GeV, Lepton epoch: 1 – 10^2 MeV [10]).

1.3.2 Properties of SU(3) gauge group and QGP

The fundamental representation 3 of gauge group SU(3) represents quarks via the use of Dirac fields. Quarks are spin 1/2 fermions that carry color charge which is responsible for the strong interaction as described in QCD. On the other hand, adjoint representation 8 of SU(3) represents gluons which are spin 1 bosons also carrying color charge. Therefore QCD describes the interaction between quarks and gluons, known as the study of SU(3) Yang mills theory of fermions which carry color (quarks). QCD carries two very important and interesting properties related to the interaction between quarks and gluons. Namely those of **confinement** and **asymptotic freedom**. The confinement feature is responsible for not observing free quarks in nature.

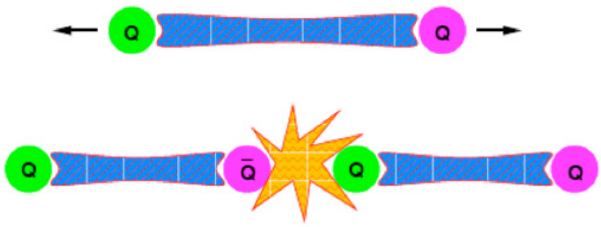

Figure 1.4: Quark confinement.

As seen in Fig 1.4 (top diagram) if two quarks are pulled apart, the QCD potential, that describes the force between them, increases linearly. However if one keeps pushing them apart, the chromoelectric field energy between quarks is released by producing a quark anti-quark pair as shown in the bottom diagram of Fig 1.4. The key observation here is that the newly produced quark anti-quark pair is now confined in bound states with the original quarks. This property of QCD is responsible

for generating color neutral hadrons (baryons and mesons) as below in Fig 1.5.

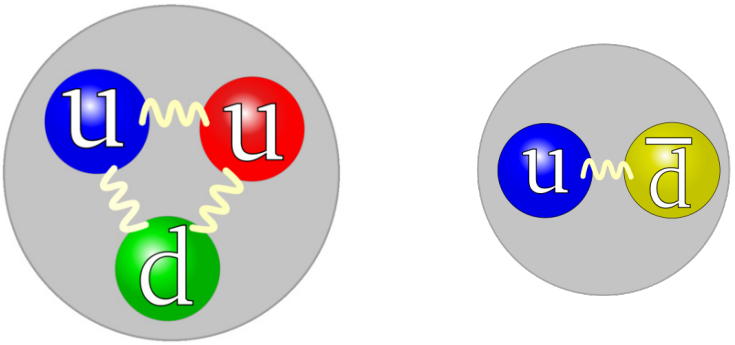

(a) Baryon (b) Meson

Figure 1.5: Quarks confined as a color neutral proton (a) and a color neutral π^+ meson (b).

Besides, the coupling strength between quarks becomes very small when they are brought closer together. This feature of QCD potential is known as asymptotic freedom. The theory of asymptotic freedom was a Nobel prize-winning discovery and it led scientists to attempt in the creation of a QGP, the pre-historic nuclear matter phase that consists of colored quarks and gluons which existed $\sim 10^{-32}s$ after the Big Bang. The first attempts at the AGS at BNL and the SPS accelerator at CERN suffered from low collision energies and thus the results were largely inconclusive. Only at the RHIC facility at BNL did we achieve the necessary conditions.

1.4 QGP signatures at RHIC

As described above, the creation of a QGP in the laboratory uses the property of asymptotic freedom in the QCD potential. To bring the quarks as close as possible,

scientists at RHIC attempt to generate the highest possible energy density. These early attempts were guided by Lattice QCD predictions [164].

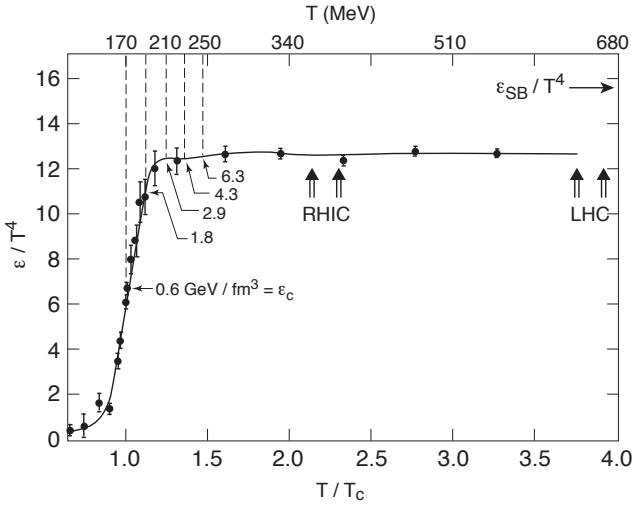

Figure 1.6: Lattice predictions for energy density as a function of temperature.

Figure 1.6 above shows the energy density in a nuclear system as a function of temperature. The sharp rise in the plot signifies a possible phase transition behavior from cold nuclear matter to hot dense QGP. In order to create these conditions, scientists at RHIC collide Au heavy ions at $\sqrt{S_{NN}} = 200$ GeV by accelerating them up to 0.99995c. Experimental details will be discussed in second chapter. The remainder of chapter one will discuss the time evolution of a heavy ion collision, and important QGP signatures scientists observed at RHIC. The chapter will close with the dissertation outline.

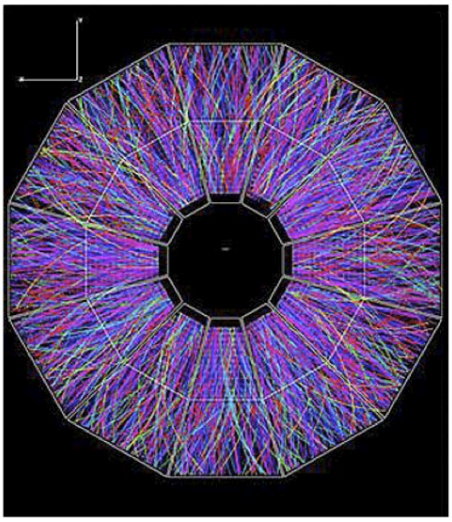

Figure 1.7: The charged particle tracks in an Au + Au collision at RHIC as seen in the STAR detector Time Projection Chamber (TPC).

1.4.1 The time evolution of a heavy ion collision

Figure 1.7 shows all final state charged hadrons as detected in the Time Projection Chamber (TPC) at STAR. Different colors of tracks correspond to different momenta. The series of cartoons in figure 1.8 shows the time evolution of a heavy ion collision which leads to these final state hadrons.

In figure 1.8(a), a schematic of colliding nuclei is shown. In their rest frame, they are spherical. In the CM frame the nuclei look like pancakes due to the Lorentz contraction in the beam direction. The initial collisions between nuclei occur as high-energy inelastic collisions of individual nucleons. Many partons are liberated in these collisions and the high density environment allows them to re-scatter several times. Thus the initial momentum distribution that was highly correlated along the beam axis is redistributed and leaves a substantial amount of kinetic energy in

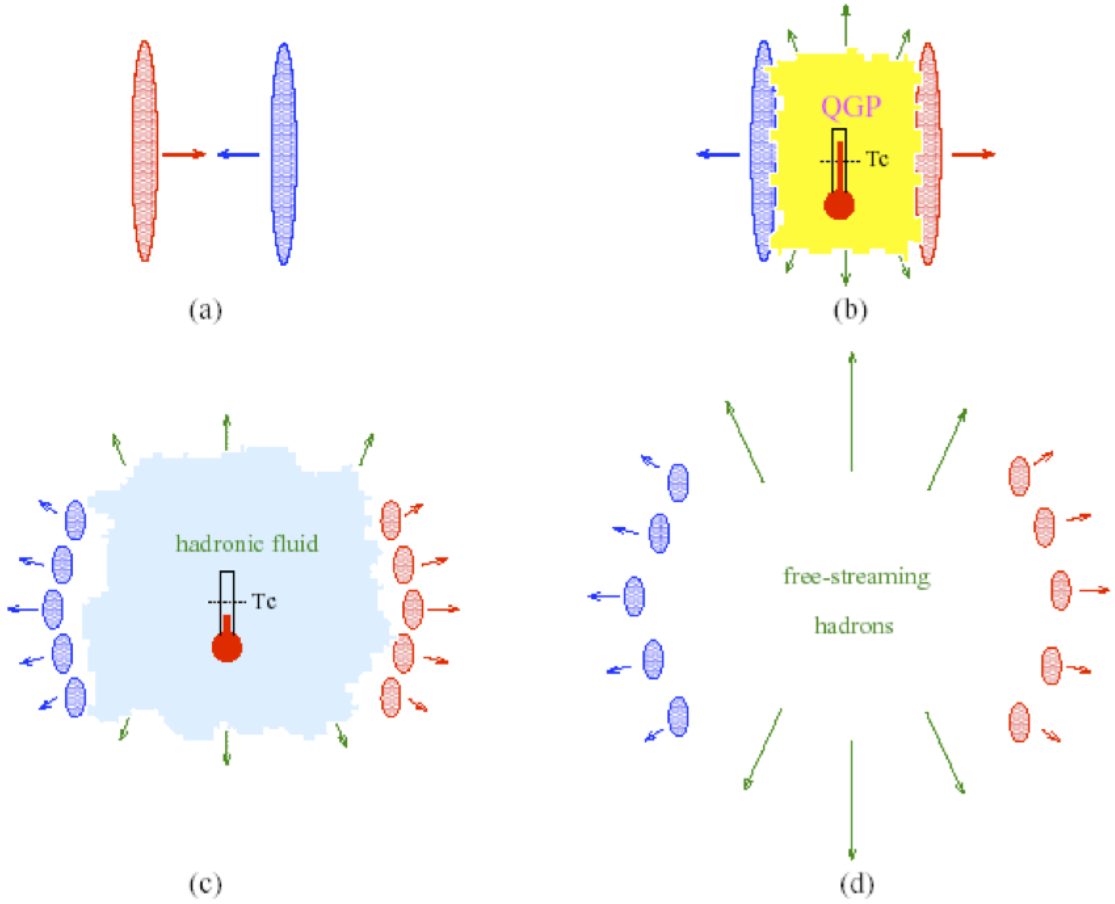

Figure 1.8: Schematic view of the various stages of a heavy ion collision. The thermometers indicate when thermal equilibrium might be attained.

the CM frame in order to produce a fireball in the mid rapidity region (the region perpendicular to the beam axis). This energy is converted to hadrons via quark, anti-quark pair production, thus leaving the net baryon density to be zero. In directions along the beam axis, even for lower energy heavy ion collision experiments, the baryon density is rich corresponding to the initial baryon concentration of the nuclei. Hence the nuclei have effectively passed through each other (i.e. the collision is transparent at RHIC energy). The rapidity y for a particle with 4-momentum vector is defined,

$$y = \frac{1}{2} ln \left(\frac{E + p_z}{E - p_z} \right) \tag{1.1}$$

where E is the total energy and p_z is the momentum along beam direction (z-direction) in CM. At relativistic speeds, the rapidity can be approximated by pseudo-rapidity η, which is the variable used commonly in all two-dimensional di-hadron correlation analysis.

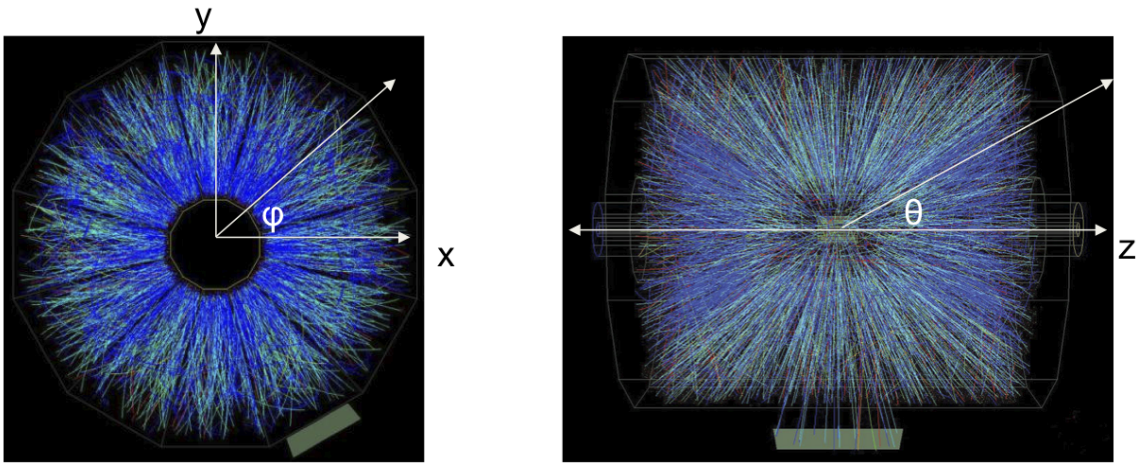

Figure 1.9: Left panel: Shows the azimuth angle as defined in the STAR detector. Right panel: Shows the angle θ with respect to the beam direction which is used to define the pseudo-rapidity η = -ln(tan(θ/2)).

The study by Bjorken gives the energy density in the central region, at the proper time τ for a collision that happens at the origin (t, z) = (0, 0) as [23],

$$\varepsilon(\tau) = \frac{1}{\tau A} \frac{dE_\perp}{dy} \mid_{y=0} \tag{1.2}$$

assuming thermalization of the system. In the above equation, **A** gives the area perpendicular to the beam direction (Z direction) or transverse area of the incident nuclei. The derivative term gives the transverse energy per unit of rapidity. For central collisions at the Super Proton Synchrotron (SPS) at CERN, by assuming the thermalization occurs at τ = 1fm/c, the above equation approximates the energy density to be $3GeV/fm^3$. Using the plot in figure 1.6 it is noticeable that this corresponds to a temperature of the order of 200 MeV. This temperature is sufficient to create a QGP.

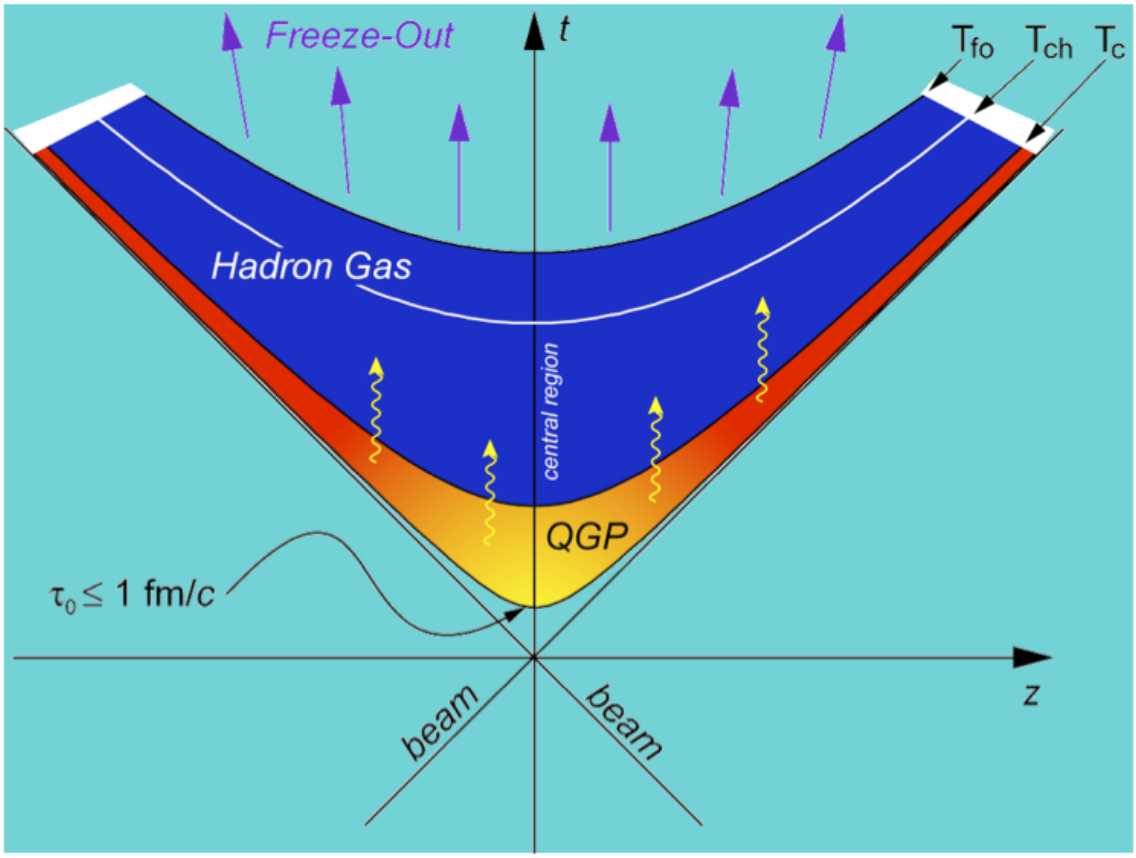

Figure 1.10: Time evolution of the collision system. T_c, T_{ch} and T_{fo} denote the critical temperature, the chemical temperature and the freeze out temperature respectively.

The system should expand and de-excite to its hadronic ground state, i.e. the vacuum state, due to the fact that the initial system possesses an excess pressure with respect to the surrounding vacuum. Around 4fm/c, when the system temperature reaches T_c, the system will start forming hadrons (hadronization) via certain proposed particle production mechanisms. Understanding these mechanisms is one of the highlighted areas of my research. The majority of these hadrons are pions. These hadrons will further collide inelastically to the point where the chemical freeze out occurs (T_{ch}). The system then experiences elastic collisions until the thermal freeze out occurs (T_{fo}). At this point the hadrons will free stream towards the detectors as shown in figure (1.8(d) and 1.10). The detected hadrons should reveal the conditions inside the fireball, i.e. detected hadrons might carry the information of whether QGP is formed in the initial system. The distribution of transverse mass is studied to see whether the initial system reached thermalization. Studies have shown that the thermal freeze-out occurs at a temperature of $T_{fo} \leq 100$ MeV. At this point the scattering surface has an approximated radius of 7fm and an expansion velocity of 0.6c [24].

1.4.2 The energy lost in the medium

The medium can be studied via the partonic energy losses in the system. Bjorken proposed that the collisional energy loss dE/dx of the hard scattered partons in nuclear collisions could provide a sensitive probe of the surrounding medium [11]. Further studies [12], [13], [14] showed that the energy loss from scattering is negligible but there is a considerable energy loss due to radiation of the partons in the

dense medium, meaning the energy loss is directly sensitive to the gluon density of the medium, if we have achieved the deconfinement of quarks and gluons. The substantially larger energy loss in the measured matter than that in cold nuclear matter [15] is incompatible with the presence of a hadronic medium.The large energy loss measurement therefore serves as an indirect signature of deconfinement.

1.4.3 Suppression of inclusive hadron spectra

A comparison between the particle spectra of the systems where we expect and not expect the formation of a high density medium is one of the initial approaches scientists have taken to study the partonic energy loss of the medium we create at RHIC. The relevant quantity is called the nuclear modification factor. Here we compare the momentum spectra of produced charged particles in Au + Au collisions with p + p and d + Au collisions. In p + p and d + Au systems we do not expect the formation of a high density medium. The definition of nuclear modification factor is therefore as follows.

$$R_{AB}(p_T) = \frac{\sigma_{pp}.d^2\sigma^{AB}/dp_T d\eta}{< N_{bin} > .d^2\sigma^{pp}/dp_T d\eta} \tag{1.3}$$

The numerator $d^2\sigma^{AB}/dp_T d\eta$ stands for the integral yield in the A + B collision in a given p_T bin, and the denominator $d^2\sigma^{pp}/dp_T d\eta$ gives the corresponding p + p yield. The coefficient $< N_{bin} >/\sigma_{pp}$ scales the p + p yield by the number of binary collisions in the Au + Au collisions at a given centrality. In addition to partonic energy loss, the above quantity may be altered by nuclear effects such as gluon

shadowing and soft partonic multiple scattering in the initial state (Cronin effect). The former will reduce R_{AB} measurement where as latter would increase it.

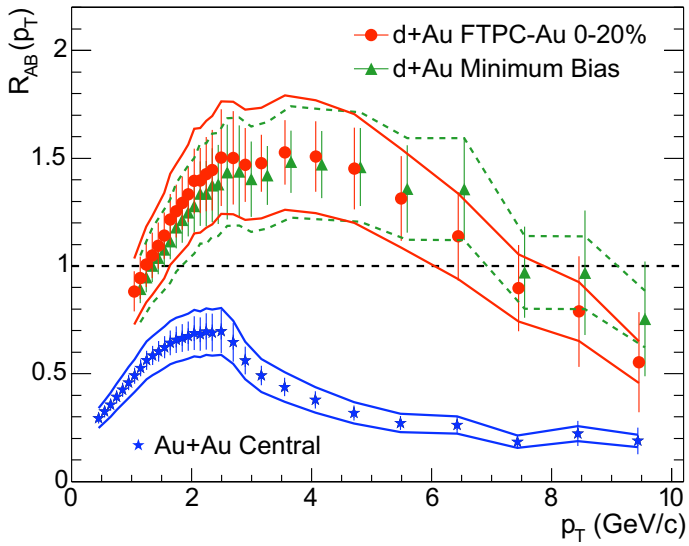

Figure 1.11: Measurement of energy loss due to the dense medium in central Au + Au collisions.

Figure 1.11 shows the R_{AB} measurement for the most central (refer to section 3.3.2) Au + Au collisions (star symbol) and two separate R_{AB} measurements for d + Au data. The circles represent the data taken in the top 20% of head on d + Au collisions and the triangles show the R_{AB} from the minimum bias d + Au collision data. The uncertainties due to normalization are shown by the solid lines. The dashed line at $R_{AB} = 1$ signifies the expected ratio if d + Au or Au + Au collisions were only a superposition of the appropriate number of p + p collisions. With respect to energy loss of a traversing parton, only the p_T range where parton fragmentation according to QCD is applicable and should be taken into account. Generally this threshold is set to $p_T > 2GeV/c$. First important implication of fig 1.11 is that the Au + Au charged particle spectrum is significantly suppressed

beyond 2.5 GeV/c. The theoretical studies done [16, 17] show that the observed suppression cannot be explained via hadronic interactions only, but requires energy loss via partonic interactions. The second important implication is that the R_{AB} for d + Au data is not suppressed and the behavior can be explained by introducing hadronic energy loss only [16, 17]. The initial enhancement we see of the charged particle spectra in the p_T region between 1.5 and 3 GeV/c is explained as Cronin effect [18]. In the d + Au system the Cronin effect alone is observed whereas in Au + Au the Cronin effect and energy loss will occur. Thus the observed suppression in Au + Au has to overcome the positive Cronin effect contribution. In order to determine the suppression factor alone, one therefore needs to compare the d + Au and Au + Au spectra in a p_T range where the Cronin effect is negligible (i.e $p_T > 7GeV/c$). A comparison between the suppressions of Au + Au system and d + Au system at $p_T \approx 8GeV/c$ (i.e. analog to comparing with p + p) reveals a suppression of a factor of 5 between the two systems.

Figure 1.12 represents R_{AA} for various Au + Au centrality bins relative to the p + p reference spectrum. It is observed that R_{AA} increases monotonically for $p_T < 2GeV/c$ at all centralities and saturates near unity for $p_T > 2GeV/c$ in the most peripheral bins. This is in contrast to central bins where R_{AA} reaches a maximum and decreases rapidly above $p_T = 2GeV/c$, thus showing suppression of the charged hadron yield relative to the p + p reference spectrum. We conclude that the denser the partonic medium the larger the high p_T suppression.

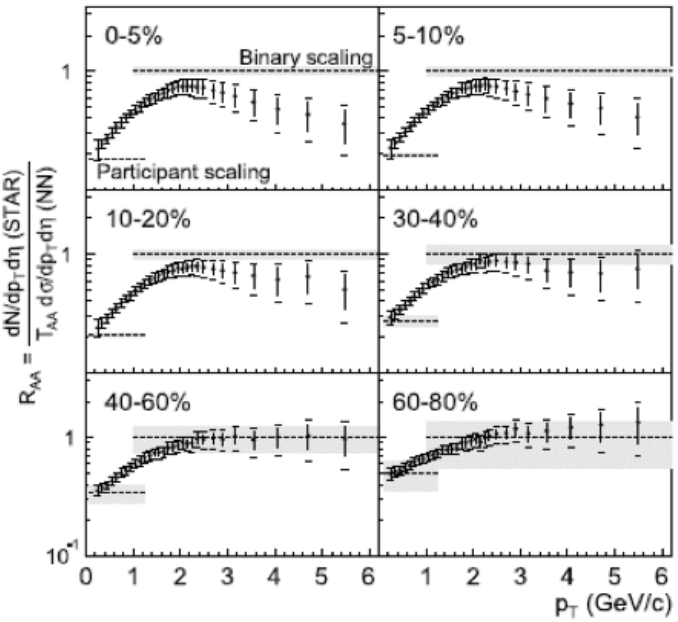

Figure 1.12: $R_{AA}(p_T)$ for various centrality bins for Au + Au relative to p + p (NN) reference spectrum.

1.4.4 Jet-like correlations via high p_T dihadron azimuthal correlations

One known particle production mechanism in elementary collisions is partonic hard scattering (high p_T), with subsequent parton fragmentation into hadrons. This process will form collimated groups of energetic hadrons or so called jets.

The leading partons in the jet are back to back in azimuthal angle ϕ (see Fig 1.13 and 1.9). At RHIC energies, jets are produced in sufficient numbers to probe the medium [25]. While full jet reconstruction is challenging (due to large combinatorial background) in high energy nuclear collisions, additional insight into partonic energy loss can be gained by studying jet-like correlations of high p_T dihadrons. In p + p

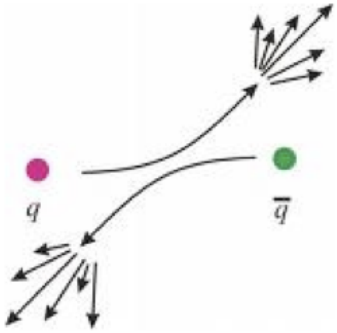

Figure 1.13: Fragmentation of a quark anti-quark pair, producing back to back jets.

collisions at RHIC energies, hadrons with $p_T \approx 4GeV/c$ carry 75% of the energy of their parent jet [25].

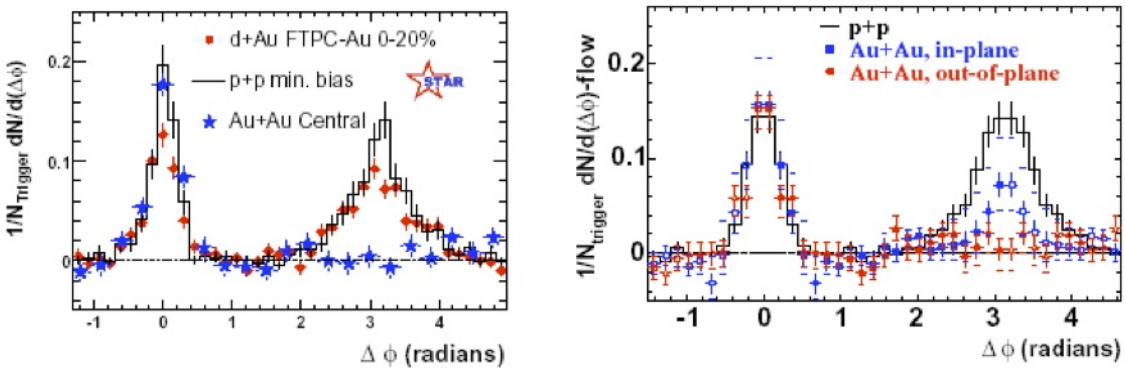

Figure 1.14: Relative angle distribution for high p_T dihadrons at $\sqrt{S_{NN}} = 200$ GeV. Left: p + p, d + Au and central Au + Au collisions. Right: trigger particle in or out of reaction plane in non-central Au + Au collisions [19].

Fig 1.14 represents the relative azimuthal angle distribution of associated hadrons defined as,

$$\frac{1}{N_{trigger}}\frac{dN}{d(\Delta\phi)} = \frac{1}{N_{trigger}}\frac{1}{\varepsilon}\int d(\Delta\eta)N(\Delta\eta,\Delta\phi) \tag{1.4}$$

where ε is the track efficiency and $N_{trigger}$ is the number of charged hadron tracks satisfying the trigger requirement (criteria for been selected as a reference particle), and N$(\Delta\eta, \Delta\phi)$ is the number of hadron pairs with relative azimuth $\Delta\phi$ (azimuthal angle difference between the two particles) and relative pseudo rapidity (measurement of an angle relative to the beam direction) $\Delta\eta$ (see figure 1.9). The trigger particle is selected to be in the momentum range $p_T^{trig} > 4GeV/c$ (trigger requirement). We associate particles in the momentum range $2 < p_T < p_T^{trig}$ to the trigger particle in azimuthal angle. The resulting correlation structure is shown in fig 1.14. The correlation study described by the above equation is known as a triggered correlation analysis. Many forms of triggered correlation studies are done in STAR. In fig 1.14 left hand side, the approximate similarity we observe on the near side ($\Delta\phi \approx 0$) for the systems p + p, d + Au and Au + Au is consistent with negligible partonic energy loss and fragmentation of the leading parton in the Au + Au system. The absence of the away side correlation in Au + Au compared to the other two systems thus suggests strong suppression of the collimated hadrons on the away side. This observation is consistent with significant medium-induced partonic energy loss. The selection of the leading particle (trigger) is such that it traverses less distance in the medium. In other words, it escapes much closer to the surface of the fireball. On the other hand, the recoiling jet parton has to go through the bulk medium of the fireball. This geometrical bias plays an important role in high p_T di-hadron azimuthal correlations. A similar di-hadron analysis can be performed in non central Au + Au collisions. The result is shown on the right hand side of fig 1.14. The reaction plane (fig 1.15) of the nuclear collision has been used to evaluate

the in plane and out of plane yields. The away side yields in plane and out of plane strengthen the conclusions that the energy loss is path dependent. As can be seen in fig 1.15, the in plane medium length is smaller than the out of plane length. Fig 1.13 right hand side shows that the energy loss in plane is smaller than out of plane. Thus we can conclude that, the energy loss depends on path length.

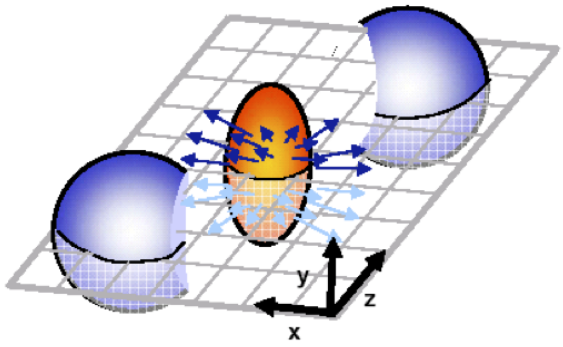

Figure 1.15: A typical non central collision of two heavy nuclei. Along the Z axis is the beam direction and X-Z is the reaction plane.

It is vital to raise the question, what happens to the hadrons in the recoiling jet? Even though we call it a suppression, it is likely that the particles produced via fragmentation have lost energy, but can be recovered at lower momentum plus new lower momentum particles are formed because the momentum in the event needs to be conserved. A study has been carried out in [20], where it has been demonstrated qualitatively that the soft recoiling hadrons in central Au + Au collisions are seen to be distributed broadly in azimuth and soften in p_T compared to similar distributions in p + p. The azimuthal distribution consistent with no dynamical correlations beyond simple momentum conservation is described in [19].

The dependence of the soft and hard associated hadrons per trigger particle can

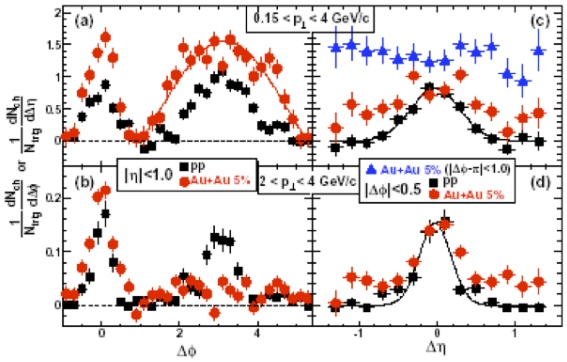

Figure 1.16: Background subtracted $\Delta\phi$ and $\Delta\eta$ distributions for p + p and most central Au + Au for $4 < p_T^{trigger} < 6GeV/c$ and two associated p_T ranges.

be realized by comparing fig 2.16 (a) and fig 1.16 (b). More soft associated hadrons are found in central Au + Au than in p + p, on both near and away sides. Taken alone, fig 1.16 (b) supports the conclusions we made previously. It is important to note that in fig 1.16 (a), inclusion of soft particles broadens the $\Delta\phi$ peak especially on the away side. This shape on the away side was expected for purely statistical momentum balance of the near side jet [21]. A similar correlation approach was recently extended into a two-dimensional ($\Delta\eta$, $\Delta\phi$) correlation analysis. Fig 1.17 presents the result obtained for two-dimensional correlation functions for high p_T charged hadrons from p + p (top) and central Au + Au (bottom) collisions. A jet-like correlation is observed at small angular separation in η and ϕ for both cases. Correlations in the away side are also apparent for both cases with a broadening along $\Delta\eta$. An additional correlation strength in central Au + Au but not in p + p is seen for small relative azimuthal angle ($\Delta\phi \approx 0$) and long range in pseudo-rapidity (large $\Delta\eta$).

A preliminary analysis suggests that this long range $\Delta\eta$ component is effectively

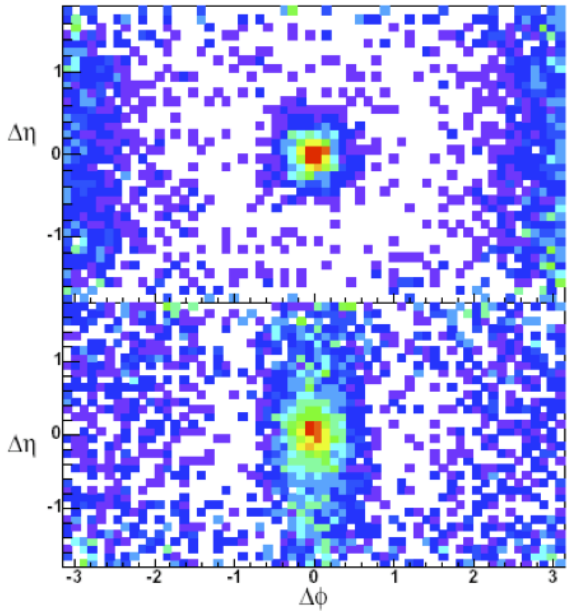

Figure 1.17: Two-dimensional ($\Delta\eta$, $\Delta\phi$) charged dihadron correlation functions from minimum bias p + p (top) and central Au + Au (bottom) collisions at $\sqrt{S_{NN}} = 200$ GeV with $3 < p_T^{trig} < 6 GeV/c$ and $2 < p_T^{assoc} < p_T^{trig}$.

uniform within the STAR acceptance $|\eta| < 1$ and it is distinct from the jet-like peak, perhaps indicating an independent underlying mechanism. The width of the short range jet-like correlation is similar in central Au + Au and p + p collisions for $p_T^{trig} > 6$ GeV/c but exhibits medium induced broadening at lower p_T^{trig} , while the jet-like correlation yield is independent of centrality [25]. The same side long range correlations for soft hadrons ($p_T < 2GeV/c$) were also studied [22]. In addition a new analysis extends the observations to the region where parton fragmentation might become significant [19]. I would like to conclude the first chapter by bringing up the importance of the same side long range correlation structure we observe in two-dimensional correlations, as discussed in section 1.4.4 The physics behind this structure is not well understood as yet. The focus of my dissertaion is an attempt

to address this question.

1.4.5 Dissertation outline

In chapter two we discuss in detail about the experimental facility, the Relativistic Heavy Ion Collider (RHIC) and the STAR detector. The ion acceleration stages will be discussed followed by the other main experimental facilities connected to the RHIC. Then we discuss about the STAR detector and its sub detector components. In chapter three we focus on the di-hadron correlation formalism. We discuss in detail the relation between fluctuations and correlations and derive the correlation measurement we construct. Latter part of chapter three will focus on specific analysis detail when experimentally constructing the correlation measurement. Chapter four introduced the components in our empirical model. The mathematical form of all model components, in relation to their corresponding physical process is explained. The composite model functional form and fit procedure is also discussed towards the end of this chapter. Chapter five reports the results from our model studies and comparisons to predictions. Finally, in chapter six, we discuss the implications from our experimental findings towards understanding the QGP formation and relevant medium properties.

Chapter 2

The STAR experiment at RHIC

Particle accelerator technology is truly one of the remarkable achievements in science. The history of accelerated beams of particles goes all the way back to Crooks cathode ray tube experiment studies in 1870. Initially these cathode rays produced beams of electrons that were accelerated via a DC voltage. Rutherford's scattering experiment in 1909 first utilized accelerated beams of α particles in order to investigate the atomic structure. During the same period in time (1923), de Broglie postulated higher resolution into the matter structure can be obtained by shooting high energetic particles into target material. The relation $\lambda = \mathrm{h/p}$ formulates Louise de Broglie's postulate and it tells us that high energetic particles (large p) give finer resolution (small λ) in probing a target. Here h is the plank constant ($6.626068 \times 10^{-34} J.s$). Thus acceleration of particles to higher energy became an important and nobel price winning task. The Cockroft-Walton generator (Nobel prize in 1951), the Van de Graaff generator and the tandem generators were among the first DC accelerators. As

further acceleration through application of DC became a difficult task, the cyclotron was introduced by Leo Szilard and initially manufactured by Ernest Lawrence in 1932. The cyclotron uses an electric field generated by an AC current to produce high energy particle beams. Lawrence received the Nobel prize in 1939 for his work. In order to overcome the limitations of cyclotron operation at relativistic speeds, AC current was later on replaced by Radio Frequency (RF). The early RF accelerators were linear accelerators, replaced by cyclotrons and synchrotrons in recent years. In modern days study higher CM energies are obtained with collider experiments rather than fixed target experiments. The first collider built was ADA (Anello di Accumulazione) in 1961. And as of today, the two of the most powerful colliders in the world are the Relativistic Heavy Ion Collider (RHIC) at BNL, Upton, New York and the Large Hadron Collider (LHC) at CERN, Geneva, Switzerland.

2.1 The Relativistic Heavy Ion Collider - RHIC

The RHIC is the newest addition to the existing Alternating Gradient Synchrotron (AGS) at BNL. Fig. 2.1 shows an arial view of the RHIC accelerator complex. To reach energies much higher than those achieved in previous heavy ion programs at the AGS, the new machine had to be built as a collider. Also in the recent past the Super Proton Synchrotron (SPS) at CERN accelerated particles up to the size of the Pb. Various fixed target experiments at AGS and SPS opened a new era in the search of the Quark-Gluon Plasma. In 2000 the Relativistic Heavy Ion Collider (RHIC) at

Brookhaven National Laboratory was completed in order to investigate the properties of nuclear matter at ultra-high energy densities. In 2007 the Large Hadronic Collider(LHC) at CERN was commissioned, reaching even higher CM energies.

Figure 2.1: The RHIC Accelerator Complex [168]

The Table (2.1) presents an overview of ultra-relativistic heavy ion accelerators which summarizes the last 30 years of heavy ion collision experiments from 2 GeV (1975) to 5500 GeV(2007). It shows the maximum energy-per-nucleon in the centre-of-mass frame and whether the set-up yields fixed target or collider mode.

Table 2.1: Experimental facilities for heavy ion collisions.

Experimental Facility (time period)	Laboratory	$\sqrt{S_{NN}^{max}}$	Type
BEVLAC(1975 - 1986)	LBNL	2.0 GeV	Fixed target
SIS(1989 -)	GSI	2.4 GeV	Fixed target
AGS(1986 - 1998)	BNL	4.8 GeV	Fixed target
SPS(1986 - 2003)	CERN	17.3 GeV	Fixed target
RHIC(2000 -)	BNL	200 GeV	collider
LHC(2007 -)	CERN	5500 GeV	collider
FAIR(2014 -)	GSI	8 GeV	Fixed target

Other than being the second highest CM energy carrying collider, RHIC is very versatile in many aspects. RHIC is the only collider in the world capable of colliding both longitudinally and transversely polarized protons. Polarized proton collisions are used to study the origin of the spin of the proton. RHIC has now collided polarized protons up to $\sqrt{S_{NN}} = 500$ GeV. RHIC is also designed to collide nuclei with an atomic mass, A, ranging from A = 1 to A $\approx$ 200. In addition it is capable of producing asymmetric collisions, those between ions with different masses, such as d + Au. Asymmetric collisions are useful for distinguishing the effects of cold nuclear matter (modification of the initial state in a nucleus) versus hot nuclear matter (such as a QGP). Also the span of CM energies that RHIC can provide is remarkable and unique as demonstrated during 2010/11 RHIC operations in order to scan the QCD phase diagram near the proposed critical point. The machine throughout the years produced a wealth of data and continues to do so. The future upgrades planned for RHIC as well as the associated experiments that should provide data for further ground breaking discoveries. The following paragraphs discuss in detail the individual components of the RHIC complex.

2.2 RHIC complex

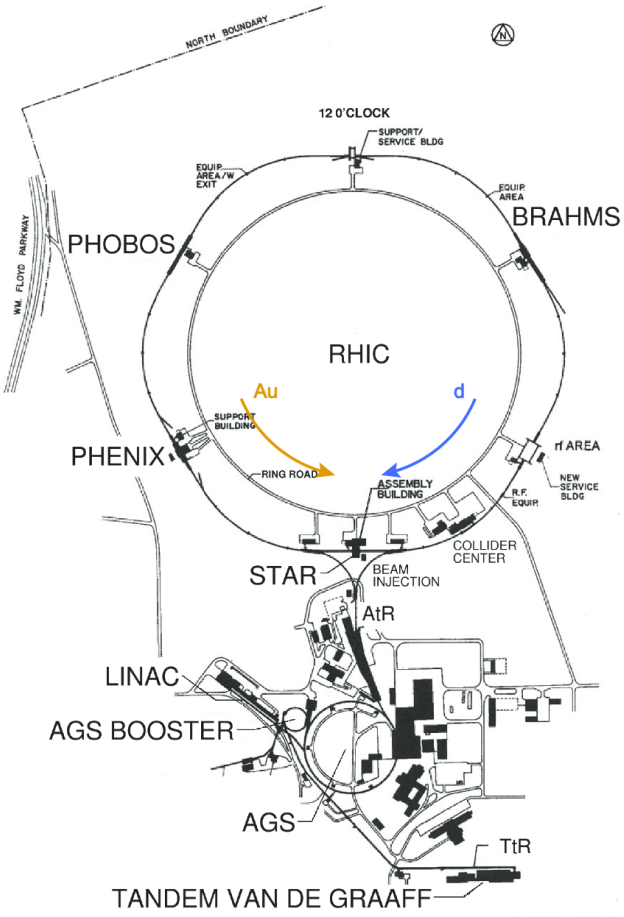

Figure 2.2: Perspective view of the RHIC complex in BNL. The four experiments are also indicated at the interaction points [169].

Fig. 2.2 shows general details of the RHIC complex. Fig. 2.3 [26] shows a schematic with details of the Au+Au acceleration procedure. In the following subsections, we will discuss the main acceleration subcomponents at the RHIC complex. Those are: pulsed sputter ion source, Tandem Van de Graaff generator, Booster, AGS, and finally the RHIC.

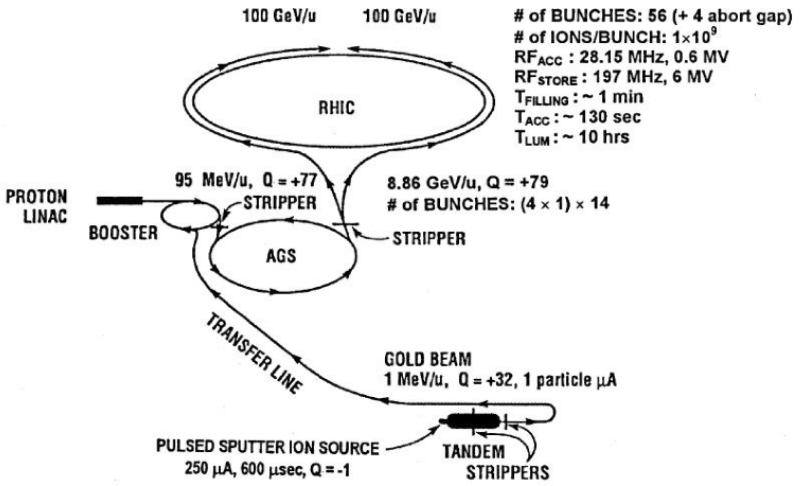

Figure 2.3: Acceleration scenario for AU ions

2.2.1 Pulsed sputter ion source

Fig. 2.4(a) shows a schematic of the ion source is used at RHIC. The cesium sputter source was designed and developed primarily by R. Middleton around 1974 [27]. It generates ions by bombarding (sputtering) cesium ions on a target material. After sputtering of cesium ions, the target liberates negative ions. An electrostatic field then guides the liberated target ions out of the chamber. The cesium vapor is ionized to a positive state with the use of a cylindrical ionizer prior to sputtering the target material. There is an electric field pointing toward the sputter target which will kick the released negative target ions out of the source to the left since the sputter target is held at a negative voltage while the outer shell is held at ground potential. Fig. 2.4(b) shows an actual target holder compared to the size of a penny.

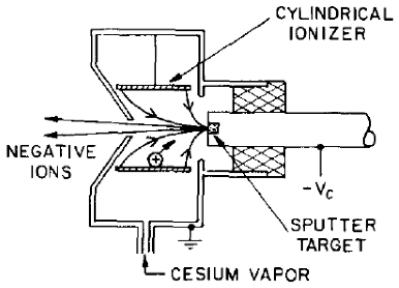

(a) The Cesium sputter source

(b) An empty target holder compared to the size of a penny

Figure 2.4: Pulsed sputter ion source

2.2.2 Tandem Van de Graaff accelerator

The tandem is a linear electro static accelerator. A dual-stage or tandem Van de Graaff is shown in fig. 2.5. A dual-stage Van de Graaff is designed by connecting two single stage Van de Graaff generators. The joining region is set at the same potential. At the RHIC facility, both ends are kept at ground potential and the joining region is kept at +14MV. The negative Au^{1-} which is created at the source is been accelerated by the electric field resulting from the high voltage, and subsequently guided into a gold stripper foil. The stripper foil is simply a very thin sheet of gold used as a target. The resulting collisions can produce a wide range of possible charge states. After the collisions, a magnetic field is used to extract only those ions with the desired charge. A series of acceleration, strip and extract is used in additional stages to reach the final desired charge and energy needed in a RHIC collision. The beam leaving the

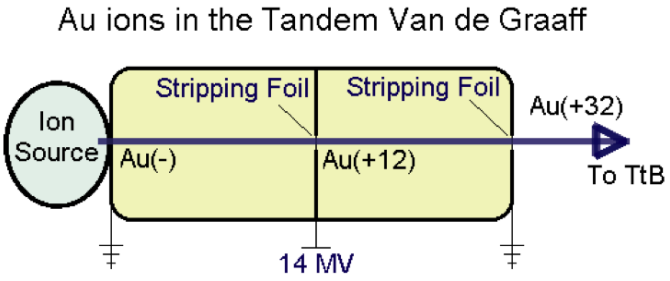

Figure 2.5: The tandem Van de Graff accelerator

Tandem is composed of Au^{12+} ions with an energy of about 1 MeV per nucleon. The beam strikes another stripper foil in the Tandem to Booster (TtB) transfer line(850 m long), on the way to the Booster. The beam injected into the Booster has a charge state of 32^{+}.

2.2.3 The Booster

The Booster is a synchrotron accelerator with a circumference of 202 meters. The design of a synchrotron allows charged particles to be accelerated at a fixed radius via the application of a spatially uniform magnetic field causing the particles to move in a circular orbit. An oscillating electric field is applied at one point during the orbit and this electric field accelerates the particles by a small amount during each successful revolution. The magnetic field is adjusted accordingly as the particles energy(speed) increases. The result is that particles in the Booster are accelerated over and over again up to a higher energy.

A very good vacuum is required to reach the desired energy in high intensity ion

beams. The gold ions can interact with residual gas in the vacuum of the Booster which can result in the capture or loss of electrons. Electron capture is a problem at low energies and electron stripping becomes more serious at higher energies [28]. Either case leads to lost particles. The Booster maintains an excellent vacuum, so there are fewer gas particles to interact with the ion beam. The electron stripping causes the number of ions to be halved from $\sim 4.3 \times 10^9$ (on leaving the Tandem) to $\sim 2 \times 10^9$ upon injection into the AGS [29]. At this charge and energy (100 MeV/nucleon), electron capture probability has come down to a level in which the AGS can continue beam acceleration with acceptable losses. Before entering the AGS, the beam crosses another stripper foil (see fig. 2.3), creating Au^{77+}.

2.2.4 The linear accelerator - LINAC

The Linear Accelerator (LINAC) at the RHIC complex is the starting point for protons and light ions. This accelerator can accelerate 35 mA beams of protons to energies up to 200 MeV [30]. To accomplish this, the LINAC uses nine radio-frequency cavities that span the 140 m tunnel. Radio waves oscillate in the cavities so protons and electrons, particles that interact with the electric field, are accelerated. The radio waves are timed to push protons or electrons in a way similar to that in which a wave pushes a surfer. By using different radio frequencies, these particles are accelerated in steps as they traverse the nine cavities. These particles are then transferred to the Booster Synchrotron.

2.2.5 The Alternating Gradient Synchrotron

The Alternating Gradient Synchrotron (AGS: 807m in circumference) is the second largest accelerator at Brookhaven National Lab. It accelerates gold ions up to 0.997 c. Therefore to accelerate ions, they are directed through a series of electromagnetic fields that alternate in field gradients. This process, referred to as alternating gradient focusing, simultaneously accelerates and bunches these heavy ions. This method of alternating electromagnetic field gradients was first developed at Brookhaven National Laboratory, and is currently used by almost every supercollider in the world [31]. By the end of this process, the AGS will have separated the beam into 57 distinct bunches. These bunches fill the RHIC rings one beam at a time via the AGS to RHIC, or ATR, line [32]. Gold ions leave the AGS with an energy of 9 GeV per nucleon before traversing the last stripper foil. This interaction strips the remaining electrons leaving bare nuclei of the species Au^{79+}.

2.2.6 The Relativistic Heavy Ion Collider

The RHIC consists of two independent rings (blue and yellow) of superconducting magnets. The rings are enclosed in a tunnel which lies $\sim$ 3.6 m underground. In the center of each ring is a beam pipe along which the ion beam travels. The ion beams travel in clockwise and counterclockwise directions in the blue and yellow rings, respectively. A vacuum of 10^{-11} bar is maintained in the beam pipes in order to avoid interaction between the gas molecules and relativistically moving ions. The collider consists of straight and curved sections alternatively. In the curved sections, dipole

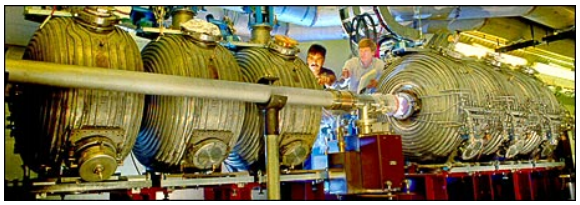

(a) A Radio Frequency(RF) cavity at RHIC

(b) The two RHIC rings underground

Figure 2.6: Particle acceleration at RHIC [170]

magnets steer the ion beam along the curvature of the pipes. In the straight sections, quadrupole magnets guide the beam along the beam axis. All RHIC magnets are superconductive magnets. They are cooled by supercritical helium to maintain an operational temperature of < 4.6 K. Radio cavities located in the straight sections of the rings generate a high frequency electromagnetic field which is used either to accelerate or to store the bunches of particles at each pass around the ring. In the middle of each straight section is an intersection region where the beam pipes cross, allowing the particle beams to collide. At the six intersection regions, is where the experimental areas are located, the trajectories of the incoming and outgoing beams merge. Dipole magnets are used to steer the beams so that they travel on the same trajectory for ~ 19 m. At the middle of this distance the bunches of nuclei collide, resulting in a diamond shape interaction zone of less then a meter. After

merging, another set of dipole magnets is used to separate the outgoing beams so that they return to their respective beam pipes. The ion bunches are filled to the RHIC rings as described above in (sec 2.2.5). In acceleration mode the bunches are captured by the two radio cavities (fig. 2.6(a)), which are operated at $\sim$ 28 MHz. This frequency corresponds to a harmonic number of 360 i.e. the circumference of the collider rings is subdivided into 360 individual buckets with a length of 10.5 m, where bunches of ions can be placed. For the first two years of RHIC operation, the collider was run mainly in a mode where every 6th bucket was filled. This lead to a total of 60 bunches in each ring. The 60 bunches are injected from the AGS into each collider ring in a bunch-to-bucket nature, where the AGS extraction system transfers one single bunch made up of four AGS bunches into one of the collider rings. This cycle is repeated 2×15 times in order to fill each collider ring with 60 bunches. Filling both rings takes $\sim$ 1 minute. After the bunches are injected into the rings, they are captured by the rising slope of the radio cavity electromagnetic field. Since the ions in the bunches are spread in velocity, the slow bunch-ions are accelerated by the rising slope of the radio frequency electromagnetic field while the faster bunch-ions are slowed down. The ions are accelerated to a speed that is close to the speed of light. After reaching that speed, only the energy of the ions is increased by the radio frequency electromagnetic field, so that ions with higher energy are less deflected by the dipole magnets. This makes them travel a longer path length, and introduces a delay relative to the ions with a lower energy. In this case an ion bucket must be on the falling slope of the radio frequency electromagnetic field, so that the more energetic (faster) ions are slowed down and the less energetic (slower) ions are

accelerated. The energy at which this takes place is called the transition energy. At the transition energy, interaction between bunch ions can cause beam instabilities. Pulsed quadrupole magnets fed by fast power supplies are used to quickly increase the energy of the beam ions to a value above the transition energy. For gold ions the transition energy is 22.9 GeV/nucleon. All ions, except protons, are injected below the transition energy and have to be accelerated through the transition to reach the maximum energy. When the bunches are accelerated to maximum energy - a process which takes about another minute - the collider switches from the 28 MHz acceleration mode to the 200 MHz storage mode. The harmonic number of the storage mode is h = 360×7 = 2520 resulting in a bucket length of 1.52 m. This high frequency enables the beam to be stored in short bunches having a length of $\sim$ 25 cm [33]. Such a short bunch length results in a r.m.s longitudinal collision vertex distribution of sin 18 cm at the six intersection regions where the counter-rotating beams collide. At each experiment, two zero-degree calorimeters (ZDC) are installed (18m away from the center of the STAR detector). The ZDCs detect spectator neutrons emitted, within a cone along both beam directions, from the collision vertex. The coincidence signal of both ZDCs is used as a common trigger by the experiments. Table 2.2 lists important parameters for RHIC.

2.2.7 Experiments at RHIC

The Broad RAnge Hadronic Magnetic Spectrometer (BRAHMS) is located in the 2 o$'$clock position on the RHIC ring. As one of the two smaller detectors, its acceptance is limited to particles coming from very specific angles. Using its spectrometers,

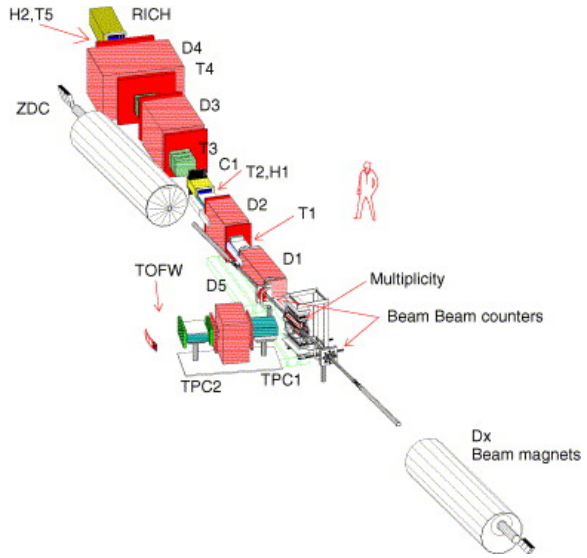

Figure 2.7: A schematic diagram of the BRAHMS detector

BRAHMS measures the momentum distribution of the detected particles. BRAHMS consists of two branches of detectors, the forward spectrometer and the mid-rapidity spectrometer (see fig. 2.7). Rapidity is a dimensionless measurement of a particles forward momentum along the beam line. By measuring θ from the beam line, the forward spectrometer covers $2.3° < \theta < 30°$ [34], and is composed of a long array of calorimeters and tracking detectors. The mid rapidity spectrometer covers $30° < \theta < 90°$ [34]. It is composed of two Time Projection Chambers (TPCs), which allow the identification of charged hadrons. The primary goal of BRAHMS is to study charged hadrons emitted from the RHIC collisions, and correlate transverse momentum (the momentum component perpendicular to the beam line) with centrality (the degree of overlap between colliding particles).

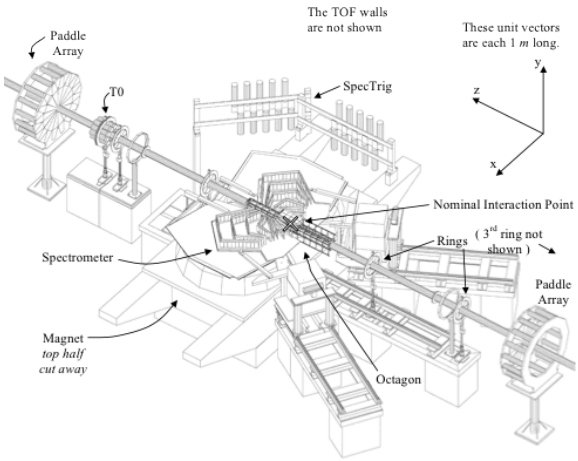

Figure 2.8: A schematic diagram of the PHOBOS detector [35]

PHOBOS [35], as seen in fig. 2.8, is designed to perform studies of global parameters with complete solid angle coverage. Charged particles can be detected over the pseudo rapidity interval $|\eta| < 5.4$ using an Octagon Multiplicity detector and six Ring Multiplicity detectors. Two small acceptance spectrometer at mid-rapidity as well as a time-of-flight wall allow for particle identification. Additional detectors include a Vertex detector, sets of scintillator paddles and a Cherenkov detector arrays for vertex determination, event triggering and centrality selection.

The Pioneering High Energy Nuclear Interaction eXperiment, (PHENIX), is designed to measure direct probes of the collisions such as electrons, muons and photons with good momentum and energy resolution. It consists of a large acceptance charged particle detector and four spectrometer arms - a pair of which is used for detecting electrons, photons, and hadrons at mid-rapidity, the other pair of spectrometers

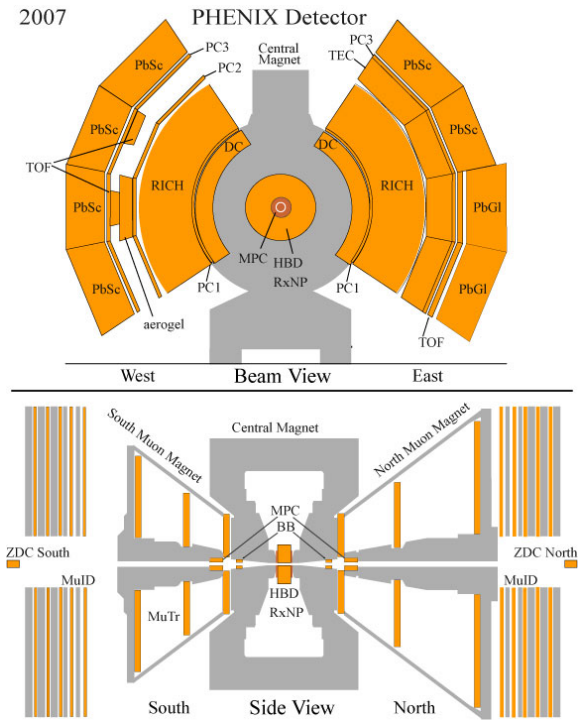

Figure 2.9: A schematic diagram of the PHENIX detector

detecting muons at forward rapidity (see fig. 2.9). There also are additional sub-detectors for event characterization, which provide information about the collision, such as is a beam-beam counter, which consists of two arrays of quartz Cherenkov telescopes surrounding the beam, and a multiplicity and vertex detector composed of concentric barrels of silicon strip detectors together with end-caps of Si pad detectors. PHENIX has also electromagnetic calorimeters mounted outside each of the two central arms.

The Solinoidal Tracker At Rhic (STAR) detector shown in fig. 2.10, is designed primarily for the measurement of hadron production over a large solid angle. It is a large acceptance detector which covers the full azimuthal ($0 \leq \Phi \leq 2\pi$) for $|\eta| < 1.8$

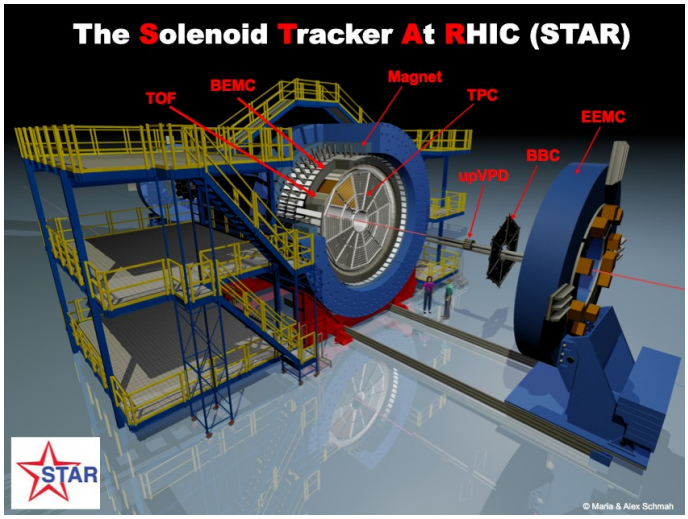

Figure 2.10: A schematic of the STAR detector - 2012

and $2.5 < |\eta| < 4.0$. It consists of second biggest working Time Projection Chamber (TPC) for particle tracking. The data for my dissertation work come from the STAR detector. STAR also has a number of sub-detectors, some of which will be discussed in detail in the following sections.

2.3 The STAR experiment

The STAR [36, 37] detector evolved in its subcomponent configuration over the past 12 years. The present configuration is shown in fig. 2.11 with most of its subcomponents. It is located at the 6 o$'$clock position in the RHIC complex as shown in fig. 2.2. It has been built to study nucleus-nucleus collisions at RHIC. The collaboration comprises of 57 institutions from 12 countries, with a total of $\sim$ 552 collaborators.

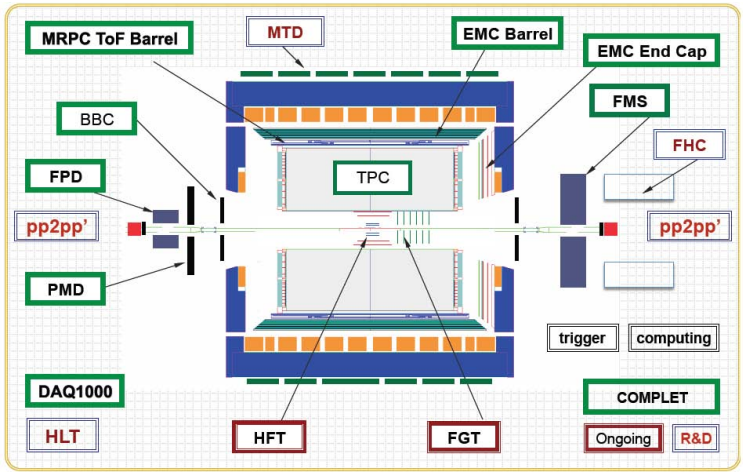

Figure 2.11: Cutaway side view of the STAR detector in year 2008 run and future upgrades

The STAR detector is capable of measuring hadron production over a large solid angle, using detector systems [38] for high precision tracking, momentum analysis, and particle identification in a region surrounding the center-of-mass rapidity. The large acceptance of STAR with full azimuthal and wide pseudo-rapidity coverage makes it suit for event-by-event characterization of heavy ion collisions and for the detection of hadron jets. Figures 2.10 and 2.11 in combination give a very good overview of the STAR detector. Its main components are a large Time Projection Chamber (TPC), a Time of Flight (TOF) patch, a Barrel ElectroMagnetic Calorimeter (BEMC), an EndCap ElectroMagnetic Calorimeter(EEMC), a Forward Gem Tracker(FGT), and a Heavy Flavor Tracker(HFT) all inside a room temperature solenoidal magnet [90] (the solid blue shield on figure 2.11) with a maximum magnetic field of 0.5 T which provides a uniform magnetic field for charged particle momentum analysis. Outside the STAR magnet we have a Photon Multiplicity Detector(PMD), a Forward Pion

Detector(FPD), a Forward Meson Spectrometer(FMS), a Muon Telescope Detector(MTD), and pp2pp as main particle tracking detectors. STAR also has a beam-beam calorimeter(BBC) and zero-degree calorimeter(ZDC) (behind the EEMC as shown in figure 2.10) and a Vertex Positioning Detector(VPD) as main triggering detectors. In the following, we will mainly discuss the STAR trigger, STAR magnet, and TPC since the heart of this thesis work is based on the data obtained with those sub-detector components. Further details about the STAR detector can be found in [39].

2.3.1 STAR trigger

The process of selecting events is known as triggering and is useful for collecting rare or selected events without the need for recording vast quantities of unwanted data. The Central Trigger Barrel(CTB), Beam-Beam Counter(BBC; mainly for p+p collisions), Zero-Degree Calorimeter (ZDC) and Electro Magnetic Calorimeter(EMC) can be identified as fast STAR trigger detectors. The purpose of the trigger detectors is to enable event selection criteria to be applied at a rate greater than that of which the slow detectors operate. The STAR experiment implements a pipelined trigger system comprising four levels, designed to simultaneously handle several triggers with different criteria, and to operate at the RHIC bunch crossing frequency of approximately 10 MHz [40]. Since the various detector subsystems in STAR have different readout speeds, which are slower than the bunch crossing rate, not all events can be recorded by the data acquisition system (DAQ). Therefore, the STAR trigger system selects events based on the input from the fast detectors. The four different

trigger levels used in STAR are labeled 0-3, with level-0 being the fastest. Successive levels utilize increasingly detailed descriptions of the event and are correspondingly afforded larger time budgets to complete their operations. The fast detectors used for triggering level-0 in heavy ion collisions are the two ZDCs (east and west), the CTB and EMC. For p+p collisions also the BBC is utilized. The decision to store an event in HPSS data storage is made at level-3, which is the final level and a software trigger, where information from fast and slow detectors are available. The level-0 trigger issues the decision to progress to level-1 for a selected event which matches the trigger criteria. The typical time for this process is within 1μs after the interaction took place. The command issued by the level-0 trigger specifies the relevant slow detector configuration for that specific event and initiates data recording using those slow detectors. During this time period those slow detectors produce their signal, level-1 trigger checks the fast detector information for background contamination and issues the decision of passing the event to level-2 if the triggered event is clean. At level-2, the entire set of information from the fast detectors is analyzed under further constraining cuts. Level-2 is also used to isolate the events carrying rare signatures like jets. The typical processing times for level-1 and level-2 trigger are $\sim$ 100μs and $\sim$ 5ms, respectively. If a triggered event passes all those trigger stages, the information is passed to the DAQ where the L3 trigger [41] finally decides whether to store the triggered information in the BNL storage farm. The L3 trigger bases its decision on the complete online reconstruction of the event. This particular trigger also includes a display which allows the visual inspection of the events almost in real time. Further detailed information can be found at [42].

2.3.2 STAR magnet

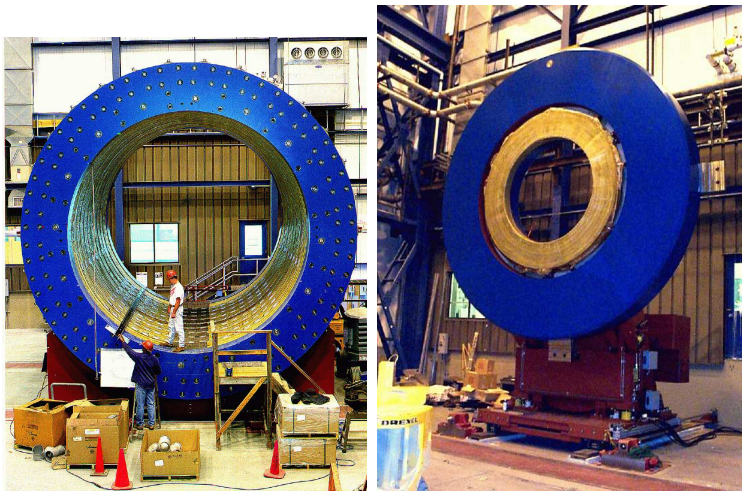

Figure 2.12: Left: Space trim and main magnet coil. Right: Pole tip trim magnet coils [171]

At the heart of STAR tracking is the magnetic field produced by the solenoidal magnet in the experiments. Three main components can be identified in generating the required magnetic field; Main coil, Space trim coils, and Poletip trim coils (see fig. 2.12). Most of the field of the magnet is produced from the Main coils. The Trim coils are used to reduce distortions. The high current in the solenoid coils ($\sim$ 4500A) generates large heat and thus a liquid cooling system is used to maintain the temperature of the magnets. The momentum information of the charged particle tracks in TPC is extracted using the magnetic field. The field has to be large enough to measure the momentum of high energy ion tracks. Increasing field strength compensates the lowest momentum cut off for tracks measured in the STAR TPC. The maximum field strength applied for data taking is 0.5T parallel to the beam direction

(z - direction) with an operating range of $0.25 < |B_Z| \leq 0.5$ T. The reproducibility of the absolute field is better than $\pm$ 0.5 Gauss. A uniform magnetic field is established over the entire TPC volume via the use of dedicated design studies and manufacturing criteria [43,44].

2.3.3 STAR TPC - The main tracking detector in STAR

The STAR detector consists primarily of a 4.2 m long cylindrical ion drift chamber, called a Time Projection Chamber (TPC), with a beryllium beam pipe running along the axis [36]. The outer radius of the detector is 2 m, the inner radius is 50 cm away from the collision vertex (see fig. 2.11). The typical TPC measures three dimensional space points along charged particle trajectories and is a large gas-filled detector. TPCs are designed to minimize the disturbances (electrical and magnetic field fluctuations) and make many space point measurements along a particles original path (trajectory). The minimum ionization region or active volume of the TPC is 45 m^3. This volume is kept slightly above atmospheric pressure to make sure that atmospheric gases do not enter the active TPC volume filled with 10% CH_4 and 90% Ar gas. This gas is also known as P10 gas.

The TPC consists of an outer and inner field cage to maintain electric field (see fig. 2.13) uniformity using equipotential surfaces, and the drift potential is maintained between each grounded end and a thin circular membrane at its midpoint (at -28 kV). Due to the applied magnetic field, a charged particle traversing the chamber follows a helical path. It ionizes nearby atoms and liberated electrons drift towards

the nearest end of the chamber at $\approx$ 5 cm/μs under the influence of a 147 V/cm electric field between the central membrane and end caps of the TPC. The cathode captures positive ions at the central membrane and the electron clouds drift towards the ends of the detector which sits at a higher potential. At the cathode plane, the positive ions are neutralized and a Multi-wire Proportional Chamber (MWPC) close to the end caps amplifies the electron clouds. Electrons meet a gating grid at the end of the drift region beyond which lies a proportional region, as shown in fig. 2.14. If an event needs to be recorded after passing the trigger criteria, the gating grid is opened (see fig. 2.15), by setting it to the ambient potential. This potential is essentially the equal potential value corresponding to the position of the gating grid wires.

Figure 2.14 shows the three wire planes of MWPC. Closest to the end cap pad planes lie the anode wires which are 20 μm in width. The inner sector anode wires are set to 1170 V and the outer to 1390 V. As the drift electrons accelerate towards the anode wires at high positive voltage, they create ionization avalanches. These avalanches also create positive ions and those positive ions produce image charges on the TPC end cap pad plane.

The amplification region is separated from the drift volume through the shield grid wire plane. The shield grid is a multi purpose wire plane. Firstly, it functions as a ground plane for the drift field. Secondly, it shields the pad plane from the gated grid and finally, it captures some of the positive ions created near the anode wires. The drift field is established between the -28 kV central membrane and grounded shield plane. The opening of the gated grid causes signals to be induced on the TPC pads.

These induced signals are significantly reduced by the shield grid. This prevents the induced signals from compromising the resolution of ionization signals at the beginning of the drift period. Slowly drifting positive ions created near the anode wires are neutralized on the wires of the shield grid in large fractions. Distortions in the drift field are caused by positive ions that drift into the active volume and leakage current.

The gated grid is furthest from the pad plane. The main purpose of the gated grid is to stop positive ions created in the amplification region that leak past the shield grid from reaching the active volume and stop non-triggered ionization from reaching the amplification region. Preventing unnecessary ionization from occurring in the amplification region extends the lifetime of the TPC. This is achieved by stopping non-triggered electrons. More importantly, since positive ions take a longer time to drift past the gated grid compared to the time that the gated grid is open this last wire plane neutralizes the positive ions that leak past the shield grid. The electric field lines for both open and closed gated grid states are shown in fig. 2.15. In the closed state, by alternating the adjacent gated grid wire potentials from positive to negative, an electric fields is established between the adjacent wires which is perpendicular to the drift direction. The established electric fields capture both non-triggered electrons and positive ions. In the opened state, the voltage on the gated grid wires is set to the corresponding equipotential surface of the drift field. In this state the gated grid is transparent to the drift electrons.

The TPC pads are laid out in sectors that cover 30 ° in azimuth, as shown in fig.

2.13(a). There are 24 identical sectors mounted on the east and west ends of the TPC. Each sector contains 32 outer and 13 inner pad rows, as shown in fig. 2.16. The pads operate as plate capacitors. In order to improve the two track resolution the inner sector pads are made smaller. The TPC diffusion limit constraints the size of inner sector pads. Altogether, each inner and outer sector combined has a total of 5,690 pads which corresponds to a total of 136,560 channels for all 24 TPC sectors. The slowly drifting positive ions created in avalanches near the anode wires induce local electric field changes on the surface of the TPC pads. These local field changes induce currents on the pads and subsequently in the TPC electronics.

The readout electronics boards of the TPC are mounted on the back of each sector. Each sector carries 181 analog Front End Electronics boards which are known as FEE cards and 6 digital readout boards (RDOs). The circuitry on each FEE is capable of covering up to 32 pads via using two parallel 16 channel circuits. The TPC pad analog signals are shaped, amplified, stored, and digitized in two circuits on the Front End Electronics card. Each pad is read 512 times for a triggered collision, which leads to a time interval of ≈ 100 ns. A weighted average of the drifting charge element is taken as the signal. Each signal will often cover several time intervals due to diffusion, and the extracted mean is used to determine the z position of the element. The recorded x, y, z position is thus known as a hit. Around ≈ 70 million pixels are available in total in order to take a 3D picture of the charged particles emerging from an event. Upon request the stored voltages on the capacitors are digitized and passed onto a multiplexer on the RDO board. The multiplexer on

the RDO board communicates via fiber optic links with the data acquisition (DAQ) crates. These crates are responsible for packing the data into DAQ files and shipping them to a High Performance Storage System(HPSS). The data are later retrieved from HPSS for online analysis.

The apparent x, y, z position is not quite the true position due to factors distorting the motion of the drifting element. Therefore corrections have to be applied to correct for the distortions due to non-uniformities in the electric and magnetic fields. After applying the corrections, we proceed to the track reconstruction phase in data production.

Track reconstruction is done in two steps. The first step is known as cluster finding. In cluster finding, contiguous regions of ionization are localized within the same pad row. For each of these clusters, the total charge and the center of gravity of the charge distribution is recorded. The final result of this step is a set of space points, where charged particles ionized the drift gas. In the next step, known as track finding, clusters corresponding to the same particle have to be identified and combined to form tracks. Since the charged particles move in a homogeneous magnetic field these tracks are fitted with the model of a helix. The curvature of the helix in the transverse plane caused by the magnetic field is used to calculate the momentum of the charged particles. Thus the resolution of the curvature (i.e. the spatial resolution of the TPC) determines the momentum resolution of the charged particle tracks in TPC. Finally, the TPC also has limited particle identification capabilities. As described by the Bethe-Bloch formula shown below, a TPC can measure the specific energy loss of charged particles in a medium.

$$\frac{dE}{dX} = -\frac{2\pi N_A z^2 e^4}{mc^2\beta^2}\frac{\rho Z}{A}\left\{ln\frac{2mc^2\beta^2 E_M}{I^2(1-\beta^2)} - 2\beta^2\right\} \tag{2.1}$$

The only particle properties entering the formula are its charge z and the velocity β of the particle traversing the TPC gas. The related drift gas properties are mass number A, atomic number Z, specic ionization I and density ρ. E_M is the maximum energy transfer in one interaction. The charge e and mass m of the electron, the speed of light c and the Avogadro number N_A enter into the Bethe-Bloch formula as described in [47]. As most of the particles seen by the TPC carry a single unit charge e, the ionization is simply a function of the velocity β of the particle. Figure 2.17 shows the specic energy loss for different particle species.

Table 2.2: RHIC parameters

parameter name	value
Top injection kinetic energy for Au	8.86-100 GeV/u
Top injection kinetic energy for Protons	23.4-250 GeV
Luminosity for Au+Au @ 100GeV/u	$\sim 2\times 10^{26} cm^{-2} s^{-1}$
No. of bunches/ring	112
No. of Au-ions/bunch	1×10^{9}
bunch length	1.52 m
Beam lifetime for Au @ $\gamma > 30$	$\sim$5 h
Circumference	3833.845 m
Beam separation in arc sections	90 cm
Number of crossing points	6
Magnetic rigidity, Bρ: @ injection	81.114 Tm
Magnetic rigidity, Bρ: @ top energy	839.5 Tm
No. of dipoles(192/ring + 12 common)	396
No. of quadrupoles	492
Dipole field @ 100GeV/u, Au	3.458 T
Beam tube internal diameter	6.9 cm
Operating temperature via liquid He	<4.6 K
Beam stored energy	$\sim$ 200 kJ

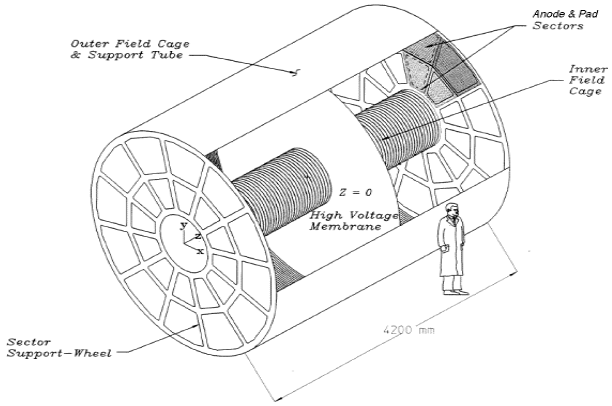

(a) Cylindrical geometry of the STAR TPCs gas volume and the sector layout on the end-caps.

(b) Inside STAR Time Projection Chamber

Figure 2.13: The STAR Time Projection Chamber

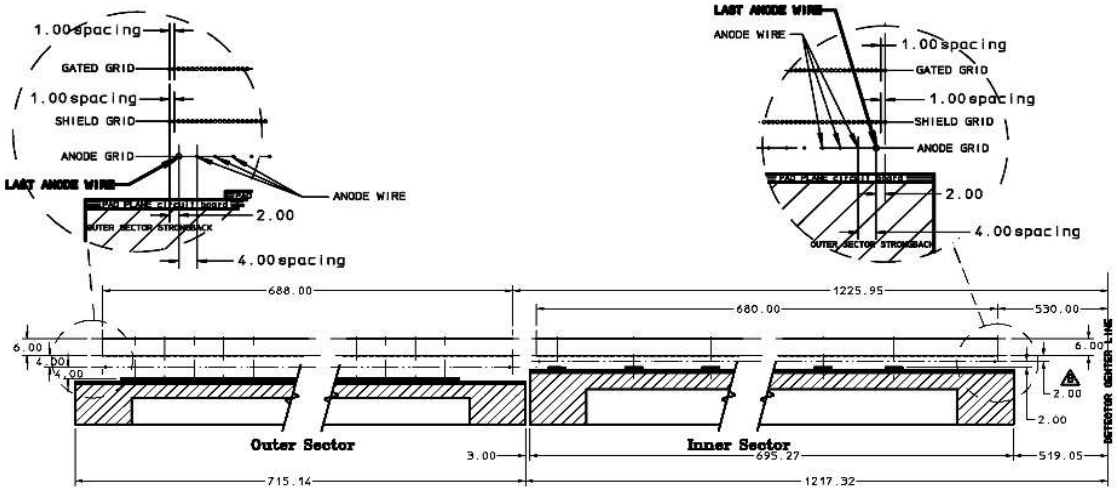

Figure 2.14: A cutaway view of an sub-sector pad plane. The cut is taken along a radial line from the center of the TPC to the outer field cage so the center of the detector is towards the right hand side of the figure. The figures shows the spacing of the anode wires relative to the pad plane, the ground shield grid, and the gated grid. The bubble diagram shows additional detail about the wire spacing. The inner and outer sub-sector pad plane has the same layout except the spacing around the anode plane is 2 mm instead of the 4 mm shown here. All dimensions are in millimeters [32].

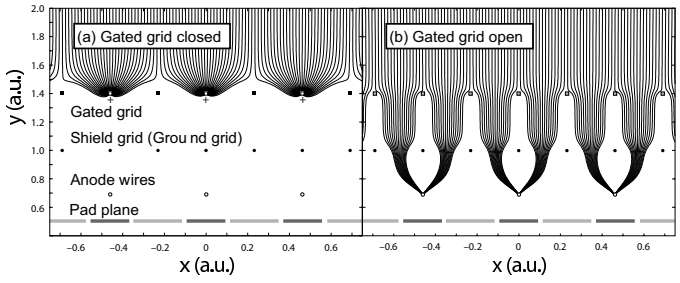

Figure 2.15: The closed (a) and open (b) states of the a gated grid. The electric field lines of the two configurations are indicated. In the closed state electrons drift to and terminate on the gated grid wires. In the open state the wires are transparent to drifting electrons [46].

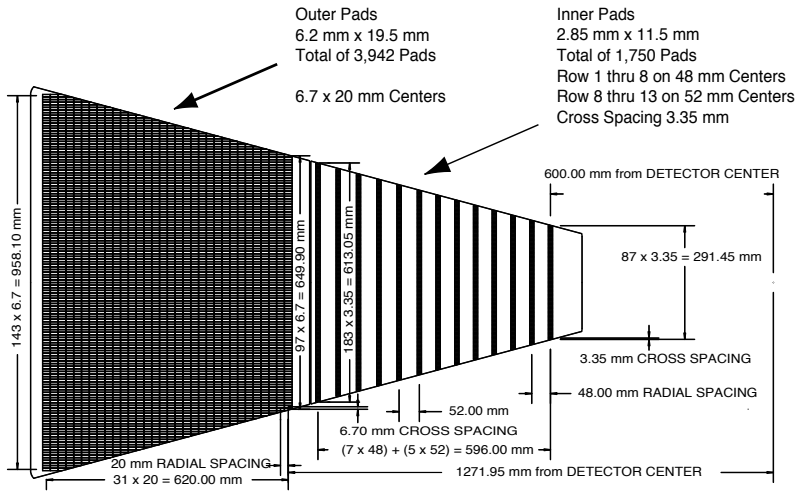

Figure 2.16: Pad plane of one TPC sector. Each sector contains 5692 pads. The inner and outer pad geometries differ to compensate for the radially decreasing hit density [32].

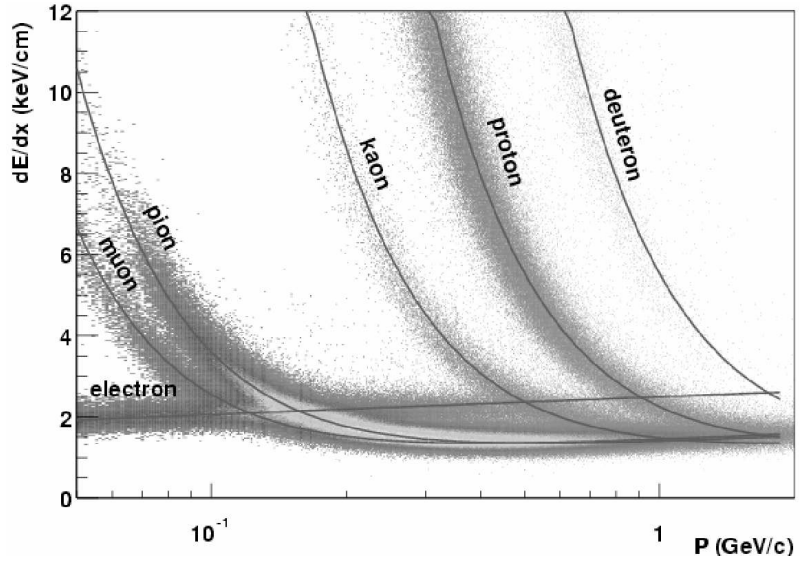

Figure 2.17: The energy loss distribution for primary and secondary particles in the STAR TPC as a function of the p_T of the primary particle [48].

Chapter 3

Di-hadron correlation: definition and approach

In 2001 the **CERN** press release [49] presented compelling evidence for the existence of new state of matter, based on data from **SPS** experiments. This evidence, along with many additional experimental observations, was awaiting confirmation at higher energies using **RHIC** data. In section 1.4 we discussed such evidence for the existence of this new state of matter (**QGP**). In this chapter we discuss in detail one particular set of measurements, namely fluctuations and correlations [50].

3.1 Fluctuations and correlations

The study of fluctuations is essential in exploring the expected **QCD** phase transition as thermodynamic properties are expected to show dynamical fluctuations away from

their mean value near a phase boundary.

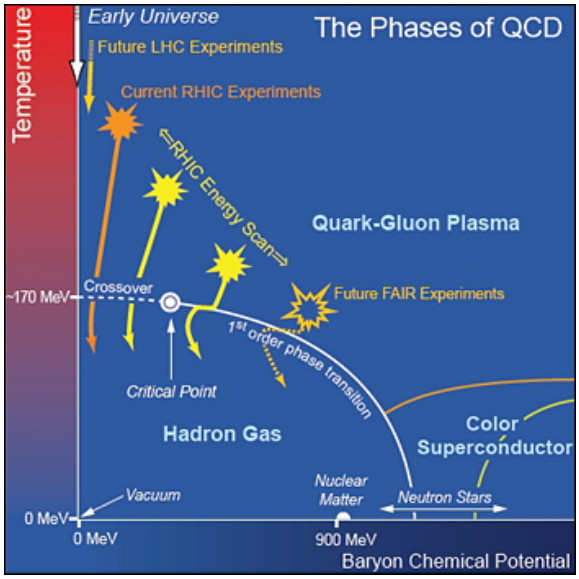

Figure 3.1: The proposed QCD phase diagram

In any fluctuation analysis the main focus is to devise a measurement to minimize the statistical and background fluctuations in order to detect the fluctuations due to phenomena of interest [50]. The complexity of devising such a measurement led to many different approaches, measures, and conclusions. Nonetheless, all fluctuation measurements have an essential mathematical component: an integral of covariance. The analysis method we adopt in our study is motivated by the fundamental importance of that component.

One of the simplest measurements to understand is the analysis of event by event transverse momentum fluctuations. The quantity of interest in this measure is the average transverse momentum, i.e. the scalar sum of all charged particles within the kinematic acceptance of the detector. For an event we can define the quantity as:

$$\langle p_T \rangle = \frac{1}{N} \sum_{i=1}^{N} p_{t,i} \tag{3.1}$$

where index i is used to index a particle in an event and N is the total number of tracks in an event which is also called multiplicity. The above definition suffers biases due to random statistical fluctuations in number of particles and momentum distribution of particles event by event. Clearly, any fluctuation in either quantity affects the final measurement. Therefore, instead of measuring $\langle p_T \rangle$ according to equation 3.1, one can introduce measurements to separate random statistical fluctuations from actual p_T fluctuations. The above measure is also susceptible to detector acceptance, or more generally, scale dependence. All fluctuations have a characteristic length or a scale which can be observed. Depending on the detector acceptance, experiments may lose information from certain characteristic fluctuations while others survive. While detector acceptance sets one limiting case, any histogram binning scale will define additional limits in sampling fluctuations. Its upper limit sets one limit while the single particle limit (each occupied bin contains exactly one particle) can be achieved by making the bin size smaller. Studying scale dependence is not only useful in revealing measurement biases, it can also be used to extrapolate between detectors that have different acceptance. A detailed study of how to minimize scale dependence and random fluctuations can be found in [51].

The authors have devised an improved statistical measure defined as:

$$\Delta\sigma^2_{p_t:n} \equiv \frac{1}{\epsilon}\sum_{j=1}^{\epsilon} n_j[\langle p_t\rangle_j - \hat{p}_t]^2 - \sigma^2_{\hat{p}_t} \tag{3.2}$$

$$\equiv 2\sigma_{\hat{p}_t}\Delta\sigma_{p_t:n} \tag{3.3}$$

where $\hat{p}_t$ and $\sigma^2_{\hat{p}_t}$ are mean and variance of the parent p_t distribution which is sampled by all charged particles from all events, ϵ is the number of events per centrality bin, j is the index used to represent an event and n_j, $\langle p_t\rangle_j$ are the multiplicity and mean p_t of event j, respectively. Equation 3.2 defines the fluctuation measurement as a variance excess. The detailed studies [51] of this fluctuation measure demonstrate that issues related to random fluctuations and scaling can be overcome.

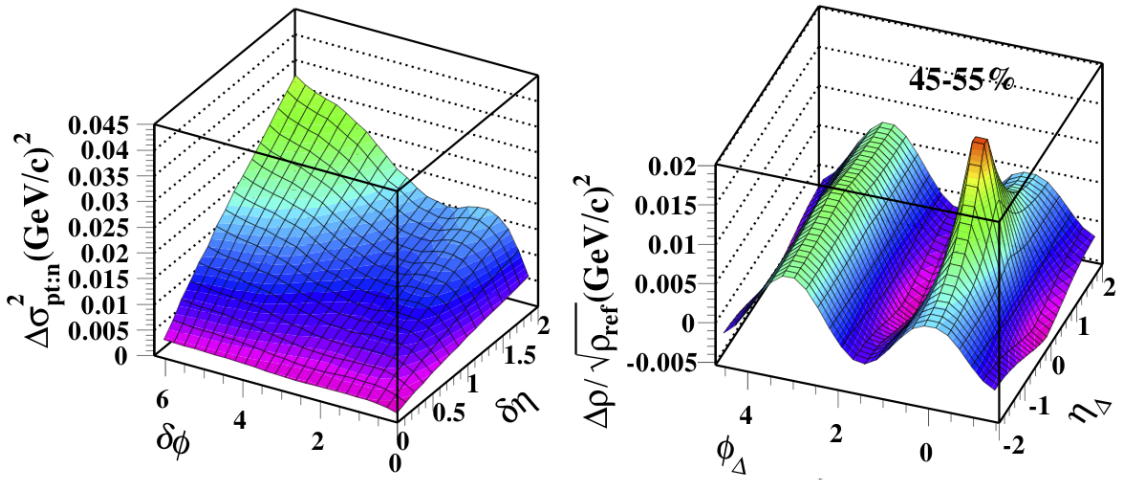

Figure 3.2: Left panel: $\delta\eta - \delta\phi$ scale dependence of $\Delta\sigma^2_{p_t:n}$. Right panel: The corresponding p_t correlation from inversion [52].

The left panel in figure 3.2 shows the scale dependence of the fluctuation quantity $\Delta\sigma^2_{p_t:n}$ as a function of $\delta\eta$ and $\delta\phi$. The apex of maximum scale corresponds to the full

STAR TPC acceptance. Fluctuations corresponding to characteristic lengths larger than full STAR-TPC acceptance will not contribute on average. A typical di-hadron correlation analysis has a fixed $\delta\eta$ and $\delta\phi$ which restricts the sensitivity to possible fluctuation information.

In our analysis we focus on studying the angular distribution of correlated particles in $\Delta\eta$ and $\Delta\phi$. To obtain this angular distribution information we infer the common mathematical property shared by all fluctuation measures; the fact that they all depend on an integral of covariance. Instead of integrating over covariance to measure fluctuations, we directly measure the covariance and normalize it appropriately to construct the well known Pearson's correlation coefficient [53]. Any correlation representation has differential information compared to a fluctuation measure, thus connecting better with physical mechanisms.

A detailed formalism of the connection between correlations and fluctuations can be found in [54]. Meanwhile a simplified relationship between the two can be written as:

$$\Delta\sigma^2_{p_t:n}(\delta\eta,\delta\phi) = 4\epsilon_\eta\epsilon_\phi \sum_{i,j} K \frac{\Delta\rho(p_t:n)}{\sqrt{\rho_{ref}(n)}}(i\epsilon_\eta, j\epsilon_\phi) \tag{3.4}$$

where $\frac{\Delta\rho}{\sqrt{\rho_{ref}}}$ is a, per final state, charged particle correlation density related to Pearson's correlation coefficient, K is a kernel that contains histogram binning information, ϵ_x is a bin width with indices i and j corresponding to a correlation bin, and δx represents a fluctuation scale. It is possible to invert equation 3.4 to obtain the correlation measure $\frac{\Delta\rho}{\sqrt{\rho_{ref}}}$ from the fluctuation measurement $\Delta\sigma^2_{p_t:n}$. The right panel

on figure 3.2 shows the corresponding correlation structure for the apex of the maximum scale on the left panel figure. Thus figure 3.2 right panel provides the correlated angular distribution that is responsible for the observed non-statistical fluctuations.

3.2 Correlation function formalism

Our formalism follows a random variable sampling of an unknown parent distribution. The random variables we study are the summed kinematic quantities of particles and pairs in histogram bins. We follow the standard statistical approach by inferring the parent distribution properties analyzing a large number of events.

3.2.1 Pearson's correlation coefficient

The mean or average value of x_i (i = *1,2,3, ... N*) data points in a distribution is defined as,

$$\bar{x} = \frac{1}{N}\sum_{i=1}^{N} x_i \tag{3.5}$$

and the variance, which tells us how far the data points are spread out from the mean, is defined as,

$$\sigma_x^2 = \frac{1}{N}\sum_{i=1}^{N}(x_i - \bar{x})^2 \tag{3.6}$$

The covariance measurement is used to determine how much two random variables vary together or in other words how correlated the two random variables are. For two data sets x_i and y_i the covariance is defined as,

$$Cov(x, y) = \frac{1}{N} \sum_{i=1}^{N} (x_i - \bar{x})(y_i - \bar{y}) \tag{3.7}$$

In the case where y=x, the above definition reduces to the variance of a random variable. As shown below, the Pearson's correlation coefficient can be obtained by normalizing the above covariance appropriately.

$$R_{xy} = \frac{Cov(x, y)}{\sigma_x \sigma_y} \tag{3.8}$$

$$= \frac{\sum_{i=1}^{N} (x_i - \bar{x})(y_i - \bar{y})}{\sqrt{\sum_{i=1}^{N} (x_i - \bar{x})^2 \sum_{i=1}^{N} (y_i - \bar{y})^2}} \tag{3.9}$$

The range of values R can vary is between -1 and +1 and can be proven by substituting $y_i = \pm x_i$ in the above equation. For perfectly correlated data, R takes the value +1, for perfectly anti-correlated data R takes the value -1 and for uncorrelated data R takes the value 0. This can be further understood by looking at figure 3.3.

3.2.2 Application of autocorrelations

The concept of autocorrelations was first introduced in the statistical description of Brownian motion by Einstein in 1905 [55, 56]. It was expanded by contributions from many great scientists including Wiener, Langevin, and Einstein. In autocorrelations

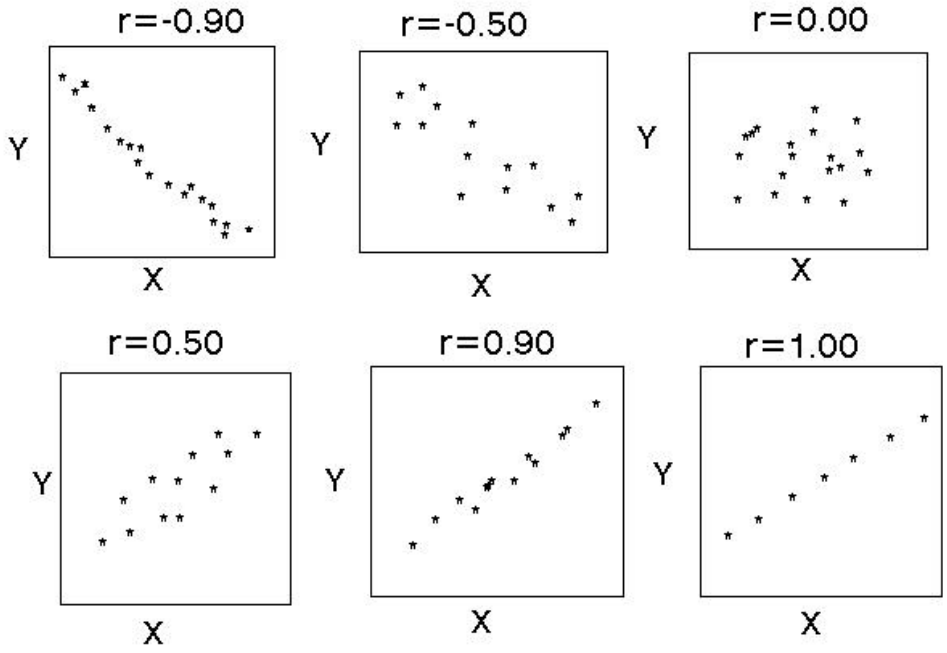

Figure 3.3: Degree of correlations using few data points.

we try to invoke the correlations within the same variable rather than between two separate variables. An example using a time series (a time varying quantity) justifies the existence of such correlations within a one dimensional distribution. The amplitude at the time step i (or some quantity that is measured at time step i) is denoted as x_i. The correlation between the measured quantities at time step i+1 (of the same quantity) and i is studied. Letting $y_i = x_i + 1$ in equation 3.9, R_{xy} measures the degree of independence between one point and the next averaged overall points. For an arbitrary time difference k the equation 3.9 becomes,

$$R_k = \frac{\sum_{i=1}^{N-k}(x_i - \bar{x})(x_{i+k} - \bar{x})}{\sum_{i=1}^{N-k}(x_i - \bar{x})^2} \tag{3.10}$$

The application of correlations and autocorrelations in RHIC physics uses histogram binning of the information in a single ion-ion collisions. We bin the histograms as a function of an arbitrary quantity x. Let $\mathbf{n_i}(\mathbf{a})$ denote the number of particle count in bin $\mathbf{a}$ for event i. The measure of correlation between any two bins $\mathbf{a}$ and $\mathbf{b}$, corresponding to quantity x, averaged over all N events can be written as follows.

$$R_{ab} = \frac{1}{N}\sum_{i=1}^{N}\left\{n_i(a) - \overline{n(a)}\right\}\left\{n_i(b) - \overline{n(b)}\right\}/\sigma_a\sigma_b \tag{3.11}$$

$$= \overline{(n-\bar{n})_a(n-\bar{n})_b}/\sigma_a\sigma_b \tag{3.12}$$

The over-bar on the second line represents the event average along with the bin indices as subscripts.

An autocorrelation among these histogram bins can be defined by measuring the relative displacement. Thus the autocorrelation measures the correlation between $\mathbf{n}(\boldsymbol{x})$ in bin $\mathbf{a}$ and $\mathbf{n}(\boldsymbol{x} + \Delta x)$ in bin $\mathbf{a} + \mathbf{k}$ as a function of Δx averaged over x. In other words this measurement tells us how particles will be distributed about a particular particle on average. Thus the histogram form of equation 3.10 is as follows.

$$R_k = \frac{1}{x_{max} - k} \sum_{a=1}^{x_{max}-k} \overline{(n - \bar{n})_a (n - \bar{n})_{a+k}} / \sigma_a \sigma_{a+k} \tag{3.13}$$

In any di-hadron correlation measurement particle pair quantities need be constructed. All above correlation measures give us particle pair yields. However there are many practical concerns arising in using pre-binned single particle distributions to make the correlated pair distributions. We list some of those concerns below.

- Loss of information in the histogram binning process.
  - When calculating the difference in physical quantities Δx, it is approximated as the difference between bin centers. However, depending on the position where particles fall within their respective bins, the difference may be shifted by one bin from the actual value
- Pair-wise tracking inefficiencies.
  - It is difficult to resolve the information from two nearby tracks

Because of the above concerns, we proceed with direct binning of individual particle pairs instead of using pre-binned single particle distributions.
It is important to note at this point that the covariance can be expressed in terms of particle pairs. The numerator in equation 3.12 corresponds to the covariance. It can be re-written as follows.

$$\overline{(n - \bar{n})_a (n - \bar{n})_b} = \overline{n_a n_b} - \overline{n_a}.\overline{n_b} \tag{3.14}$$

The first term on the right-hand side of equation 3.14 represents the total number of pairs in bin (**a**, **b**), event-wise averaged for a two-dimensional histogram of particle pairs (e.g. ϕ_1, ϕ_2). The second term calculates the statistical reference of the expectation when **a** and **b** are uncorrelated. Particles in a particular event are combined to form all possible pairs. Using a two-dimensional histogram, the distribution of these pairs is measured. Thus we have a measurement of the first term on the right hand side of equation 3.14. We refer to them as sibling pairs. The second term is measured by taking the two particles from two independent (uncorrelated) events and we refer to them as mixed pairs. A detailed discussion about the relationship between single particle and particle pair histograms can be found in [57]. In the following we demonstrate the equivalence between the single particle bins and particle pairs for sibling and mixed events formalism. We define $n_{i,a}$ as the number of particles in bin a for event i with ϵ total events.

$$
\begin{aligned}
Cov(a,b) &= \overline{n_a n_b} - \overline{n_a}.\overline{n_b} \\
&= \overline{n_a n_b} - \frac{1}{\epsilon^2}\sum_{i=1}^{\epsilon}\sum_{j=1}^{\epsilon} n_{i,a}n_{j,b} \\
&= \overline{n_a n_b} - \frac{\epsilon(\epsilon-1)}{\epsilon^2}\frac{1}{\epsilon(\epsilon-1)}\sum_{i=1}^{\epsilon}\sum_{j=1,j\neq i}^{\epsilon} n_{i,a}n_{j,b} - \frac{1}{\epsilon^2}\sum_{i=1}^{\epsilon} n_{i,a}n_{i,b} \\
&= \left(1-\frac{1}{\epsilon}\right)\overline{n_a n_b} - \frac{\epsilon-1}{\epsilon}\frac{1}{\epsilon(\epsilon-1)}\sum_{i=1}^{\epsilon}\sum_{j=1,j\neq i}^{\epsilon} n_{i,a}n_{j,b} \\
&= \frac{\epsilon-1}{\epsilon}\left[\overline{n_a n_b} - \frac{1}{\epsilon(\epsilon-1)}\sum_{i=1}^{\epsilon}\sum_{j=1,j\neq i}^{\epsilon-1} n_{i,a}n_{j,b}\right] \\
&= \frac{\epsilon-1}{\epsilon}[\overline{n_a n_b} - \overline{n_a}.\overline{n_{b\,mixed}}]
\end{aligned}
\tag{3.15}
$$

The factor in front of the square brackets approaches unity for a large number of events. Thus the derivation in equation 3.15 shows the equivalence between the two formalisms.

Next we need to derive a term for the denominator in equation 3.12 in terms of particle pairs. In our approach, the number of particles we are detecting in a given detector volume during a very short period of time is discrete. Therefore the particle detection can be approximated by a Poisson process. The mean and variance of a Poisson distribution take the same value. Using this fact we can re-write the denominator in equation 3.12 as $\sigma_a\sigma_b \approx \sqrt{\overline{n_a}.\overline{n_b}}$. The term inside the square root yields a particle pair quantity constructed from mixed pairs in bin (**a**, **b**). Finally, the autocorrelations can be obtained either by using the definition for R_k or by directly binning the histogram for the difference variable $\Delta x \equiv x_1$ - x_2 [57].

3.2.3 Correlation measure

The constructed sibling and mixed pair densities relate to equation 3.12 as shown below.

$$\frac{\Delta\rho}{\sqrt{\rho_{ref}}} = \frac{\overline{(n-\bar{n})_a(n-\bar{n})_b}}{\sqrt{\overline{n_a}.\overline{n_b}}} \tag{3.16}$$

Here $\Delta\rho \equiv \rho_{sib} - \rho_{ref}$ where ρ_{sib} is the sibling pair density and ρ_{ref} is the mixed pair density. As ρ_{sib} contains both correlated and uncorrelated pairs, after subtracting out ρ_{ref}, $\Delta\rho$ is proportional to the correlated pair density. The denominator $\sqrt{\rho_{ref}}$ is proporsional to the number of particles since ρ_{ref} represents the number of

uncorrelated pairs. Therefore our correlation measure is proportional to the correlated pairs per particle.

In any correlation study, extra care needs to be taken for correcting experimental artifacts such as inefficiencies, acceptance issues and loss of track information in the reconstruction process. Both sibling and mixed pair distributions suffer from those experimental artifacts. Additionally the sibling pairs also suffer from losing pairs due to two track inefficiencies. To correct for the common experimental artifacts between the two pair distributions we construct the ratio $r = \frac{\rho_{sib}}{\rho_{ref}}$. We can now re-write the correlation measure as:

$$\frac{\Delta\rho}{\sqrt{\rho_{ref}}} = \sqrt{\rho_{ref}}\frac{\Delta\rho}{\rho_{ref}} \tag{3.17}$$

$$= \sqrt{\rho_{ref}}(r-1) \tag{3.18}$$

However it is evident in equation 3.18 that we again introduce the effects to due artifacts by multiplying with $\sqrt{\rho_{ref}}$. An idealized $\rho^{'}_{ref}$ can be constructed assuming longitudinal boost invariance and azimuthal symmetry. This idealized $\rho^{'}_{ref}$ has been corrected for experimental artifacts and can be formed using $\frac{dn}{d\eta}$ at $\eta = 0$ [58]. The corrections due to two track efficiencies will be discussed briefly under section 3.2.4. Before applying the ratio r, we need to make sure that the events used to construct the average pair densities have similar structure. Otherwise we loose efficiency in removing the experimental artifacts by not canceling the effects when calculating the ratio r. This is taken care of by analyzing events in appropriate multiplicity windows Δn and primary z vertex location Δz.

After grouping events in these Δn and Δz windows the sibling and mixed pair distributions are constructed by averaging over selected events. The number of pairs are divided by the area of a correlation bin to construct the average number of pairs per unit area (pair density). Afterwards the total average mixed pairs are normalized to the total average sibling pairs according to the construction of ratio r. Finally the correlation measure within a specific centrality bin is obtained by taking the pair weighted average over all Δn and Δz bins. The final form of the correlation measure can be written as:

$$\frac{\Delta\rho}{\sqrt{\rho_{ref}}}(a,b) = \sqrt{\rho'_{ref}}[r(a,b) - 1] \tag{3.19}$$

The above measures correlated pairs per particle in the two-dimensional histogram bin (**a**,**b**). The binning corresponds to angular difference variables $(\Delta\eta, \Delta\phi)$ in the thesis work presented. In general the bin index could be any kinematic quantity related to a particle.

3.3 Analysis details

In this section we mainly discuss the specific event selection cuts, track selection cuts and corrections for the sibling pair loss.

3.3.1 Event selection cuts

The results presented here are based on three data sets taken by the STAR detector at RHIC. We have analyzed run 4 (2003 - 2004) central trigger Au+Au data at $\sqrt{S_{NN}}$ = 200 GeV, run 5 (2005) minimum bias Cu+Cu data at $\sqrt{S_{NN}}$ = 200 GeV and run 9 (2009) minimum bias p+p data at $\sqrt{S_{NN}}$ = 200 GeV. Run 4 central trigger events are selected using ZDC east-west and BBC east-west trigger detectors, run 5 minimum bias events are selected using ZDC east-west with a vertex cut and run 9 minimum bias used ZDC east-west and the **V**ertex **P**ositioning **D**etector (**VPD**) detector. Additionally we impose a cut on the z vertex position of the reconstructed event. We reject events with a z vertex position greater than ± 25 cm from the TPC center. The TPC has a ± 100 cm full acceptance and we constrain our analysis to the quoted range in order to remove correlation artifacts due to acceptance boundary effects.

3.3.2 Event centrality

Event centrality is a classification based on the impact parameter of a heavy ion collision. Figure 2.4 summarizes the definition of using the measured charged particle multiplicity which is directly proportional to the impact parameter.

The most head-on collisions produce the highest number of tracks. As seen in figure 3.4 smaller impact parameter collisions produce higher number of tracks and corresponding events are called "central collisions". Otherwise the events are called

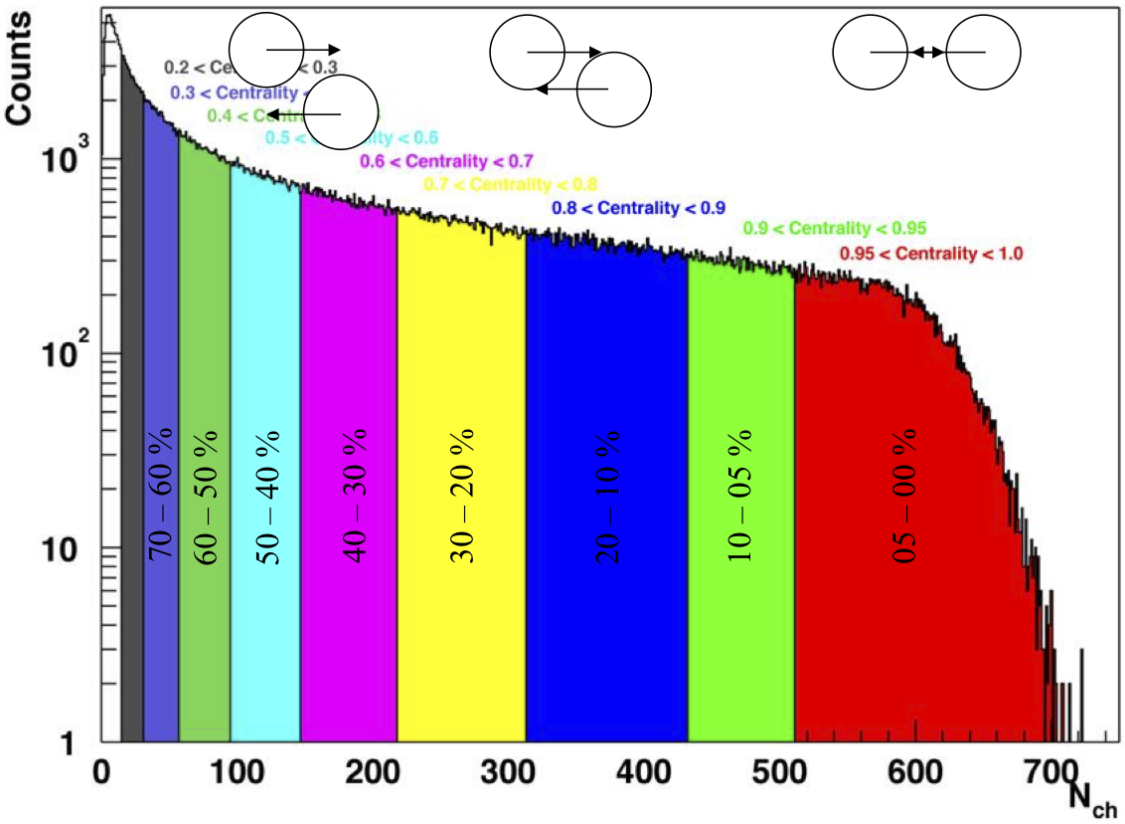

Figure 3.4: A multiplicity frequency distribution; Number of events verses the number of charged tracks produced in an event.

"mid-central" and "peripheral" collisions in the increasing order of impact parameter. In determining the multiplicity value range for a specific centrality fraction, we use a running integral method to integrate the unit normalized multiplicity frequency distribution. As an example, as seen in figure 3.4, we can determine the multiplicity bin value which selects the top 5% events with highest multiplicity out of our total minimum bias cross section and consider those events as 0 - 5% central events. Likewise we can determine any arbitrary centrality fraction percentile as depicted in the figure.

The STAR experiment uses a standard methodology in determining the centrality fractions. A reference multiplicity frequency distribution is plotted with a $|\eta| \leq 0.5$ cut on charged particle tracks. This distribution is then used to determine the centrality percentile of the events. However using the standard centrality definitions in STAR causes artificial correlation structures in our di-hadron correlation analysis which extends to $|\eta| \leq 1.0$. Thus we calculate centrality fractions with a $|\eta| \leq 1.0$ cut in order to eliminate any artificial correlation structures. It is also essential to correct for the trigger efficiencies and background estimates using Monte Carlo Glauber simulation methods [59,60].

3.3.3 Track selection cuts

Track selection cuts can be divided into three categories: kinematic cuts, particle identification cuts and reconstruction cuts. Table 3.1 states the applied track cuts in all three categories.

Figure 3.5 shows a comparison for selected track cuts, with and without the specific cut when all other cuts are applied as shown in table 3.1 [58]. The histograms are generated using 200 GeV Au+Au collisions for all centralities.

The lower p_t cut value 0.15 GeV/c is set considering the applied magnetic field strength in TPC which is 0.5 T. At this field setting, particles with lower momentum can not reach the inner field cage of the TPC since they travel in helical trajectories. The upper p_t value is set considering the fact that reconstructed tracks with even

Table 3.1: Summary of track cuts applied in the analysis

Category	Track cut	Minimum	Maximum	Description
Reconstruction	NFitPoints	15	50	Number of fit points per track
	NFitPerNMax	0.52	1.1	Track splitting correction
	χ^2	0.0	3.0	Reconstructed track quality
	Global DCA (cm)	0	3.0	Minimum distance from a reconstructed vertex to the track
Kinematic	p_t(GeV/c)	0.15	16.0	p_t range used in the minimum bias analysis
	ϕ	$-\pi$	π	Full azimuthal acceptance
	η	-1.0	1.0	Optimal η acceptance in TPC for our analysis
PID	Charge (e)	-1	1	Includes tracks with only a charge of ± 1
	NSigmaElectron	-1.5	1.5	Rejects background electrons

higher p_t are not well resolved. However we do not loose a great amount of statistics due to this kinematic cut as shown in figure 3.5.

The two angular variables we use in our analysis are the angles η and ϕ. Even though the full TPC acceptance in η stretches beyond $\pm$ 1 ($\approx \pm$ 1.25), we have to restrict our acceptance due to reduced reconstruction efficiencies in the fiducial volume of the detector. We use the full azimuth acceptance in STAR. Any fluctuations in the ϕ distribution are caused by sector boundary gaps in TPC.

There is a minimum number of fit points to a TPC track. To reduce the background contributions we set the minimum number to be 15. Also by requiring that a TPC track should have at least 52% of the estimated maximum number of fit points, we

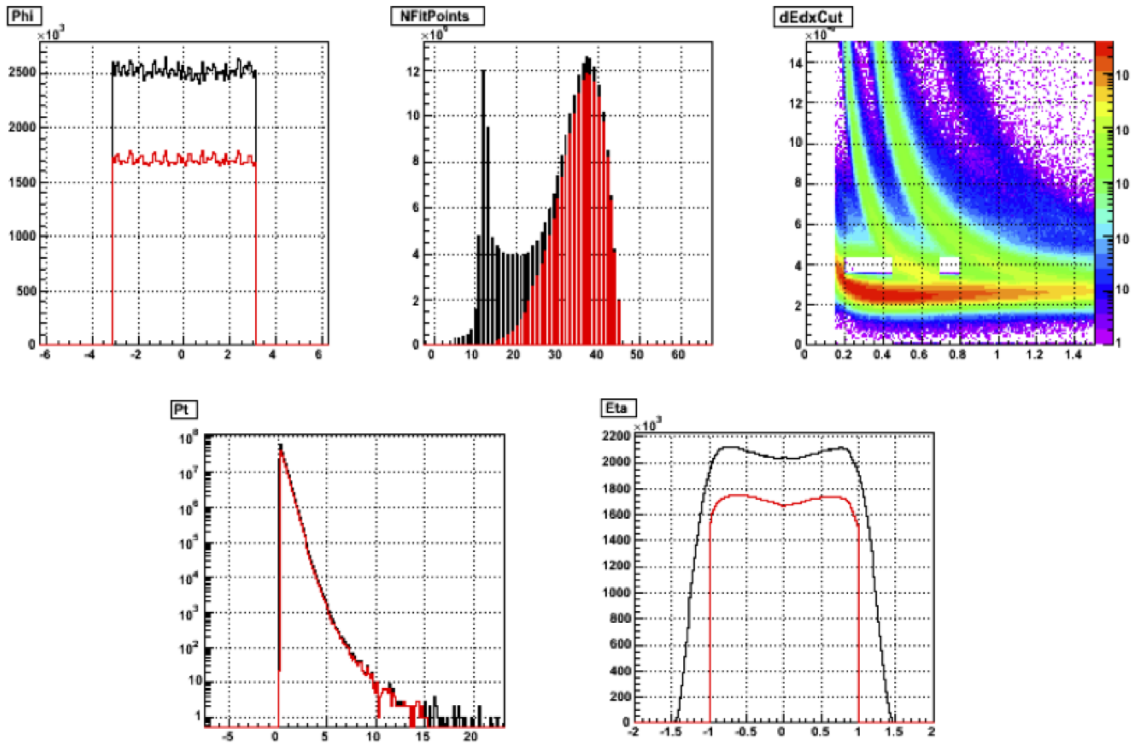

Figure 3.5: Histograms represent a comparison between with(red) and without(black) the specific cut when all other cuts are applied. Top row shows the ϕ, number of fit points and electron rejection nSigma cut's dE/dx versus momentum plot from left to right. Top row shows the p_T and η cut comparisons from left to right [58].

minimize the split track contributions. In a split track scenario, fit points from a single particle are reconstructed as two separate tracks.

In an event, the primary charged particle tracks come from the original collision vertex. However there are secondary charged particle tracks produced due to decaying parent particles as well as interaction with detector material. In order to distinguish between the two, a **D**istance of **C**losest **A**pproach (**DCA**) cut is applied. The DCA cut uses the fact that a secondary particle should not point towards the primary reconstructed event vertex. All charged particles above a DCA of 3 cm are rejected

from the analysis.

The required quality of the helix fit compared to the number of track hit points is determined by setting the acceptable χ^2 range to the fit. The chosen χ^2 value is based on previous analyses of single charged particle distributions in the TPC.

We only accept charged particle tracks with a charge of +e or -e when constructing our correlation measurement in order to reduce contributions from exotic hadron states (e.g. Δ^{++}), even though the correlation contribution due to such processes are negligible.

Finally, we reject electrons using a NSigma cut based on energy loss in TPC. The TPC energy loss is given by the Bethe-Bloch formula in equation 2.1. In figure 3.6 we can see the relevant curve for an electron in TPC. As seen in figure 3.5, by selecting the two momentum regions where the least overlap with the other dEdx curves, we apply a NSigma cut of $\pm$ 1.5 in order to identify and suppress electron contamination in the correlation measure.

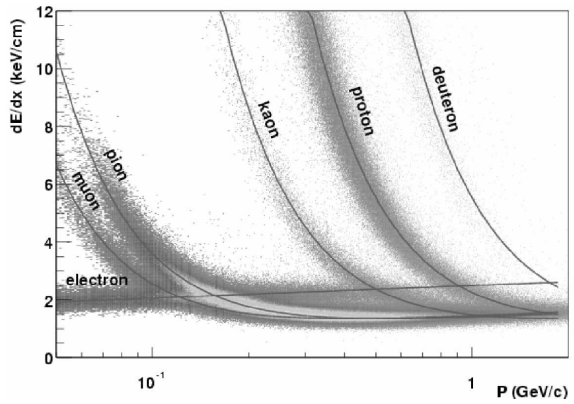

Figure 3.6: $\frac{dE}{dx}$ distributions for different species in TPC along with the corresponding predicted curves using Bethe-Bloch formula.

3.3.4 Pair loss corrections

Due to inefficiencies in track reconstruction, there is a loss in sibling pairs when compared to mixed pairs. This pair loss causes artificial correlation structures in our final correlation measure as shown in figure 3.7.

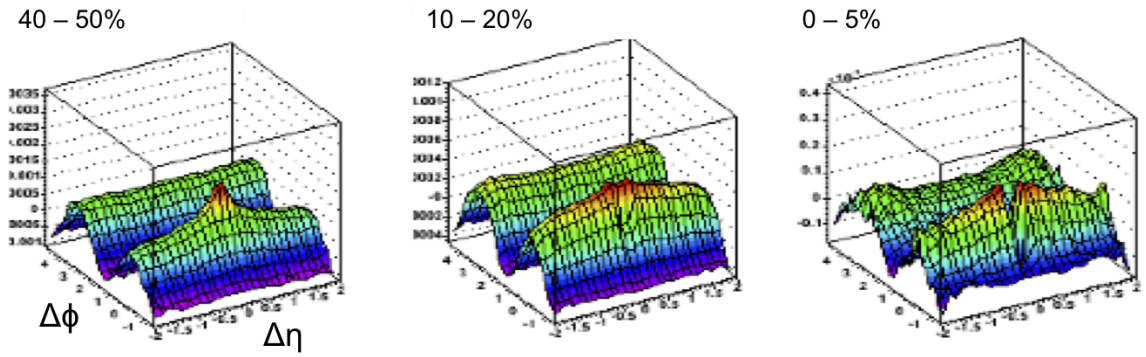

Figure 3.7: The centrality evolution of correlation structure for 0-5%, 10-20% and 40-50% (from right to left). The pair loss effect is observed in central collisions for small angle pairs [58].

The effect is pronounced in central collisions for small angle pairs. Further investigation reveal this effect is caused by track merging and track crossing [58]. In track merging, hits from two nearby charged particles are reconstructed as a single track. Under track crossing, both or one of the overlapping particles in azimuth are not reconstructed accurately.

By decoupling the η and ϕ pair loss dependence into average z (longitudinal) and x-y (transverse) separation, studies have confirmed that pair loss effects become stronger in central collisions for short range pairs [58]. Furthermore, track merging is found to be independent of the centrality whereas pair crossing is dependent on the centrality. After detailed studies, a pair cut based on the average transverse and longitudinal

separations has been devised [58]. Pairs are rejected from both sibling and mixed pairs in order to avoid over-correction. It has been found that, for the track merging correction, an average transverse and longitudinal separation of less than 5 cm is an appropriate cut. For the pair crossing correction, it required a less than 5 cm cut on longitudinal separation and a less than 15 cm cut on transverse separation. Pairs below the cut values have been rejected for the run 2 Au+Au 200 GeV angular correlation data [58]. We adopted the same cut scheme and optimized the cut values to avoid loss of statistics. For the pair crossing correction, our analysis required only a less than 5 cm cut on transverse separation. The rest of the cut values did not change from the previous studies.

3.3.5 Tracking efficiency

In order to draw precise physics conclusions, we need to correct the particle information for acceptance issues and detector inefficiencies. In order to achieve this, in principle, a differential study needs to be carried out as a function of p_T, η and ϕ. The issues can be categorized mainly into two; the tracks which do and do not pass through the active detector volume. In order to cancel out the inefficiency and acceptance issues originating from the tracks which pass the active detector material, we adopt the technique which we discussed under section 3.2.3. However, this technique (dividing the sibling pair signal by the mixed pair signal) does not correct for the inefficiencies and acceptance loss caused by the tracks which do not pass through the active detector volume. Generally a Monte Carlo simulation study is carried

out in order to calculate the efficiency factor to correct raw data. In our analysis, this efficiency correction factor needs to be applied in the pre-factor $\sqrt{\rho'}$ (equation 3.19). Figure 3.8 shows the tracking efficiency as a function of η and p_T from a previous study in the STAR experiment [STAR thesis: Mark Horner, University of Cape Town]. The same procedure needs to be carried out under our kinematic cut scheme in order to get the relevant tracking efficiencies. Our current results do not reflect this efficiency corrections and will be carried out during the publication stage.

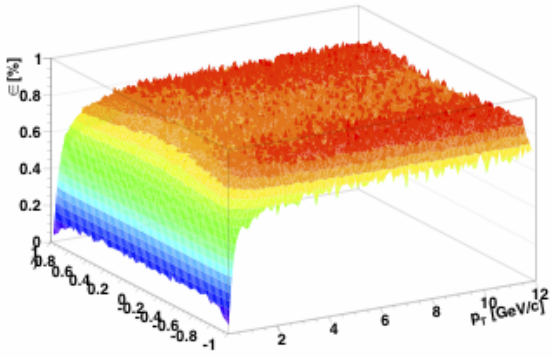

Figure 3.8: The tracking efficiency as a function of p_T and η for 0-5% Au + Au data [Mark Honer].

Chapter 4

A fit model for complex di-hadron correlations

If a stationery isotropic homogeneous system is created in a heavy ion collision, then we could expect a flat correlation structure in our di-hadron correlations (see figure 4.1) since all particles emitted from the source have an equal probability to be emitted in any direction.

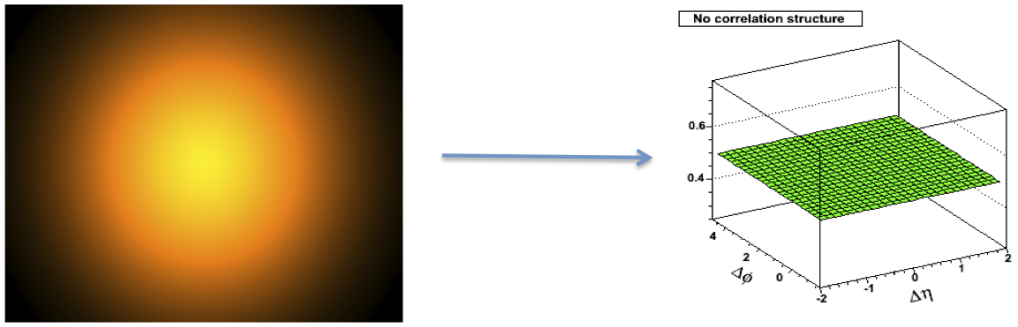

Figure 4.1: Left: A stationery isotropic homogeneous system. Right: Corresponding correlation structure in $\Delta\eta - \Delta\phi$.

However, in high energy nuclear physics we expect certain correlation structures due to well known physical processes. In this chapter we discuss such processes and develop an empirical fit model to extract the underlying physical phenomena.

4.1 Parton fragmentation

Figure 4.2 left-hand side illustrates a back to back hard scattering and the resulting fragmentation of both partons in p + p collisions while the right-hand side shows the corresponding di-hadron correlation on near and away side.

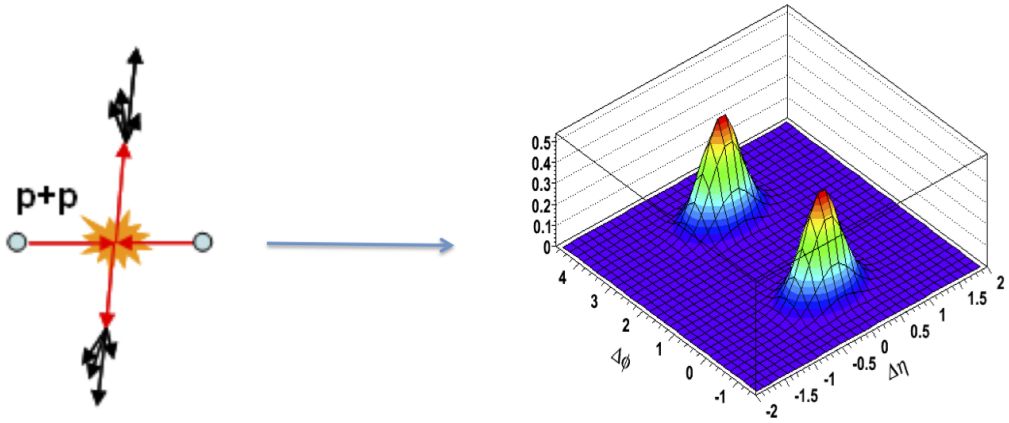

Figure 4.2: Left: Back to back parton hard scattering in p + p collisions. Right: The corresponding near and away side correlation structure in $\Delta\eta - \Delta\phi$ space.

These hard parton scatterings are expected to occur in elementary as well as heavy ion collisions. In heavy ion collisions only the non-thermalized high momentum fraction of the fragmentation process should be visible above the bulk particle contribution. Therefore we include an asymmetric 2d Gaussian model component in our fit model which has the following mathematical form:

$$a_3 exp\left\{-\frac{1}{2}\left[\left(\frac{\Delta\eta}{a_4}\right)^2+\left(\frac{\Delta\phi}{a_5}\right)^2\right]\right\} \tag{4.1}$$

where a_3 is the amplitude, a_4 is the $\Delta\eta$ width and a_5 is the $\Delta\phi$ width. Although the jet peaks are measured to be symmetric in $\Delta\eta$ and $\Delta\phi$ in elementary collisions, we leave both widths as free parameters in order to accommodate any jet medium modification in heavy ion collisions.

4.2 Away-side momentum conservation

As we have discussed before, with the near side trigger parton there is a back to back recoil associated partner which is ideally 180° opposite in azimuth. Since in p + p collisions we do not experience a medium formation at these energies ($\sqrt{S_{NN}} = 200\,GeV$), this associated parton on the away-side fragments in a similar way to the trigger thus requiring a 2d Gaussian to model the correlation structure on the away side as well (figure 4.2).

In heavy ion collisions, the associated particle on the away-side might undergo enhanced medium interactions due to the surface bias of the same side trigger particle. In azimuthal correlations, studies have shown an enhanced yield with a broader away-side (compared to the near side width) peak for low momentum particles and a relatively strong depleted yield for the high p_T particles [19]. As we discussed under section 1.4, this indicates that our recoil jet interacts with a medium, looses energy

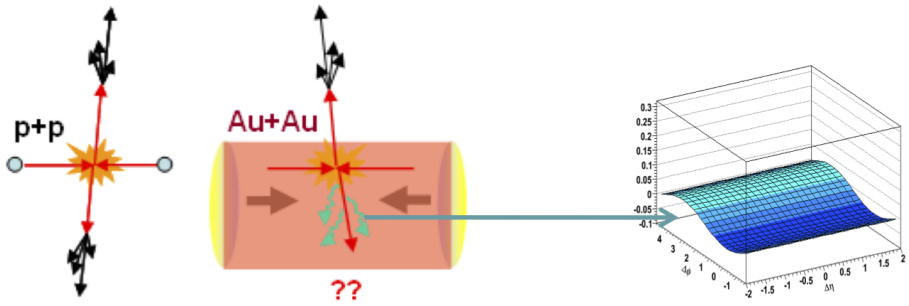

Figure 4.3: A schematic of hard parton scattering in p + p(left) and Au + Au(center) collisions. In p + p the associated partner does not traverse a medium whereas in Au + Au it does. The corresponding correlation structure is shown on right.

and looses its initial scatter direction in ϕ. Following the same reasoning in η direction, we could model the away-side momentum conservation term using a -cos($\Delta\phi$) model component in the fit as shown in figure 4.3. This term models both global and local momentum conservation phenomena in such collisions.

4.3 Elliptic flow

Figure 4.4 shows a schematic of the elliptic flow phenomenon. After a non-central heavy ion collision, the interaction zone can be described by an almond shape. If the system behaves collectively, this initial coordinate space anisotropy is converted into a momentum space anisotropy for all measured final state charged hadrons. In a Fourier expansion of the angular distribution the second harmonic component (v_2) directly relates to the elliptic shape of the initial system's coordinate space geometry and was discussed as a key signature for the existence of a QGP [61]. In a pair correlation measure this phenomena is expected to give a cos($2\Delta\phi$) structure, thus

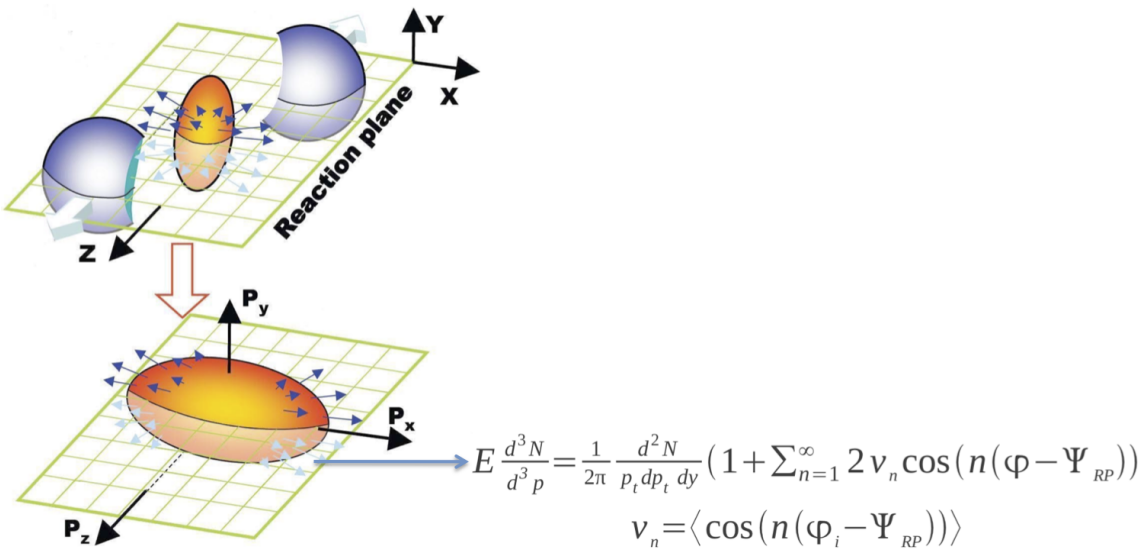

Figure 4.4: Left top: A mid-central heavy ion collision in coordinate space has an almond shape. Left bottom: The initial coordinate space anisotrpy is converted in to a momentum space anisotropy due to the collective nature of the medium. Right: The momentum space anisotropy can be Fourier decomposed.

we include the corresponding model component. It is also important to note at this point that a first term in a Fourier expansion of the angular distribution, known as dipolar asymmetry [62 - 68], would have the same term as the above mentioned away-side momentum conservation [163] component. We have not made any attempts to separate the momentum conservation and dipolar asymmetry correlation phenomena from the extracted -cos($\Delta\phi$) model component.

4.4 Higher order harmonics

The importance of higher order terms in the Fourier decomposition of an anisotropic angular distribution shown in figure 4.4 has been discussed in recent theoretical

publications [71,72,73]. Figure 4.5 shows a schematic which describes the underlying physical origin of higher order

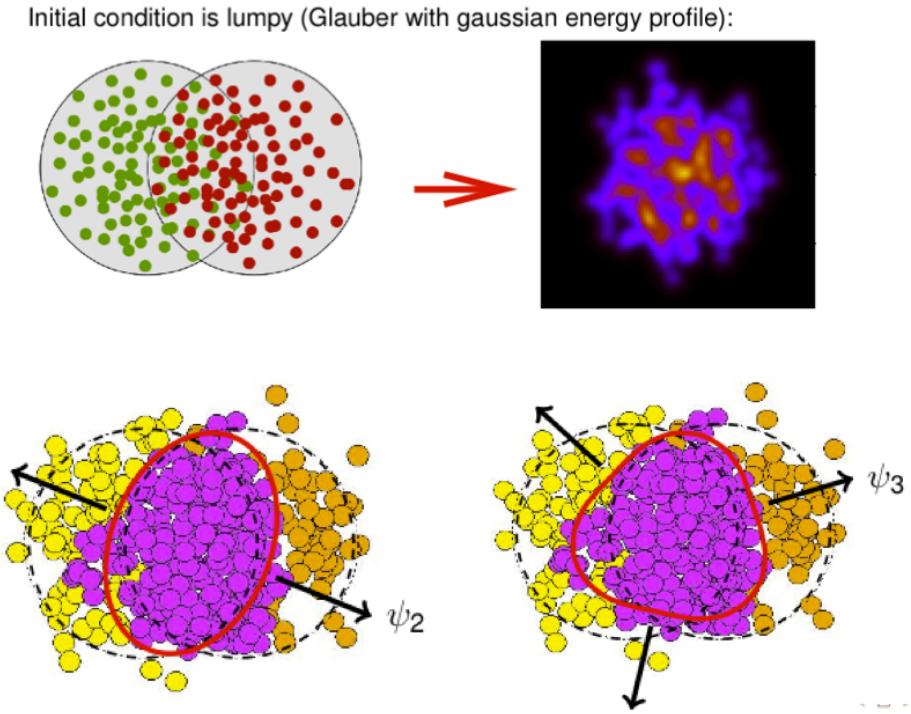

Figure 4.5: Top: Shows the initial nucleon and the corresponding energy distribution from a heavy ion collision. Bottom: Shows possible initial nucleon distributions which generates higher harmonics flow (from M. Luzum QM 2011).

harmonics. It follows the same reasoning as with elliptic flow, the 2nd harmonic in the azimuthal decomposition, but is more sensitive to the fluctuations in the initial energy density distribution. In other words, rather than using hard sphere nuclei in a Glauber calculation, any realistic nucleon distribution assuming, for example, a Woods-Saxon potential for the nuclear surface will lead to energy density fluctuations beyond the simple almond shape. Figure 4.5 bottom shows as an example the third-order harmonic deduced from the same initial nucleon distribution than v_2. The series

can be expanded to include all harmonics up to the order which can be assigned to the measured correlation function with some significance. The higher order fluctuations are predicted to become even more important in very central collisions when the 2nd Fourier coefficient is negligible. Figure 4.6 shows the harmonics (n = 1-6) as a function of p_T from an AMPT model calculation [71]. In our p_T evolution study we will search for this evidence (section 5.2) and incorporate model components ($\cos(n\Delta\phi)$; n > 2) to extract correlation contributions to the data.

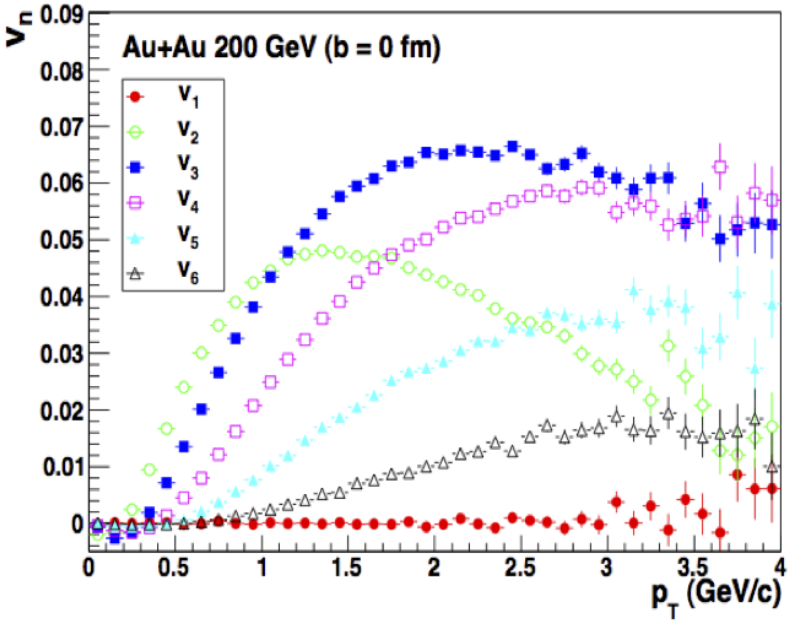

Figure 4.6: Azimuthal anisotropies of hadron spectra $v_n(p_T)$ (n = 1-6) in central (b = 0) Au+A collisions at $\sqrt{S_{NN}} = 200$ GeV from AMPT model calculation [71].

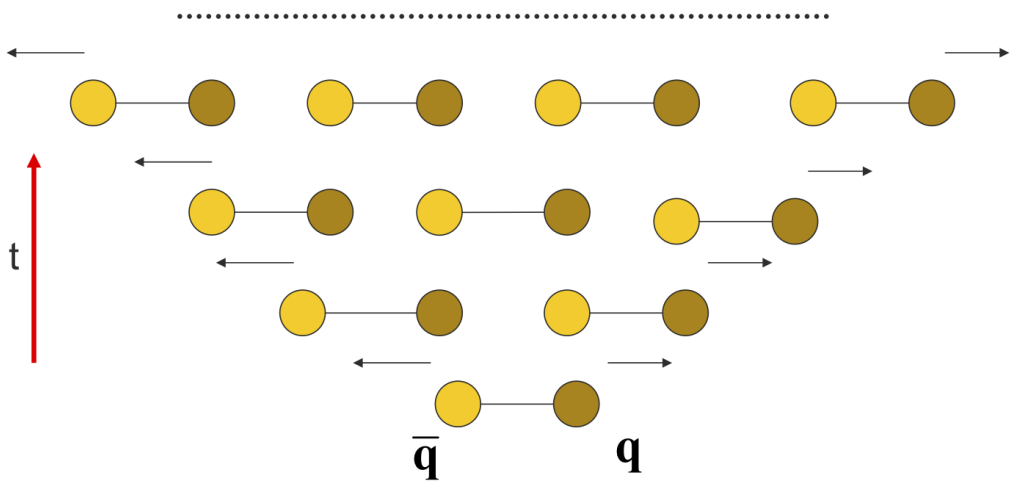

Figure 4.7: Time evolution of the Lund string fragmentation phenomena [69].

4.5 String fragmentation

String fragmentation phenomena can be understood simply using the Lund model, which is also applied in the PYTHIA event generator [162]. As we saw in figure 1.4, pulling apart a color neutral $q\bar{q}$ pair creates a color force between the two quarks. The color force lines are constrained in a narrow tube connecting the two with a string tension of ≈ 1 GeV/fm. In a collision, partons with low momentum are expected to form such $q\bar{q}$ pairs which undergo oscillations due to string tension and the resulting fragmentation occurs as shown in figure 4.7. In the $q\bar{q}$ rest frame, these fragments are moving along the longitudinal direction with the possibility of arbitrary azimuthal orientation. This motion is expected to generate a structure which is flat in $\Delta\phi$ and having a narrow width in $\Delta\eta$ as shown in figure 4.8.

Therefore we include a 1d Gaussian model component in $\Delta\eta$ which has the following form:

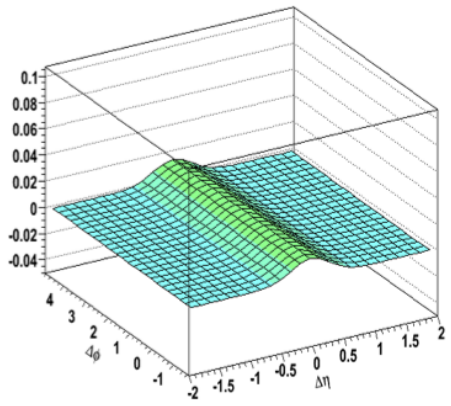

Figure 4.8: The 1d Gaussian structure in $\Delta\eta$ that represents Lund string fragmentation.

$$a_6 exp\left[-\frac{1}{2}\left(\frac{\Delta\eta}{a_7}\right)^2\right] \tag{4.2}$$

where a_6 and a_7 are the amplitude and width of the 1d Gaussian, respectively. It is also important to mention that the correlation contribution due to this phenomena becomes negligible in central (0-10%) Au + Au collisions.

4.6 Hanbury Brown Twiss (HBT) effect, $\gamma \rightarrow e^+e^-$ and resonances

The contribution to heavy ion physics from the well known HBT phenomena can be found in [70]. In essence, quantum interference effects between detected identical particles with similar relative momentum give rise to small angle correlations in our correlation function thus leads to a narrow peak around $\Delta\eta$, $\Delta\phi = 0$.

A similar structure can be expected from resonance decay. Resonances are excited

states of ground state hadrons which decay via strong decay. Since the strong decay is allowed (i.e. conserves all quantum numbers) the lifetime of hadronic resonances is comparable to the lifetime of the plasma (on the fm/c scale). Typical examples of hadronic resonances and their decays are the; $\Delta \to \rho\pi$, $k^* \to k\pi$, $\phi \to k^+k^-$ and $\rho \to \pi^+\pi^-$. A resonance decay is a decay of a parent particle into daughter particles (e.g. $\Lambda \to \pi^- p$). At the decay vertex (figure 4.9) the daughter particles are close to each other in coordinate space. Therefore in the final state charge particle correlation structure, resonances also produce small angle correlations. Finally, gamma conversions in the detector material ($\gamma \to e^+e^-$) also generate small angle correlations. All of these contributions are modeled using a 2d exponential model component centered around $\Delta\eta$, $\Delta\phi = 0$ which has the following form:

$$a_8\, exp\left\{-1\left[\left(\frac{\Delta\eta}{a_9}\right)^2 + \left(\frac{\Delta\phi}{a_{10}}\right)^2\right]^{1/2}\right\} \tag{4.3}$$

where a_8, a_9 and a_{10} are the amplitude, $\Delta\eta$ width and $\Delta\phi$ with of the 2d exponent respectively. It is also important to mention that all three contributions are low momentum phenomena.

4.7 Fit model and procedure

Based on the information in this chapter, the most generic fit function that should be applied to the data consists of the following components.

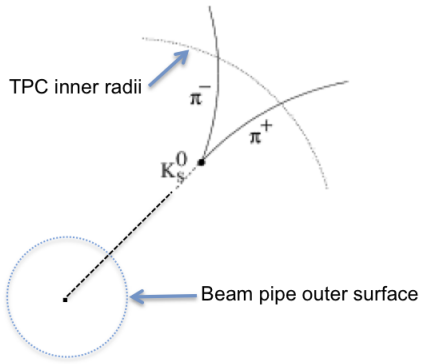

Figure 4.9: The decay of a K^0_S into a $\pi^+\pi^-$ pair.

$$F = a_0 + a_1 cos(\Delta\phi) + a_2 cos(2\Delta\phi) + a_3 cos(3\Delta\phi) + a_4 cos(4\Delta\phi) + a_5 cos(5\Delta\phi) + a_6 exp\left\{-\frac{1}{2}\left[\left(\frac{\Delta\eta}{a_7}\right)^2 + \left(\frac{\Delta\phi}{a_8}\right)^2\right]\right\} \quad (4.4)$$

Our approach to investigate novel di-hadron correlations takes two paths. First we carried out a centrality evolution study to cross check our analysis with the previous study [58] and to provide with an important comparison between Cu + Cu and Au + Au collisions at 200 GeV. Then we focused on a $\langle p_T \rangle$ evolution of di-hadron correlation in 0-10% centrality using both Cu + Cu and Au + Au collisions at 200 GeV.

In either fit procedure we do not always require all model components described in this chapter since some components are p_T and centrality dependent. We instead select the required model components based on the requirements from the data and report our findings. We also carried out additional fit quality tests as described in previous studies [58] and confirmed the global minimum status of our resulting fit. Some of the tests we carried out are, changing fit parameter range, alternative fitting

procedures, random initial parameters and χ^2/DOF as a function of fit parameter value (see figure 4.10).

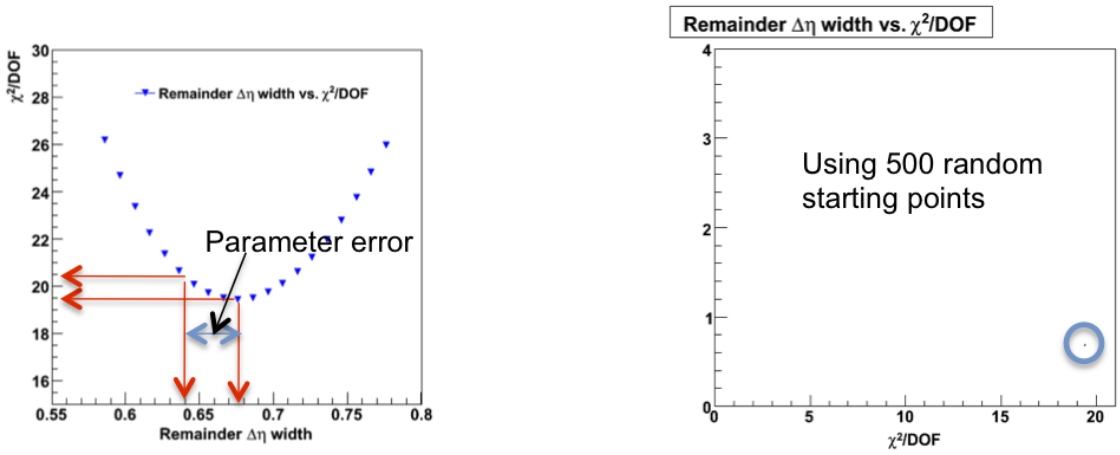

Figure 4.10: Left: The χ^2/DOF distribution as a function of the corresponding parameter value ("remainder" $\Delta\eta$ width). The corresponding change in the parameter value to a change in χ^2/DOF at the minima by one unit is quoted as the parameter error. Right: Result from using 500 random starting fits. None of the fits converge to an improved χ^2/DOF value with a different $\Delta\eta$ width.

The left panel in figure 4.10 describes the χ^2/DOF distribution as a function of the "remainder" $\Delta\eta$ width. At the minimum χ^2/DOF value (19.4 for this $\langle p_T \rangle$ bin), the corresponding $\Delta\eta$ width converge to 0.6764. We produce the χ^2/DOF distribution by changing the $\Delta\eta$ width from its fit minima value in order to cross check the possibility of a second minima which better describes the data. This test was carried out for all other parameters in the model and found that fits converge to the global minima. We further carried out a random input fit test to convince our selfs in the global minima we obtained. The result from 500 random input fits is shown on the right panel in figure 4.10. Each random input fit was iterated 5 times before the final converging fit was decided. The results confirm that previously quoted global

minima does not change with different combinations of input fits and indeed we are reporting the global minima fit parameters.

The errors we report in this thesis are primarily due to statistics. When calculating the fit parameter errors, statistical error distributions in data as well as minimization uncertainties are taken in to account by the standard ROOT minimization algorithm MINUIT (χ^2 minimization)[74]. The error on raw data histograms are propagated in quadrature (the standard method) at each manipulation (scaling, dividing, etc.). However when reporting the final fit parameter error, we avoid reporting the MINUIT procedure and used the method depicted in figure 4.10 left panel. This method takes into account cross correlations between model parameters and quote change in parameter value based on $\chi^2/DOF_{minima} + 1$ as the parameter error. This is essentially different to the standard statistical practice, where $\chi^2_{minima} + 1$ is used (MINUIT). We argue that our method practically suits when fitting 2d histograms since $\chi^2/DOF_{minima} + 1$ shows a considerable change in the residual structure as compared to the standard practice. Possible sources of systematic error are non-primary track contamination, event vertex position dependences, photon conversions ($\gamma \rightarrow e^+e^-$) due to detector material and two track inefficiencies [75]. Additional information on fit quality will be discussed in detail at relevant places in chapter five along with the fit results.

Chapter 5

Results

As mentioned under section 1.4, our principal motivation behind the interpretation of heavy ion data is to find evidence for the existence of a QGP and related phenomena. Our contribution will be to understand the novel correlation phenomena observed in STAR di-hadron measurements as described under section 1.4.4. We discuss the implications of our study regarding QGP formation and QGP properties in chapter six. In this chapter, we first describe previous measurements of di-hadron correlations before showing the results from our analysis, which we devised by taking the previous studies into consideration [22,76,77].

5.1 Previous studies of di-hadron correlation function

An enhanced correlated yield on the near side ($\Delta\phi \approx 0$) at large pseudo rapidity separations ($\Delta\eta$) has been observed in previous di-hadron correlation studies [22,76,77]. The correlation structure corresponding to this yield, which is also known as the ridge, was first observed in [22] for all charged particle pairs in the low p_t ($p_t < 2$ GeV/c) regime and also in [76] for trigger particles in the intermediate p_t ($4 < p_t < 6$ GeV/c) range. Since it was unclear from those measurements whether the novel structure is related to hard parton scattering followed by jet production, further investigations were carried out in [77] pushing the trigger p_t up to 9 GeV/c. It is observed that the novel correlation exists up to the highest possible trigger p_t within the given statistical reach.

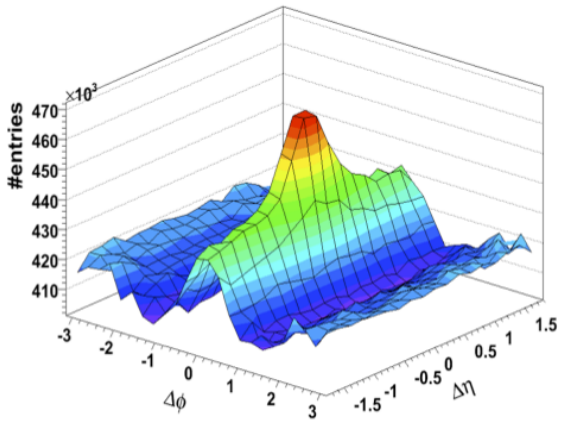

Figure 5.1: Raw $\Delta\phi$ x $\Delta\eta$ di-hadron correlation function in central Au + Au collisions for $3 < p_T^{trig} < 4$GeV/c and $p_T^{assoc} > 2$GeV/c. (Background and flow subtracted).

Figure 5.1 displays the main result, namely a near side yield that exhibits a

distinguishable peak around ($\Delta\eta$,$\Delta\phi$) = (0, 0). This is expected from jet fragmentation. The other prominent structure is the ridge structure where the enhancement of correlated yield at large $\Delta\eta$ on the same side is clearly visible. Assuming distinct underlying physical processes in the different $\Delta\eta$ regions, the near side is decomposed into a jet like peak and a $\Delta\eta$ independent ridge component. By projecting the two dimensional correlation function on to $\Delta\eta$ and $\Delta\phi$ in different $\Delta\phi$ x $\Delta\eta$ regions, the information from the di-hadron measurements related to the ridge were extracted. The two decompositions are symbolized as J and R. The small $\Delta\eta$ jet-like yield is symbolized as J and the large $\Delta\eta$ ridge-like yield is symbolized as R. Three projections were studied.

- $\Delta\phi$(J + R): Projecting onto $\Delta\phi$ with the full experimental $\Delta\eta$ acceptance, $|\Delta\eta| < 1.7$, and subtracting the elliptic flow modulated (v_2) background.
- $\Delta\phi$(J): Subtracting the $\Delta\phi$ projection for $0.7 < |\Delta\eta| < 1.7$ from the $\Delta\phi$ projection $|\leq|$ 0.7.
- $\Delta\eta$(J): Projecting onto $\Delta\eta$ in a $\Delta\phi$ window $|\Delta\phi| < 0.7$. A constant fit to the measurements was used to subtract the background.

The following one-dimensional schematic (fig. 5.2) further illustrates the idea.

Figure 5.3 shows the same side yield as a function of the number of participants N_{part} in the collision. The assumption of the uniformity of the ridge-like correlation structure in $\Delta\eta$ acceptance is confirmed by the agreement of the measured jet-like yield between the $\Delta\eta$(J) and $\Delta\phi$(J) method for all centralities. The jet-like correlated

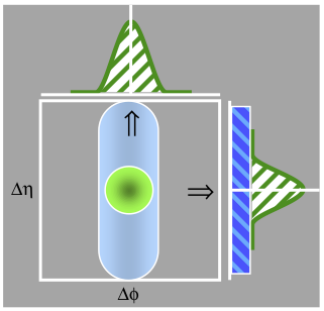

Figure 5.2: One-dimensional view of ridge + jet yield.

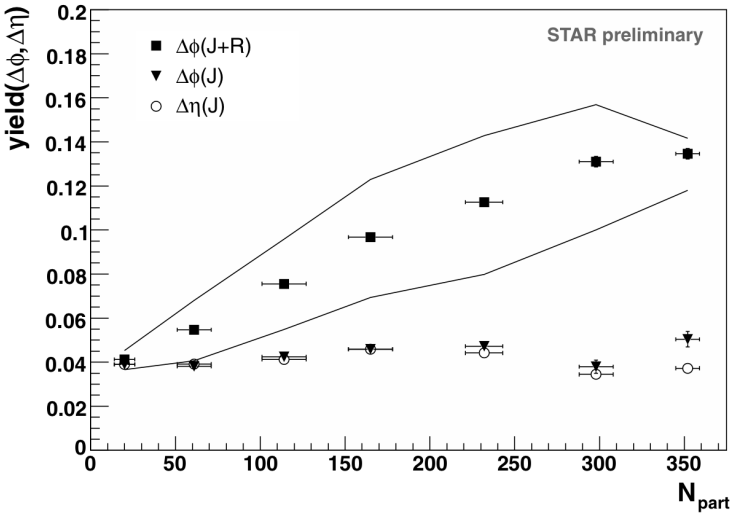

Figure 5.3: Near-side yield of associated particles in $\Delta\eta$ and $\Delta\phi$ with $p_t^{assoc} > 2$ GeV as a function of N_{part} in Au+Au for $3 < p_{trig} < 4$ GeV.

yield is independent of centrality (N_{part}) and agrees with the p + p yield [63]. Due to the inclusion of the correlated yield at large $\Delta\eta$ the $\Delta\phi$(J + R) yield shows a significant increase with centrality.

The absolute ridge is defined as the difference in the yields $\Delta\phi$(J + R) and $\Delta\eta$(J). Figure 5.4 shows the substantial persistence of ridge yield up to the highest p_T^{trig}. Thus the ridge can be associated with jet production. It is also shown that the

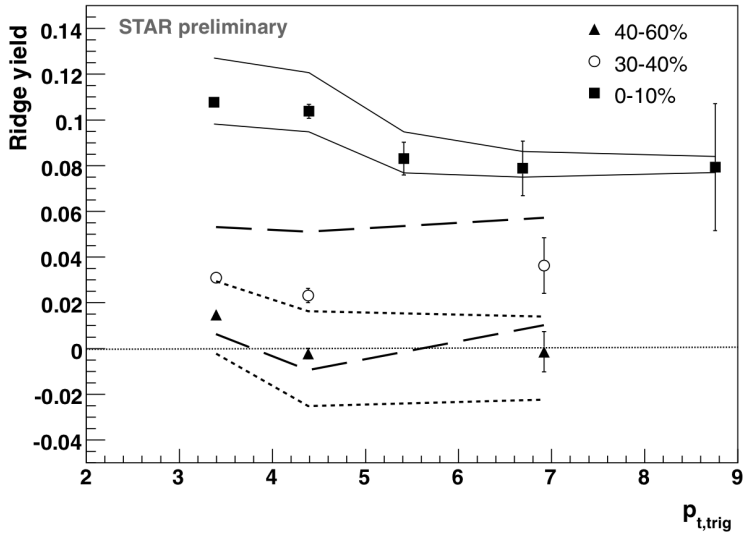

Figure 5.4: Absolute ridge yield for different centralities as a function of p_T^{trig} for $p_T^{assoc} > 2$ GeV/c in Au + Au.

ridge yield increases with centrality. Various other approaches were taken in [77] to study the properties of the particles associated to the ridge-like or jet-like same side correlation. The study of the ridge yield via p_T^{assoc} spectrum in different p_T^{trig} windows and the study of the near side di-hadron fragmentation function in central Au + Au collisions further strengthens the assumption that the same side $\Delta\phi$ x $\Delta\eta$ correlation consists of two distinct components: a jet contribution, consistent with the p + p and d + Au di-hadron reference measurements [78], and the ridge contribution with properties similar to the medium.

5.2 Analysis approach for dissertation study

In order to investigate the cause of the ridge structure, we focus on the correlation structure in the most central events (0-10%). Firstly, this centrality bin corresponds to the highest possible energy density created in a heavy ion collision for a given system (Au + Au or Cu + Cu). Secondly, if a QGP is formed, it is likely to be formed in the highest possible energy density environment and we can study the relation between the novel correlation phenomena and QGP. Finally, considering the centrality trend observed in raw data (fig. 5.5 and fig. 5.6), we expect the novel correlation strength to be the strongest at 0-10% centrality bin. We also carefully studied the transverse momentum ranges that were explored in the previous studies [22,76,77] and decided to add more detail to this parameter dependence. In our study the transverse momentum evolution of di-hadron correlations is obtained by raising the lower p_T acceptance for both charged particles using the untriggered analysis technique. We first report our initial comparison studies of the Cu + Cu and Au + Au centrality dependence, and then discuss our findings from the p_T evolution study using Cu + Cu, Au + Au and p + p collisions.

5.3 Centrality evolution studies

As we discussed under section 3.2, our di-hadron correlation analysis technique uses all charged particle pairs ('untriggered analysis') as opposed to the above (section 5.1) discussed triggered analysis. From our centrality evolution study (fig. 5.5 and

fig. 5.6) it is evident that the ridge structure starts to appear with increasing centrality in heavy ion collisions. This observation provides an independent confirmation of the previous triggered studies that have been carried out [22,76,77]. Di-hadron correlations in peripheral heavy ion collisions are expected to show a similar structure that in elementary collisions, which is confirmed by comparing inclusive p + p collisions to peripheral Cu + Cu and Au + Au collisions (fig. 5.7). However even in the most peripheral 70-80% bin, we still observe a slight relative $\Delta\eta$ elongation in the Au+Au 200 GeV system. This observation is directly related to the density of the system created in the collision.

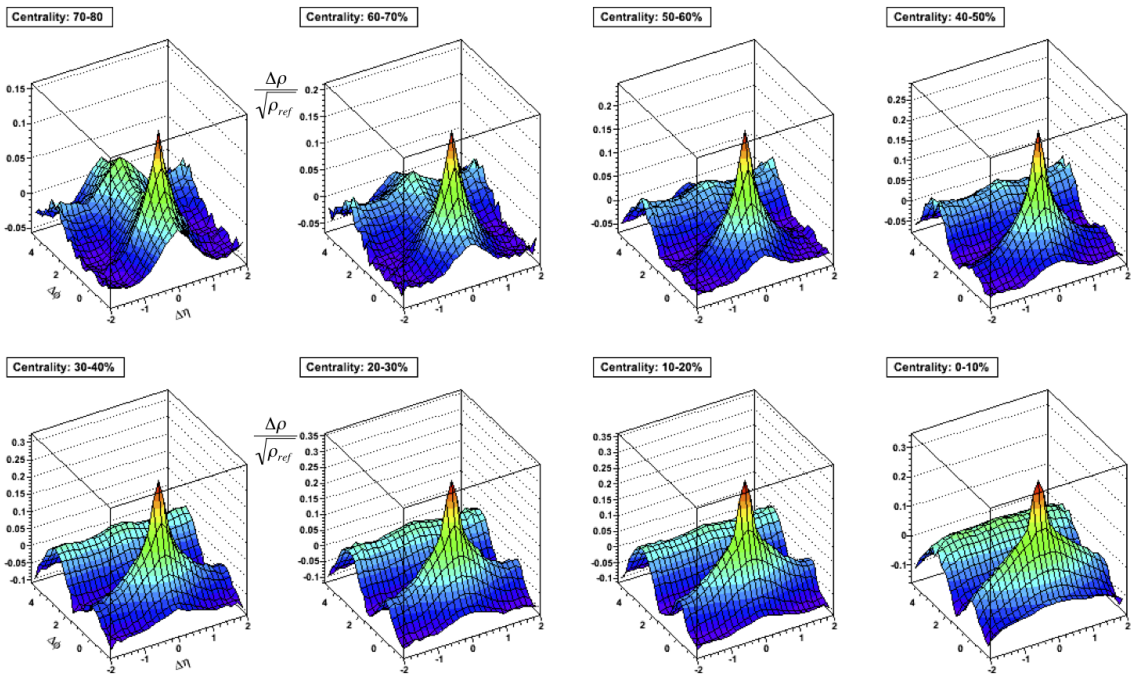

Figure 5.5: Centrality evolution of di-hadron correlation in Cu + Cu collisions at $\sqrt{S_{NN}} = 200$ GeV.

It is also important to note how the away side correlation structures compare. The

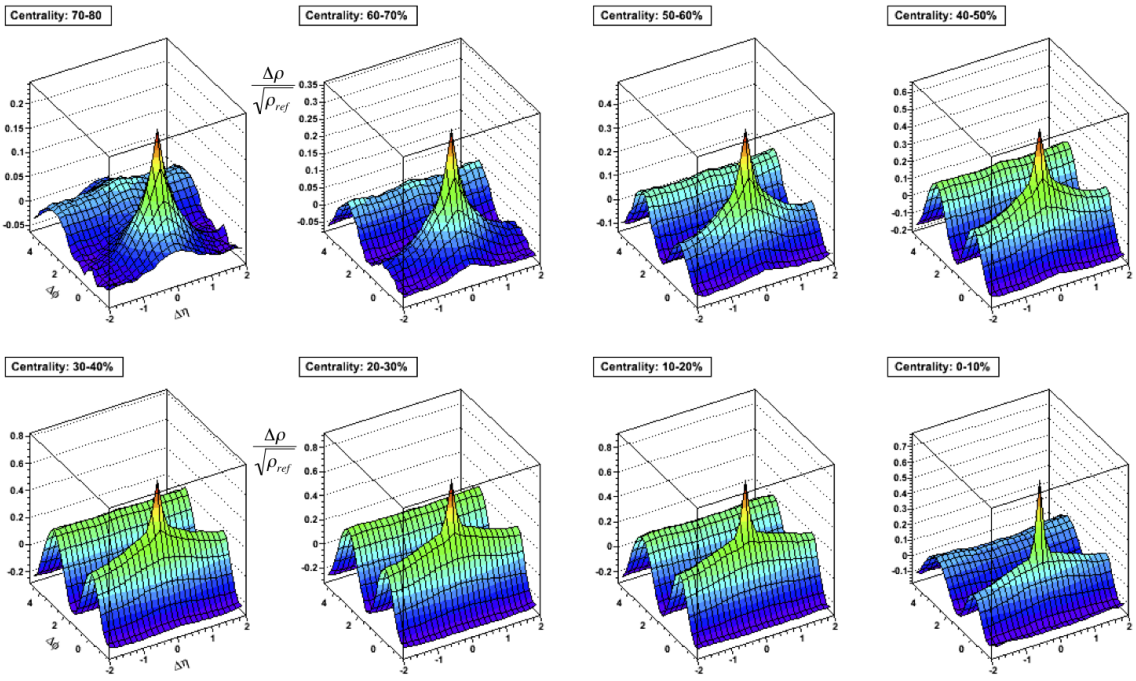

Figure 5.6: Centrality evolution of di-hadron correlation in Au + Au collisions at $\sqrt{S_{NN}} = 200$ GeV.

comparisons are well explained using jet-like correlation processes (see sections 1.4.4, 4.1 and 4.2). In elementary collisions (p+p) the recoil partner from a hard scattering has no medium to interact with. Thus on average the recoil partner does not have a broadened pseudo rapidity compared to, for example, PYTHIA simulations. In the case of medium formation, the recoil partner interacts with the medium and thus has a higher probability to scatter away from the original pseudo-rapidity direction (see fig. 5.7).

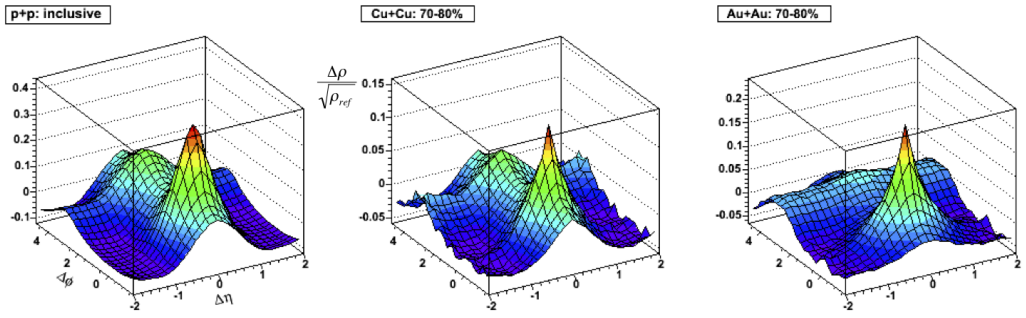

Figure 5.7: Comparison of di-hadron correlation structures between elementary collisions and peripheral heavy ion collisions

The underlying assumption which is studied in a centrality evolution study is whether Au + Au collisions can be understood as a linear super position of elementary p + p collisions. If Au + Au collisions were a linear superposition of p + p collisions, the correlation measure would be independent of the centrality. A geometrical centrality measure is defined as $\nu \equiv \frac{\langle N_{bin}\rangle}{\langle N_{part}\rangle/2}$ [58] where $\langle N_{part}\rangle$ is the average number of participating nucleons in a collision and $\langle N_{bin}\rangle$ is the average number of binary (nucleon-nucleon) collisions in an event. The ν values corresponding to the standard STAR centrality percentiles have been calculated for Cu + Cu and Au +

Au collisions at selected center of mass energies using a Glauber Monte Carlo simulation study [79]. In our centrality evolution study we make use of this representation. In order to determine the underlying physics origins of this correlation structure, an empirical model fit function based on model components discussed in chapter four has been adopted. The centrality evolution of the model component parameters are studied in order to test the linear superposition hypothesis.

Contribution in p + p correlations

The charge independent di-hadron correlation structure in p + p 200 GeV has been decomposed into two p_T ranges in figure 5.8. This decomposition lead to identify three specific correlation contributions that were discussed in chapter four. The Lund string model (longitudinal fragmentation) explains the correlation structure centered along $\Delta\eta = 0$ for the low momentum particle pairs.

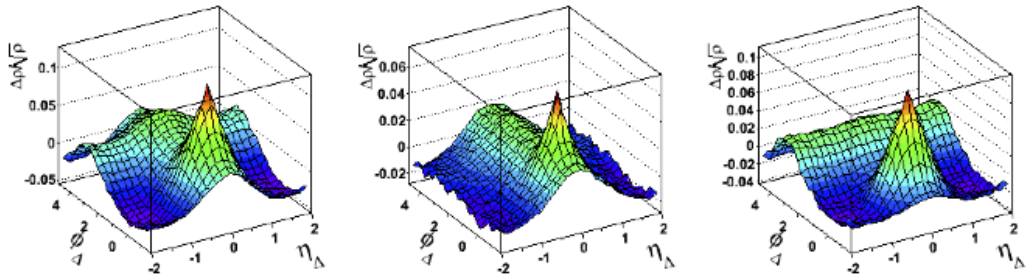

Figure 5.8: Charge independent di-hadron correlation structure for all charged pairs(left), low momentum(p_T < 0.5 GeV/c) pairs(middle) and intermediate momentum(p_T > 0.5 GeV/c) pairs(right) in p + p 200 GeV collisions [58].

Secondly, for the large peak observed at the origin ($\Delta\eta$=0,$\Delta\phi$=0), we have several contributing processes. **H**anbury **B**rown and **T**wiss (**HBT**) quantum interference and resonance studies suggests a sharp 2d exponential peak at the origin for the low

momentum pairs [81]. For intermediate momentum pairs, mini-jet/jet fragmentation processes are the main sources of correlation which can be modeled using a 2d Gaussian. Possible electron-positron contamination in this narrow region about the origin has been suppressed via the dE/dx cut we described in table 3.1. The third and final correlation structure is the away side ridge along $\Delta\phi = \pi$. This structure originates due to momentum conservation in intermediate momentum scattering processes and global momentum conservation. The structure can be represented via a -cos($\Delta\phi$) function.

Contribution in heavy ion collisions

Additionally, in heavy ion collisions we require a cos($2\Delta\phi$) component to represent elliptic flow correlations [82]. Since the primary motivation behind the centrality evolution study was to compare our results to the previous Au + Au study [58], we did not include higher order harmonics in the fit model. After considering possible correlation contributions, the empirical model function takes the following form. The corresponding 11 fit parameters are denoted by $a_i\,(i = 0, 1, ..., 10)$ which are described in table 5.1.

$$F = a_0 + a_1\,cos(\Delta\phi) + a_2\,cos(2\Delta\phi) + a_3\,exp\left\{-\frac{1}{2}\left[\left(\frac{\Delta\eta}{a_4}\right)^2 + \left(\frac{\Delta\phi}{a_5}\right)^2\right]\right\}$$
$$+\ a_6\,exp\left[-\frac{1}{2}\left(\frac{\Delta\eta}{a_7}\right)^2\right] + a_8\,exp\left\{-1\left[\left(\frac{\Delta\eta}{a_9}\right)^2 + \left(\frac{\Delta\phi}{a_{10}}\right)^2\right]^{1/2}\right\} \qquad (5.1)$$

Figure 5.9 above shows an example fit decomposition for mid central Cu + Cu

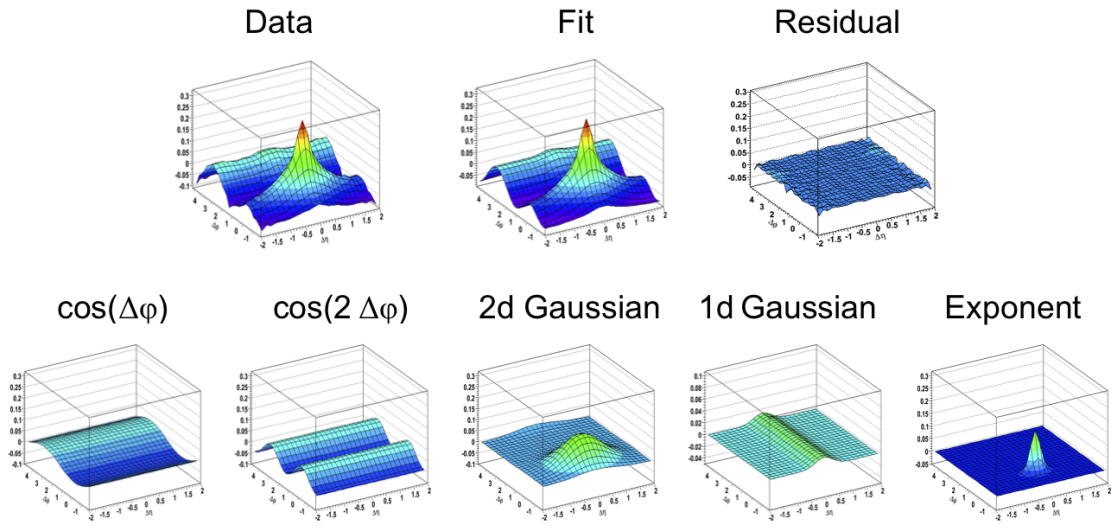

Figure 5.9: An example fit from Cu + Cu 200 GeV data at 30-40% centrality bin. Top row shows the fit quality graphically and the bottom row shows the model decompositions.

200 GeV data. The residual structure (data - fit) is a proof for the good χ^2/DOF value (≈ 3.24) we get from our standard ROOT minimization method [74]. The bottom row shows the respective decompositions coming from the same fit. In figure 5.10 we show the evolution of all eleven parameters as a function of ν.

As mentioned earlier, the primary goal behind our centrality evolution study was to provide a comparison between Au and Cu species at the same center of mass energy. The importance of such a comparison study was pointed out in previous studies [58]. This comparison only focuses on three parameters out of our eleven parameter fit, which are related to the 2d Gaussian structure. A brief summary of the definition of all eleven parameters is shown in table 5.1, while a detailed discussion can be found in [58]. One of the key findings from the latter reference is

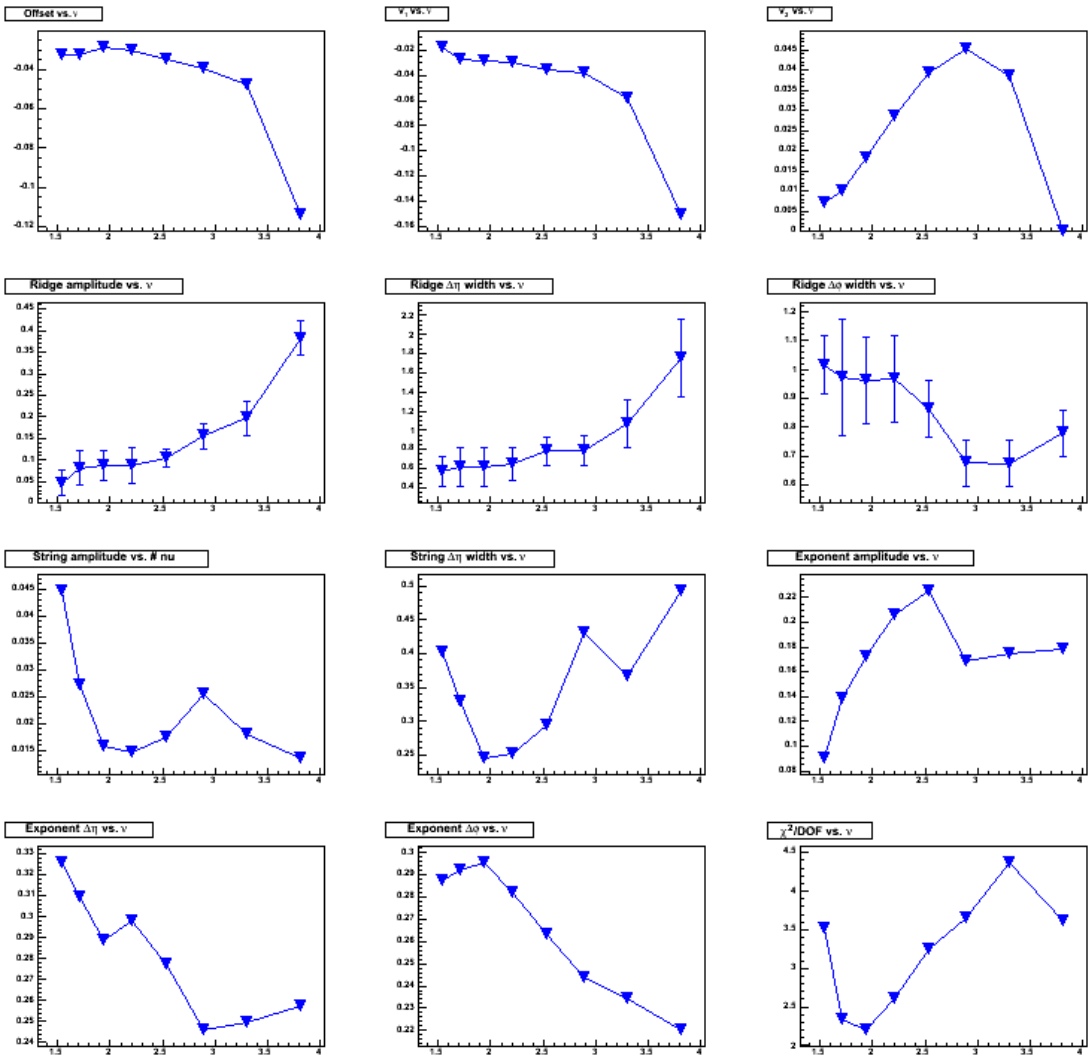

Figure 5.10: The centrality evolution of all 11 parameters in the fit and the χ^2/DOF as a function of ν.

the anomalous centrality evolution of the 2d Gaussian amplitude and $\Delta\eta$ width in Au + Au collisions. Figure 5.11 shows the evolution of those two parameters and the near side 2d Gaussian volume where the volume has been calculated using the formula, $2\pi a_3 a_4 a_5$ (2d Gaussian volume).

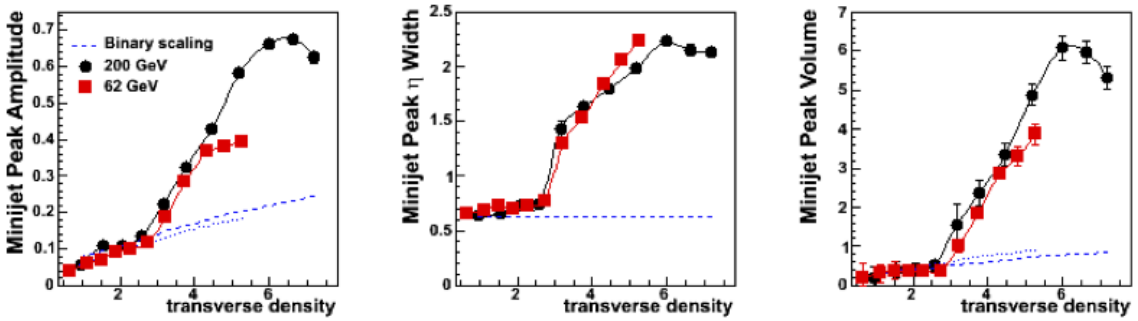

Figure 5.11: The near side 2d Gaussian peak amplitude, $\Delta\eta$ width, and volume for 62 GeV (red) and 200 GeV (black) as a function of transverse particle density $\widetilde{\rho}$. The blue lines show binary scaling expectations for 62 GeV (dotted line) and 200 GeV (dashed line) [58].

We can clearly observe the departure of the parameters from the expected binary scaling values as a function of transverse particle density $\widetilde{\rho}$ which is defined as,

$$\widetilde{\rho} = \frac{3}{2}\frac{dN_{ch}}{d\eta}/\langle S\rangle. \tag{5.2}$$

where $\widetilde{\rho}$ is defined as the final state particle density per unit η. The factor 3/2 account for the neutral hadrons and $\langle$ S $\rangle$ gives the overlap area of the initial collision [58].

A study comparing two species is a direct measure of the validity of binary scaling. We report the first results of this comparison as a function of ν variable and

Table 5.1: A brief summary of fit parameters

Parameter	Parameter name	Description
a_0	Offset	Estimates a negative offset for positive correlation structures in data
a_1	-cos($\Delta\phi$) amplitude	local and global momentum conservation
a_2	cos($2\Delta\phi$) amplitude	elliptic flow [82]
a_3	2d Gaus. amplitude	amplitude of the ridge
a_4	2d Gaus. $\Delta\eta$ width	$\Delta\eta$ width of the ridge
a_5	2d Gaus. $\Delta\phi$ width	$\Delta\phi$ width of the ridge
a_6	1d Gaus. amplitude	longitudinal fragmentation amplitude
a_7	1d Gaus. $\Delta\eta$ width	longitudinal fragmentation $\Delta\eta$ width
a_8	2d Expo. amplitude	amplitude of HBT and e^+e^- contamination
a_9	2d Expo. $\Delta\eta$ width	$\Delta\eta$ width of e^+e^- contamination
a_{10}	2d Expo. $\Delta\phi$ width	$\Delta\phi$ width of e^+e^- contamination

the results are shown in figure 5.12. All three parameters behave similar to previous studies and the exact

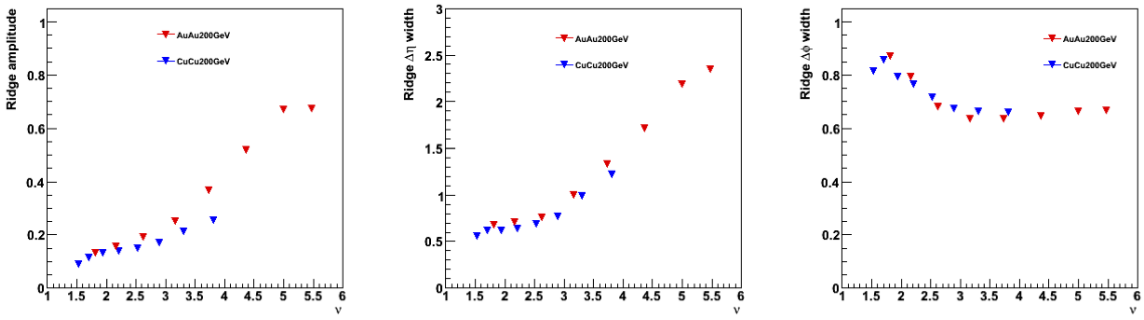

Figure 5.12: 2d Gaussian (we refer to as "ridge") parameter comparison between Au + Au and Cu + Cu at $\sqrt{S_{NN}} = 200$ GeV.

values compare reasonably well. Generally, all eleven parameters of the previous Au + Au analysis and our Cu + Cu analysis agree very well. As it is expected, Au + Au amplitude yields a higher value at larger ν values compared to Cu + Cu. The $\Delta\eta$ broadening of both systems is increasing as a function of ν and this evidence directly supports the fact that initial state correlation effects translate into final state correlations in an expanding medium (see section 6.2).

5.3.1 Theory comparison

We compare to a model with **C**olor **G**lass **C**ondensate (**CGC**) initial conditions [83,84]. CGC is a novel approach which allows for first principle investigation of non-perturbative QCD. It follows from the gluon saturation picture for particles carrying a low momentum fraction(**x**) in an accelerated nucleus or a nucleon. At small

x the gluon density rises and fill up the phase space to a saturation scale denoted as Q_s[85,86,87] where Q^2 is the momentum transfer in a scattering between two partons. A coherent state of gluonic matter(CGC) is achieved at high densities which allows a classical treatment to QCD [88,89].

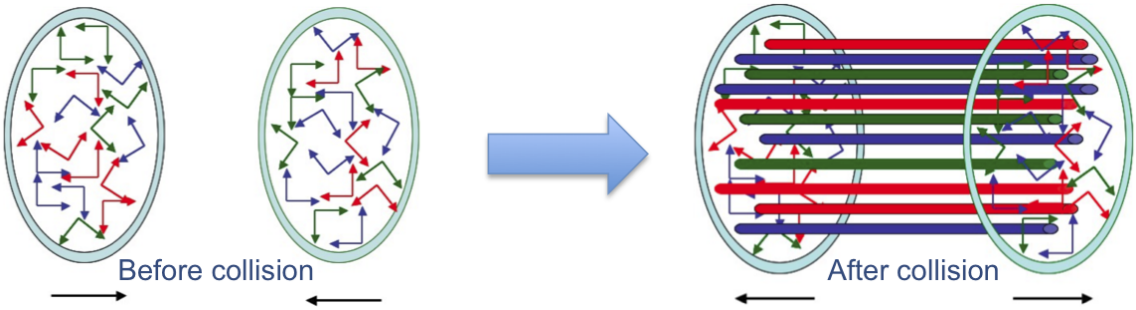

Figure 5.13: On the left: The collision of two sheets of Colored Glass. On the right: The longitudinal color electric and magnetic fields made in hadron collisions [91].

The schematic in figure 5.13 illustrates the idea behind dynamics of CGC. In the initial nuclei, the gluons are represented via randomly oriented chromo-electric and magnetic fields. Immediately after the collision(interaction) the fields become purely longitudinal color fields which are known as color flux tubes. Finally the flux tubes evaporate into particles via quantum instabilities. A more detailed discussion on CGC can be found in [90]. The time evolution of this system and the resulting correlations in the hadronic matter have been studied extensively in [90], and we compare our experimental results to these predictions.

Figure 5.14 and 5.15 schematically describes the theory. In the left plot of figure 5.14, we see an isotropic emission of particles from flux tubes with no radial push outward, which will lead to an uncorrelated structure in the final state hadrons.

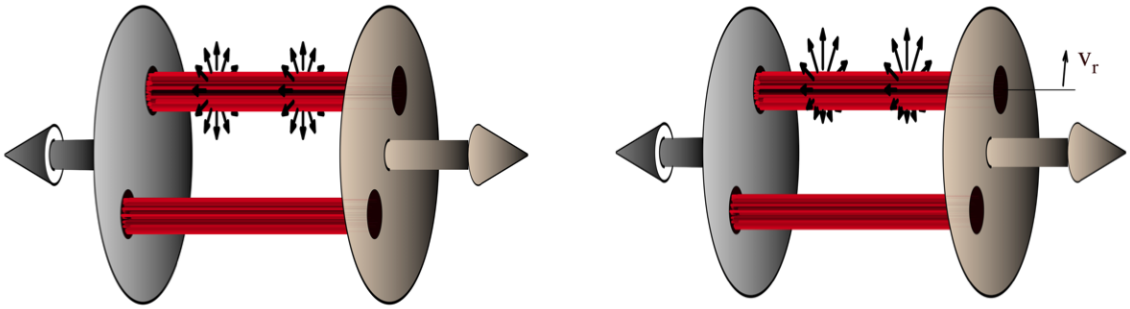

Figure 5.14: On the left: Particles does not experience a radial push. On the right: Particles experience a radial push from the medium. (Gelis, BNL 2010)

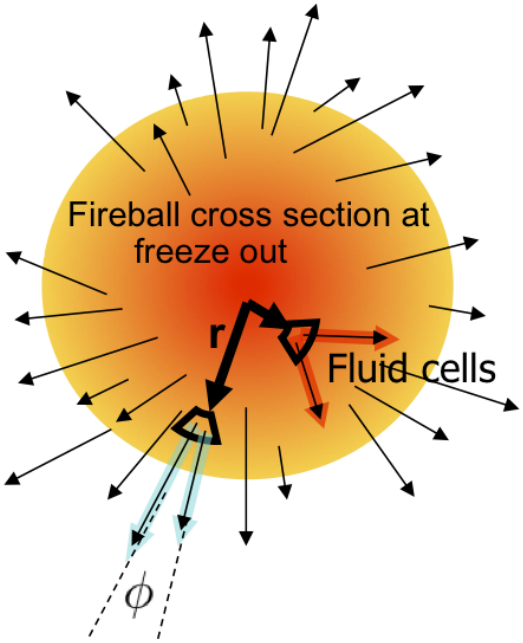

Figure 5.15: Azimuthal view of the expanding system. Azimuthal opening angle is larger at smaller radius [90]

However, due to the medium created in a collision, there exists a pressure gradient radially outward acting on the particles which are produced from flux tubes. This pressure gradient pushes the particles in a preferred direction, thus generating a correlation structure in the final state. Figure 5.15 shows a couple of relevant parameters for the theory calculation. As the particles created by flux tubes can be treated as fluid cells at different radii, the mean transverse radial velocity of a fluid cell depends on the radial position. Also the opening angle ϕ for each fluid element depends on the radial position. The corresponding relations are shown in equations 5.3 and 5.4 respectively. Applying these conditions, an average opening angle and the correlation amplitude on the near side is calculated using the generated particle pair distribution [90]. However it is important to point out that

$$\mathbf{v_t} \approx \lambda \mathbf{r_t} \tag{5.3}$$

$$\phi \approx (\lambda \mathbf{r_t})^{-1} \tag{5.4}$$

the theory does not describe the away side ($\Delta\phi \approx \pi$) correlation structure and the $\Delta\eta$ dependency of the near side correlation structure. Currently the CGC theorists are working on improving their approach by coupling it to a hydrodynamical transport code.

Figure 5.16 shows the comparison of theory predictions to our extracted fit parameters to the ridge amplitude and $\Delta\phi$ width [92,93,94]. The shaded bands represent the theoretical error which is mainly due to the blast wave model [95,96,97] parameters T (temperature) and β (velocity) used in the theory to describe the radial flow. In

this model, CGC is applied only to determine the initial parton density. For the amplitude comparisons, the theory curve

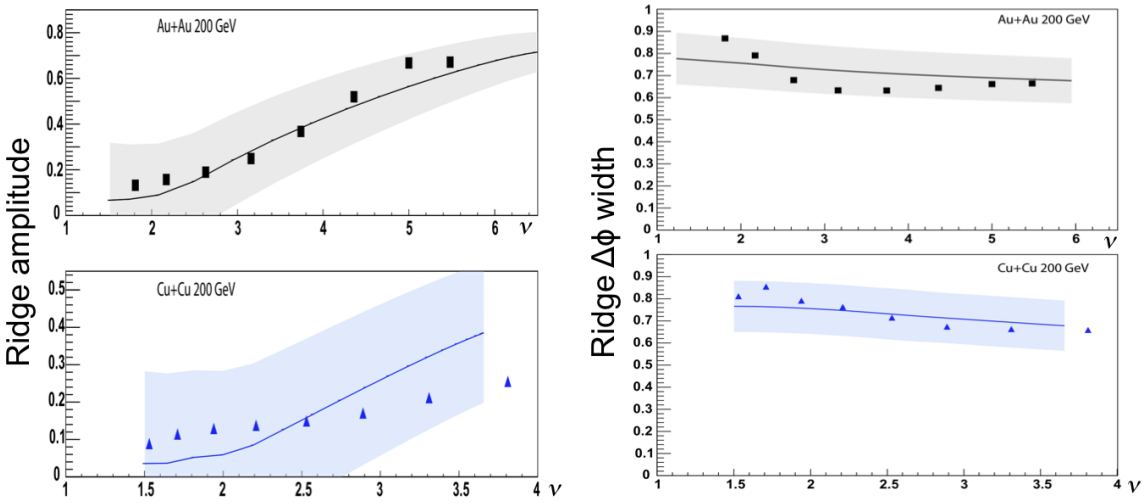

Figure 5.16: Top row: Ridge amplitude and $\Delta\phi$ width comparison for Au + Au data. Bottom row: The same as above for Cu + Cu data.

is scaled to the most central bin value. After scaling the centrality dependence of the experimental amplitudes for both Cu + Cu and Au + Au systems is well reproduced.

5.4 Transverse momentum dependence studies

As mentioned before, the transverse momentum evolution of di-hadron correlations in 0-10% centrality bin was carried out to map the kinematic region neglected in previous studies [22,76,77]. We hope to study the connection between the high and

low p_T kinematic regions in the context of "ridge" formation. At hight p_T we should be sensitive to jet physics, whereas at low p_T and intermediate p_T we have many convoluting effects such as, elliptic flow, string fragmentation, HBT, mini-jets, resonances and possible novel QCD phenomena.

We first report our raw data spectra for both, Cu + Cu and Au + Au 200 GeV, and show the measured correlation function compares to the structures previously reported for high p_T [77]. Then we show the results from our model study and related theoretical comparisons [98,99].

5.4.1 Correlation function comparisons

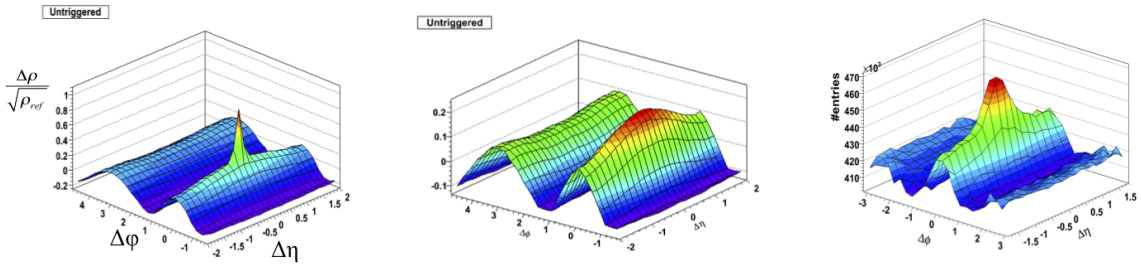

Figure 5.17: Di-hadron correlation structures using 0-10% Au + Au 200 GeV data. Left: Correlation structure for 0-10% centrality from our analysis using all charged particle pairs ($p_T > 0.15$ GeV/c). Middle: Correlation structure after subtracting the HBT/e^+e^- contribution using our 2d exponential model component. Right: Di-hadron correlation structure at high p_T from [77].

Figure 5.17 shows the two extremes of the kinematic region we hope to map using our transverse momentum evolution study. In the left figure the HBT/e^+e^- peak obscures the long range correlation structure, thus we subtract the contribution using our 2d exponential model component (see section 4.5). The di-hadron structure in

the left and middle panel consists of charged particle pairs using the full p_T range in STAR ($p_T > 0.15$ GeV/c) whereas the structure in the right most panel consists of leading particles (trigger) with $3 \leq p_T \leq 4$ GeV/c and associated particles with $p_T \geq 2$ GeV/c. As we can observe in figure 5.17, the inclusion of low p_T particles generates a monolithic structure on the near side compared to the structure at high p_T which is seen as a combination of a long range and a short range structure in $\Delta\eta$.

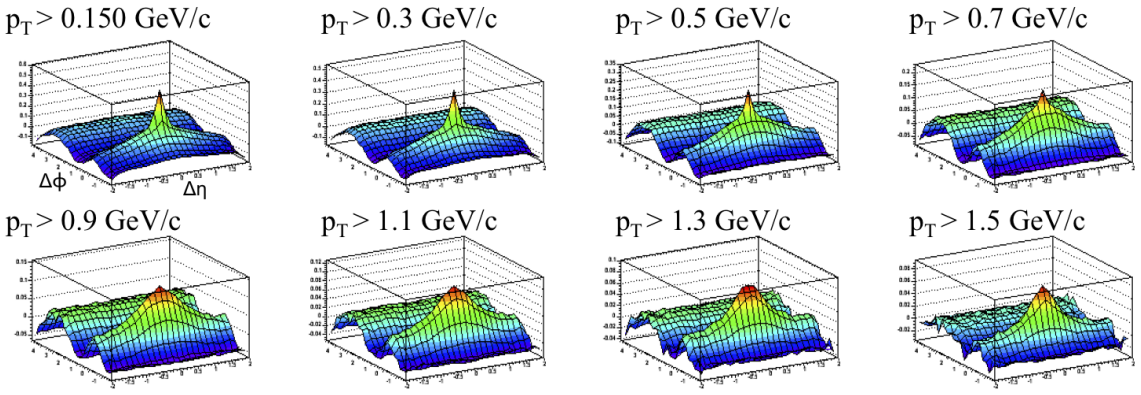

Figure 5.18: Transverse momentum evolution of di-hadron correlation in 0-10% centrality bin using Cu + Cu 200 GeV data.

Figure 5.18 and figure 5.19 show the detailed results for the p_T evolution of di-hadron correlation functions using Cu + Cu and Au + Au data, respectively. The data are obtained by increasing the lower momentum threshold for both charged particles as labeled in the figure.

The correlation functions reveal a smooth evolution of the near side structure. The long range correlation strength reduces at high p_T and the jet structure becomes more prominent. Around $p_T > 2.1$ GeV/c in figure 5.19 we reproduce the structure of the triggered analysis (fig. 5:17 right panel). While the higher track density in Au + Au enables us a better statistical reach in p_T compared to Cu + Cu, it also

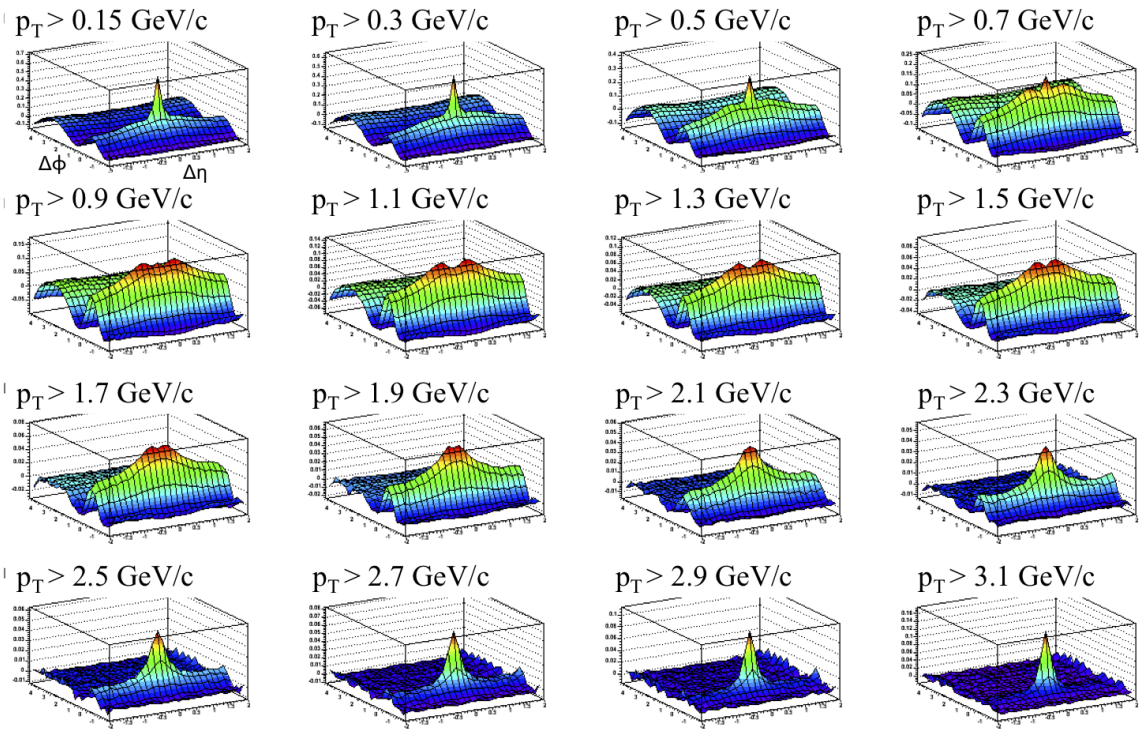

Figure 5.19: Transverse momentum evolution of di-hadron correlation in 0-10% centrality bin using Au + Au 200 GeV data.

generates a dip at ($\Delta\eta = 0$, $\Delta\phi = 0$) for lower p_T threshold cuts. This is understood mainly via Coulomb repulsion between close tracks in a high track density environment. It is confirmed using charge dependent di-hadron correlations (fig. 5.20 and fig. 5.21). The like sign (++ and $--$) charged tracks repel in Au + Au (fig. 5.20). A smaller dip structure at (0,0) remains even for unlike sign pairs ($+-$) (fig. 5.21) which is due to tracking inefficiencies due to our small angle rejection cut [58].

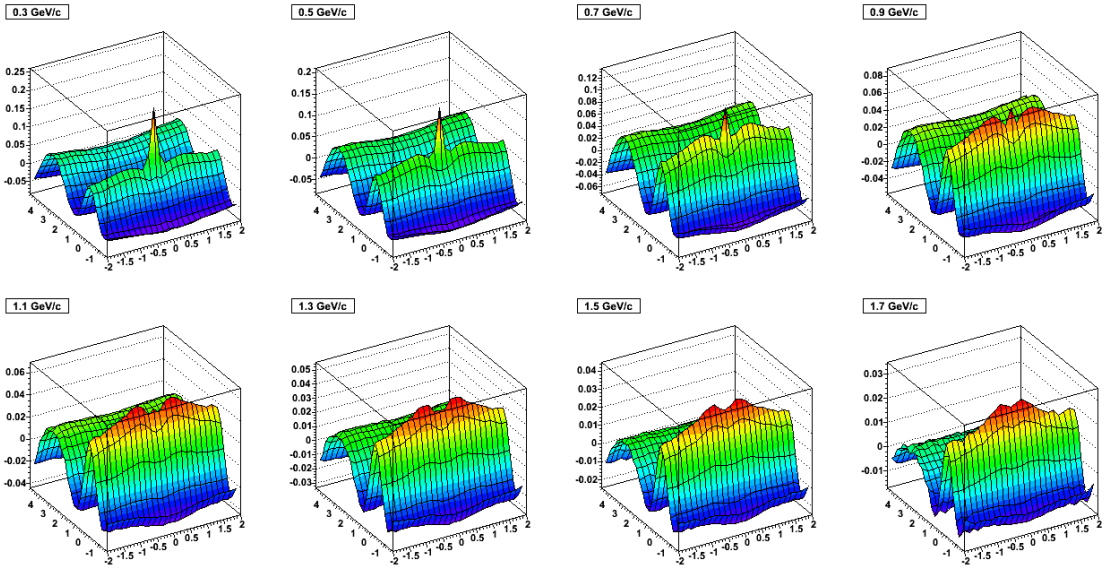

Figure 5.20: p_T evolution of like sign pairs for eight selected bins which shows a depletion of pairs in the charge independent di-hadron correlation structures.

Before modeling the data, we modify the small angle pair behavior. The HBT/e^+e^- pair contribution is subtracted using our 2d exponential model and the small angle $\Delta\eta$x$\Delta\phi$ bins corresponding to the dip are excluded from the fit by setting the statistical error to zero. A Gaussian fit is then applied to determine the proper bin content of the excluded bins. For the complete fit function application the bins are

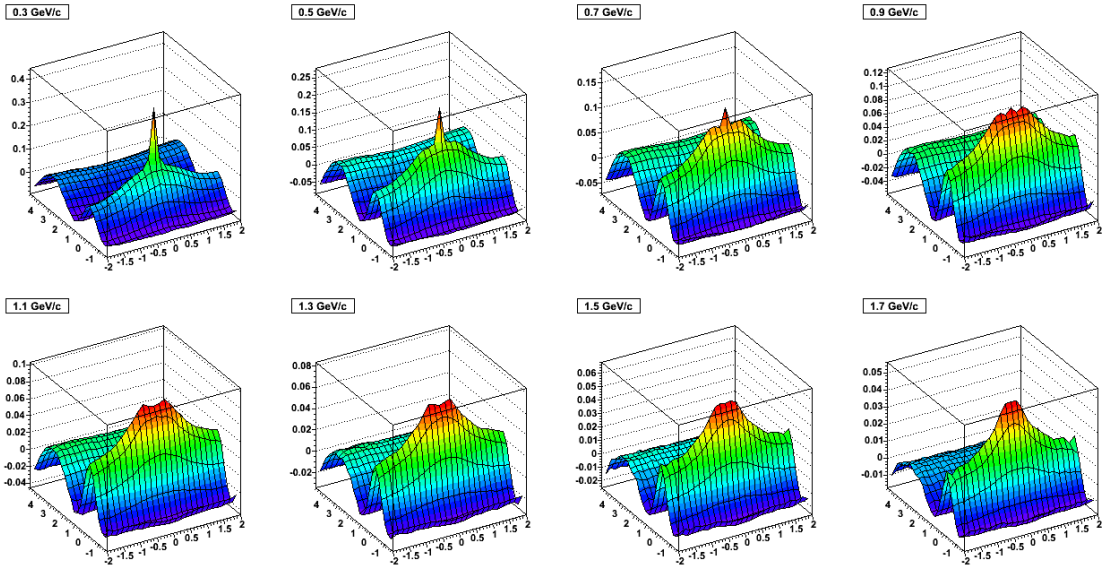

Figure 5.21: p_T evolution of unlike sign pairs for eight selected bins which shows a depletion of pairs in the charge independent di-hadron correlation structures.

then filled with the content extracted from the Gaussian fit. Figure 5.22 shows the resulting di-hadron correlation functions. In figure 5.23, we show the same functions with a fixed scale for the z-axis, which better illustrates the reduction in correlation strength for higher p_T threshold cuts. It also shows the "ridge" correlation strength reducing and the jet correlation strength increasing for high p_T threshold cuts. The increase of jet correlations at high p_T cuts does not contradict the fact that the total yield of particle pairs is decreasing, it rather documents that the correlation strength in the small angle bins are increasing. This observation was confirmed by looking at the raw "sibling" and "mixed" pair distributions where we found that indeed the total number of pairs decreases monotonically for both pair types as a function of the p_T cut. However, if we consider the small angle pair evolution for both types, at high p_T, the relative decrease in the "sibling" pairs is lower compared to the "mixed"

pairs. Thus the ratio leads to a relative increase in correlation strength at high p_T in the small angle region.

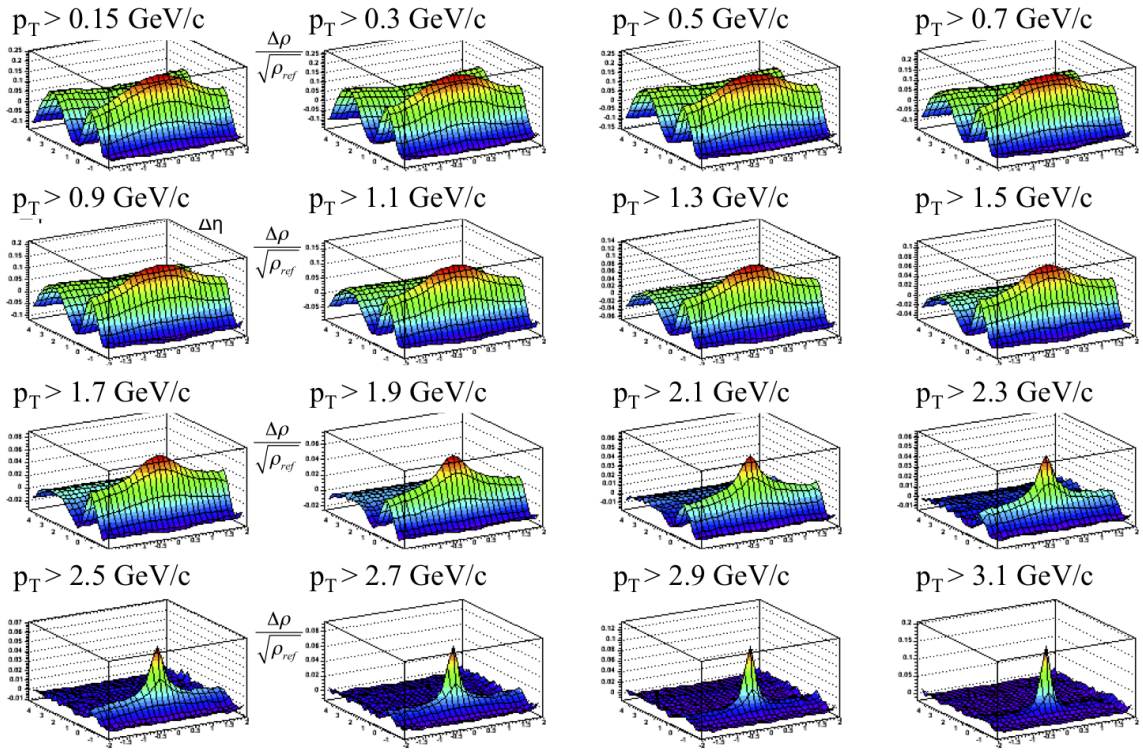

Figure 5.22: Di-hadron correlation structure evolution using Au + Au 200 GeV data after removing the small angle effects.

5.4.2 Model study with higher order harmonics

Focusing on the most central bin not only gives us an opportunity to study the highest energy density environment, it also gives us an opportunity to test recent theory predictions for the existence of higher order harmonics [71,72]. As shown in figure 4.6, theory prediction states that higher harmonics contributions are important in very central high p_T data. We first search for evidence of higher order harmonics

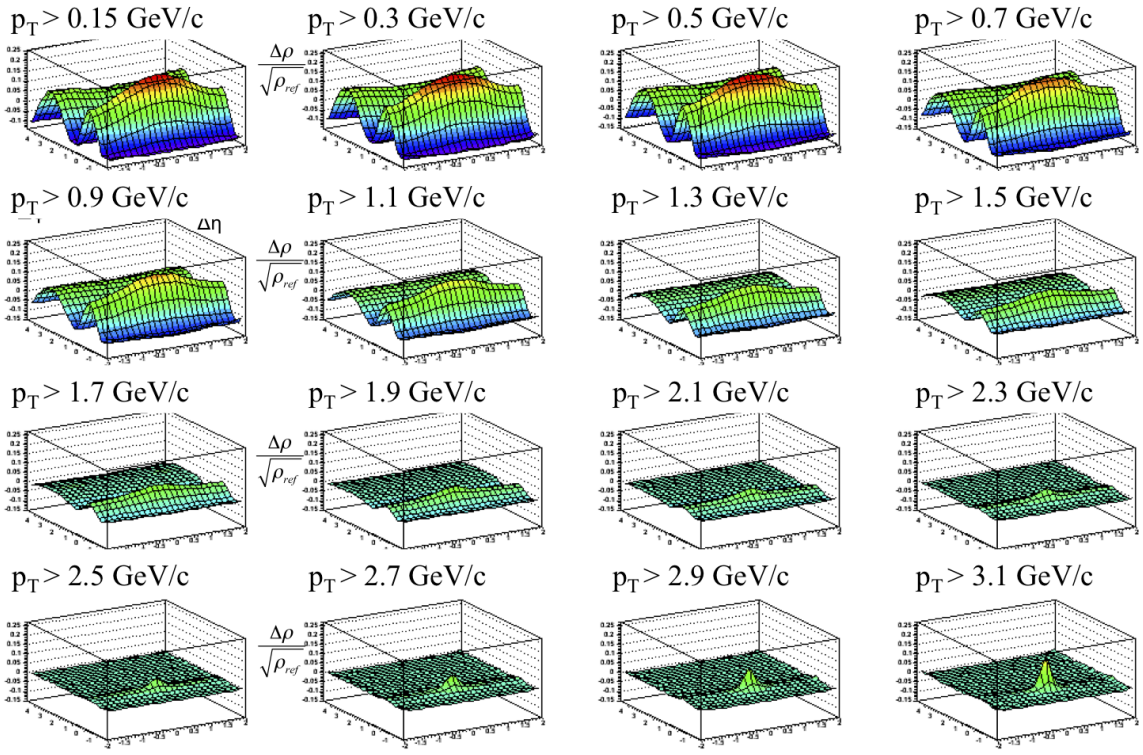

Figure 5.23: Di-hadron correlation structure evolution using Au + Au data in figure 5.22 with a fixed scale in the z-axis illustrates the reduction in correlation strength.

in the data [99]. Figure 5.24 shows the projections of di-hadron correlations in three p_T intervals for 0-1% central data. We select the centrality criteria to come closest to the theory prediction (impact parameter $b = 0$) and evolve the di-hadron correlation as a function of p_T. At a higher p_T, we start to observe a double hump structure in the away side di-hadron projection (fig. 5.24). The peak positions ($2\pi/3$ and $4\pi/3$) of the structure agrees with a $\cos(3\Delta\phi)$ model description which also propagates to the near side. Based on this evidence for higher harmonics we fit the data using a fit model which incorporates higher order harmonics. The function takes the following form:

$$F = a_0 + a_1 cos(\Delta\phi) + a_2 cos(2\Delta\phi) + a_3 cos(3\Delta\phi) + a_4 cos(4\Delta\phi) + a_5 cos(5\Delta\phi) \tag{5.5}$$

Terms with n $\geq$ 6 are not supported by the data thus our model function terminates at $\cos(5\Delta\phi)$. We first investigated the residual structure after subtracting the harmonics contribution. Figure 5.26 shows an example fit to data using the model described in equation 5.5. Displayed here is the 0-10% data with $p_T \geq 1.7$ GeV/c cut. We observe that a model fit with higher harmonics alone does not describe the data. Similar residual structures have been observed for the other p_T cuts. Based on the evolution of the remaining structure, the least constrained model component we could introduce to equation 5.5 is a 2d Gaussian. Possible physics interpretation to the 2d Gaussian will be addressed in detail in chapter 6. The revised model function takes the form:

$$F = a_0 + a_1 cos(\Delta\phi) + a_2 cos(2\Delta\phi) + a_3 cos(3\Delta\phi) + a_4 cos(4\Delta\phi)$$
$$+ a_5 cos(5\Delta\phi) + a_6 exp\left\{-\frac{1}{2}\left[\left(\frac{\Delta\eta}{a_7}\right)^2 + \left(\frac{\Delta\phi}{a_8}\right)^2\right]\right\} \quad (5.6)$$

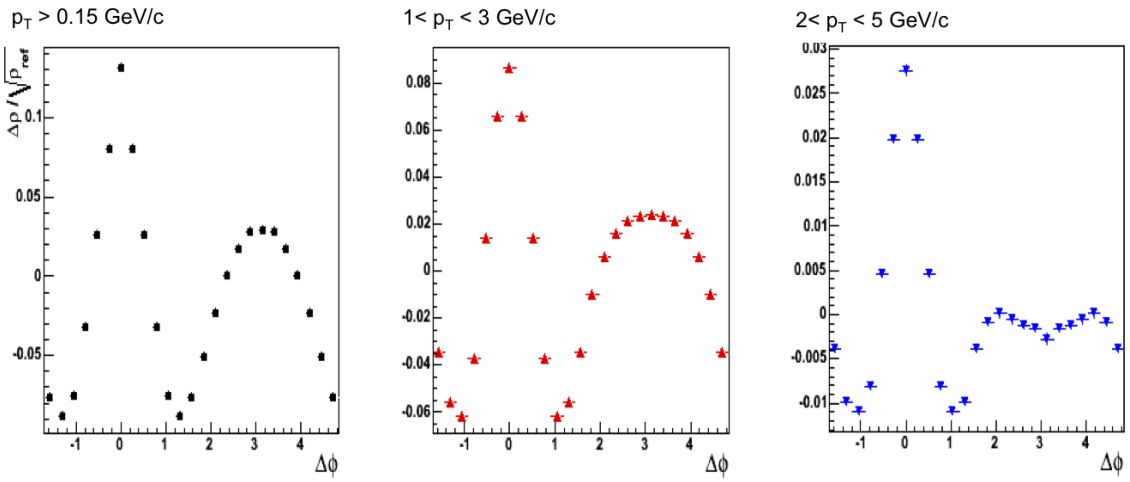

Figure 5.24: Projection of 2d di-hadron correlation structure on to $\Delta\phi$ axis for three p_T intervals in 0-1% very central bin.

An example fit with the revised model function (equation 5.6) is shown in figure 5.27. We observe that the residual peak structure from figure 5.26 is well addressed by the remainder inclusion. The residual structure corresponds to a χ^2/DOF of 5.47. In figure 5.28 we show a decomposition example for the $p_T \geq 1.7$ GeV/c correlation function.

For the p_T study we summarize our results by showing the $\langle p_T \rangle$ evolution of the remainder and the summed harmonics ($n \geq 2$) structure. Figures 5.29 and 5.30 shows the p_T evolution of these structures for six selected bins. The remainder amplitude

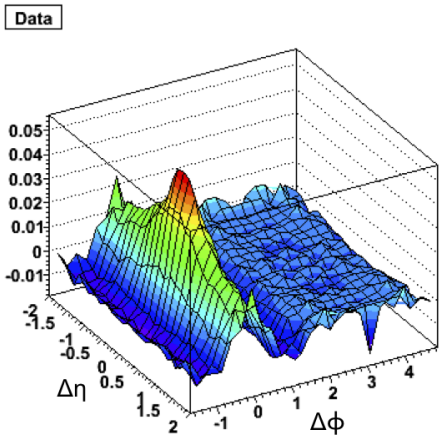

Figure 5.25: 2d di-hadron correlation structure corresponding to the right panel projection shown in figure 5.24

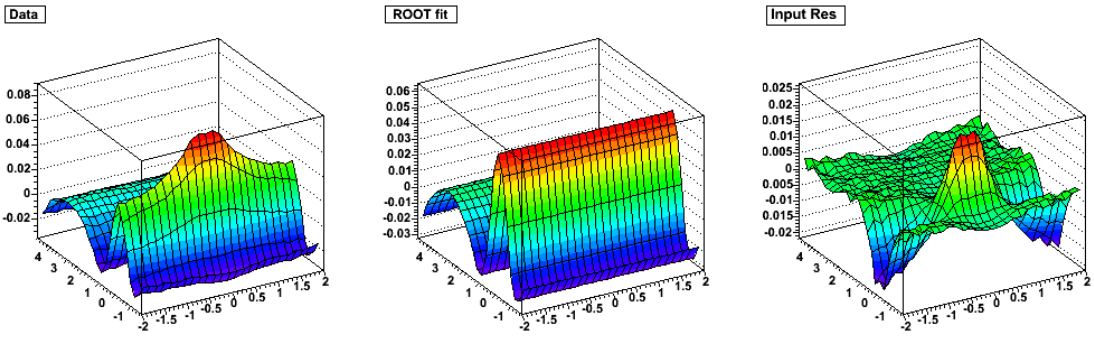

Figure 5.26: An example fit using the model function in equation 5.5. The data comes from 0-10% centrality bin with a $p_T \geq 1.7$ GeV/c cut.

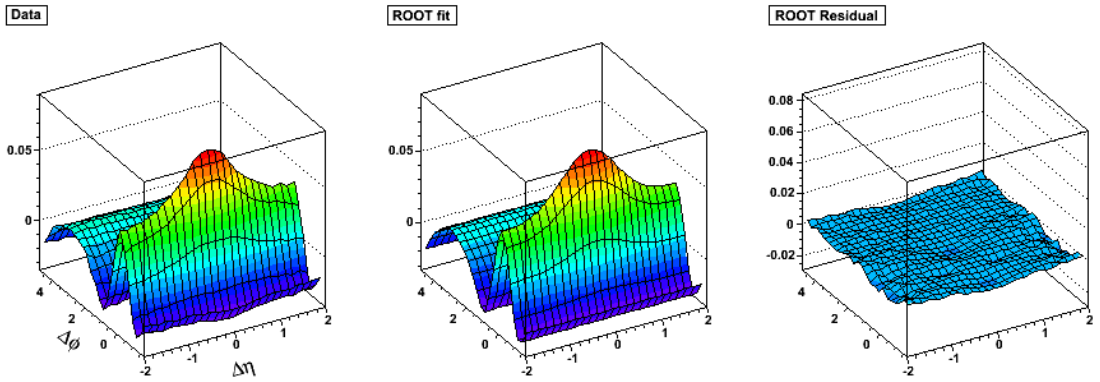

Figure 5.27: An example fit using the model function in equation 5.6. The data comes from 0-10% centrality bin with a $p_T \geq 1.7$ GeV/c cut.

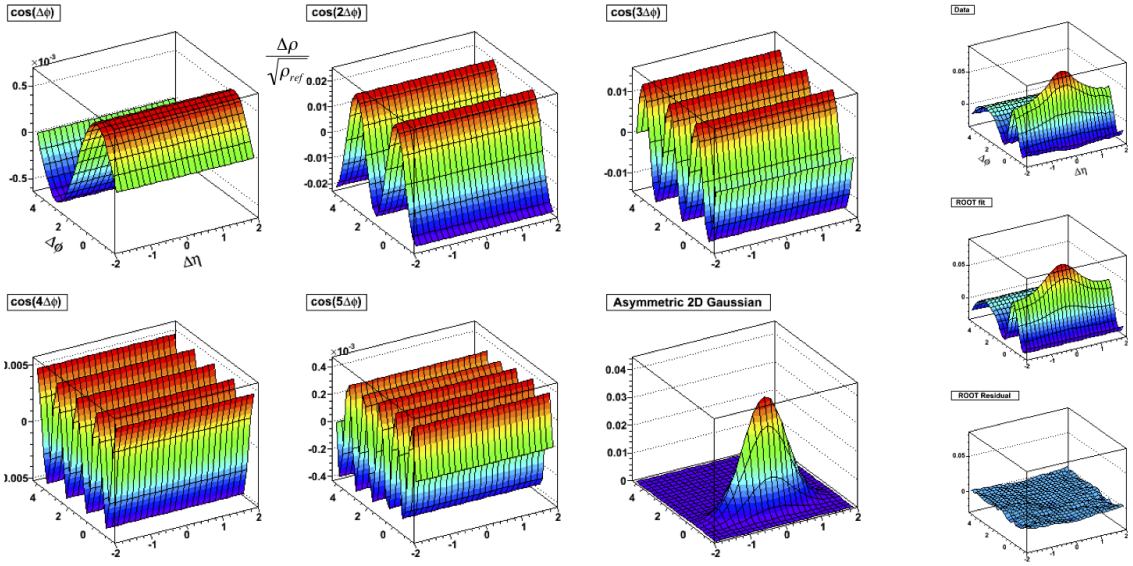

Figure 5.28: A decomposition example (left) of fitting along side the data, model fit and residual structure (right column) for $p_T \geq 1.7$ GeV/c cut.

drops until the $p_T \geq 2.1$ GeV/c cut and strengthens afterwards due to correlated particles in the jet fragmentation process, which occurs in a narrow $\Delta\eta$x$\Delta\phi$ space. In contrast the widths of the remainder reduce as a function of $\langle p_T \rangle$. The summed harmonic structure amplitude on the near- and away-side drops, while the away-side width becomes broader as a function of p_T. Figures 5.31 and 5.32 show the quantitative evolution of the fit parameters. In figure 5.31 we show the amplitude comparison between the summed v_n ($n \geq 2$) component (blue data points) and the remainder (red data points). The evolution of those two amplitudes are comparable in the $0.9 < \langle p_T \rangle < 2.1$ GeV/c range. Below $\langle p_T \rangle \approx 0.9$ GeV/c we observe a monotonic decrease and an increase of summed harmonic amplitude and the remainder amplitude respectively, with decreasing $\langle p_T \rangle$. Even though the general trend of the remainder widths is to reduce as a function of $\langle p_T \rangle$, $\Delta\eta$ width slightly increases and then monotonically decreases after $\langle p_T \rangle \approx 0.9$ GeV/c. The $\Delta\eta$ and $\Delta\phi$ widths are comparable for $\langle p_T \rangle > 2.5$ GeV/c thus the remainder become symmetric in widths. Finally, we report the results from our comparison to p + p data and hydrodynamical scaling $\frac{v_n^{1/n}}{v_2^{1/2}}$ (for $n = 3, 4$). A detailed discussion of these results is presented in chapter 6. Figures 5.33 and 5.34 show the $\Delta\phi$ and $\Delta\eta$ width comparison between the remainder and corresponding p + p near-side peak. Both remainder widths are greater than the corresponding p + p widths for all $\langle p_T \rangle$. At higher $\langle p_T \rangle$ the width are modified by a factor of two with respect to p + p. The maximum relative broadening is a factor of two larger in $\Delta\eta$ compared to $\Delta\phi$. We hope to discuss modified jet phenomena via this comparison. In figure 5.35 we use our extracted parameters to formulate the harmonic scaling relation $\frac{v_n^{1/n}}{v_2^{1/2}}$ (for $n = 3, 4$) and plot as a function

of $\langle p_T \rangle$ in order to study the theory predictions made in [100]. In chapter six (discussion) we discuss our findings in relation to understanding a QGP formation, QGP medium properties and medium modified jet phenomena in QGP.

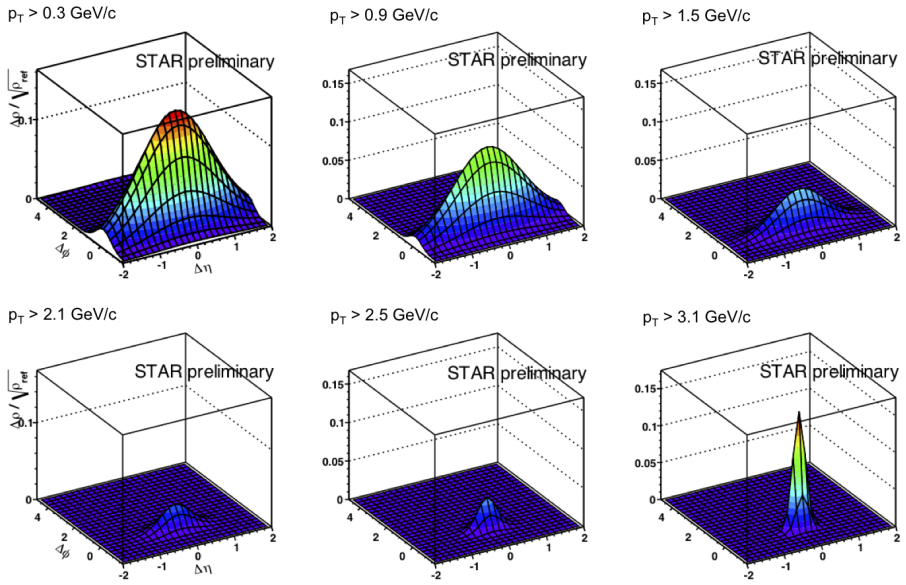

Figure 5.29: The remainder evolution as a function of the p_T cut for six selected bins.

5.4.3 The fit quality and χ^2 test for goodness of fit

In order to test the fit quality we calculate the standard χ^2/DOF which is shown in figure 5.36. For $x_i (i = 1, 2, 3, ..., \nu)$ variables, the χ^2 is defined as:

$$\chi^2 \equiv \sum_{i=1}^{\nu} \frac{(x_i - \mu_i)^2}{\sigma_i^2} \tag{5.7}$$

where μ_i and σ_i^2 correspond to the mean and variance of the variable x_i respectively. Ideally we would expect that each term of the sum is one since the random

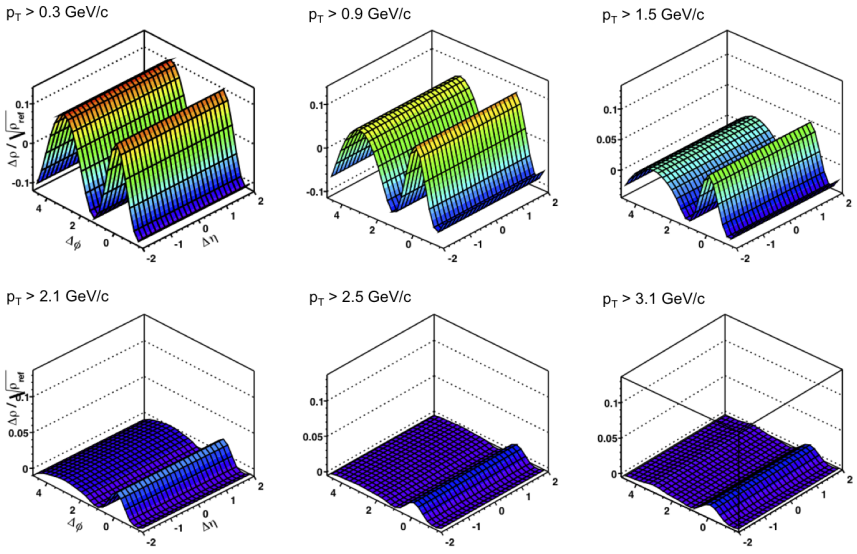

Figure 5.30: The summed harmonic structure $(v_2 + v_3 + v_4 + v_5)$ as a function of the p_T cut for six selected bins.

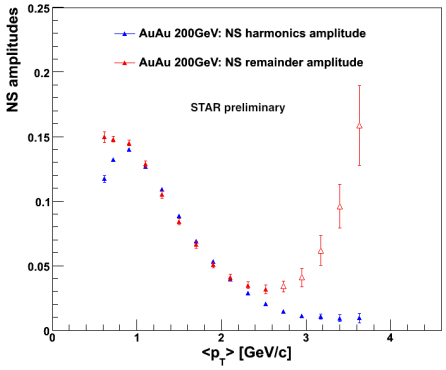

Figure 5.31: The amplitude comparison between summed v_n components and the remainder as a function of $\langle p_T \rangle$.

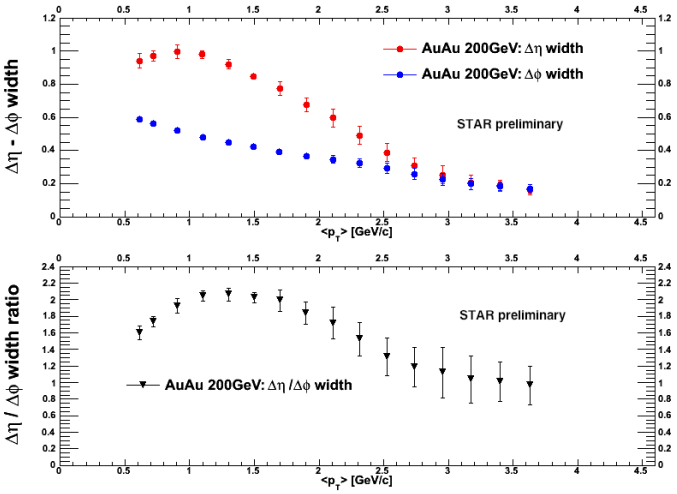

Figure 5.32: The remainder $\Delta\eta$ and $\Delta\phi$ width comparison as a function of $\langle p_T \rangle$. Top panel shows the individual parameters and the bottom panel shows the ratio between the parameters.

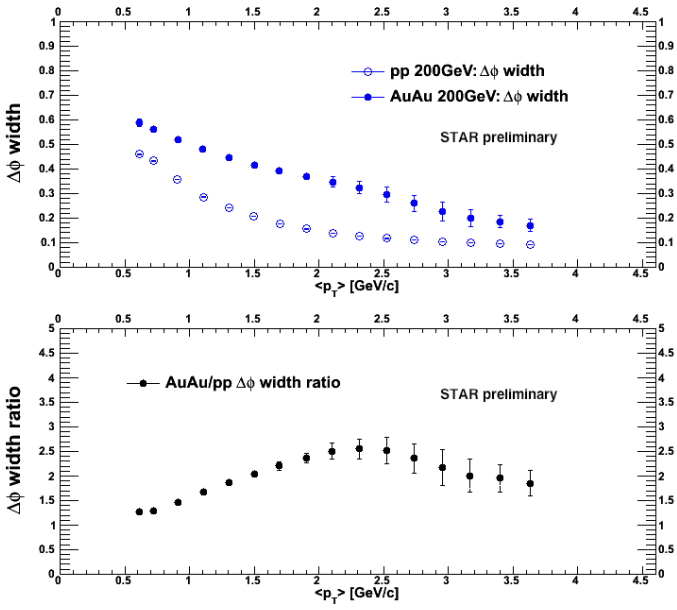

Figure 5.33: The $\Delta\phi$ width comparison between Au + Au remainder structure and corresponding near side peak structure in p + p. Top panel shows the individual parameters and the bottom panel shows the ratio between the parameters.

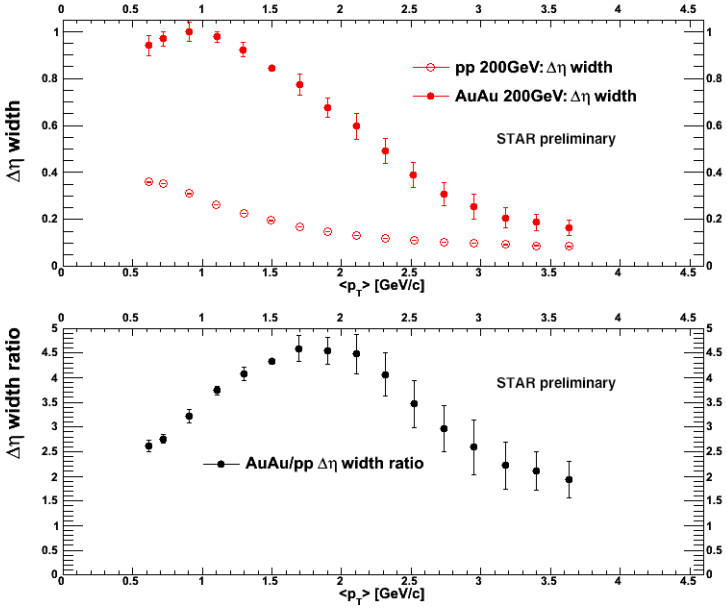

Figure 5.34: The $\Delta\eta$ width comparison between Au + Au remainder structure and corresponding near side peak structure in p + p. Top panel shows the individual parameters and the bottom panel shows the ratio between the parameters.

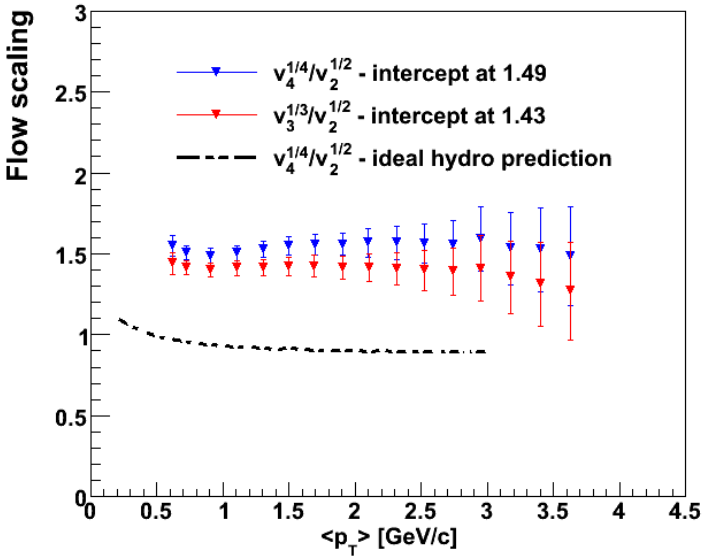

Figure 5.35: Higher order harmonic scaling relations, $\frac{v_4^{1/4}}{v_2^{1/2}}$ and $\frac{v_3^{1/3}}{v_2^{1/2}}$ as a function of $\langle p_T \rangle$.

fluctuation of the value x_i about the mean should be close to the variance. Therefore if we can choose μ_i and σ_i correctly, our χ^2 value should be equal to ν. The model function which defines the best μ_i values that satisfies this condition would describe the data well. If χ^2 become larger than ν given that our σ_i estimates are accurate, then the model function do not describe the data well. In our data, we calculate the σ_i which is the error on data, using square error propagation. The σ_i values we get are on the order of 10^{-3}. Figure 5.37 shows the χ^2 distribution for three ν values. The χ^2 distribution with ν degrees of freedom is defines as:

$$f(\chi^2) = \frac{1}{2^{\nu/2}\Gamma(\nu/2)} e^{-\chi^2/2} (\chi^2)^{(\nu/2)-1} \tag{5.8}$$

with a mean of ν and a variance of 2ν. The distribution become symmetric for larger ν values even though it is highly skewed to the left for small ν values. In a test for goodness of fit, we have to consider the possibility that our x_i variables are not independent to each other for the most general case. Therefore depending on the number of relations or constraints (say r) between the variables x_i our degrees of freedom (ν) reduces to $N - r$. In our fit model study, x_i's are the bins in the $\Delta\eta$x$\Delta\phi$ space (625 in total) and the constraints are the number of parameters in the fit function (9 in total). Therefore the χ^2 for our fits should be close to 616 for our model study. In figure 5.36 we observe large χ^2/DOF values for some of the fits.

We investigated this large χ^2 issue since our extracted parameters from the model fit compare very well with other independent studies in the STAR experiment (see chapter 6). Figure 5.38 shows the χ^2 distributions for eight selected p_T threshold

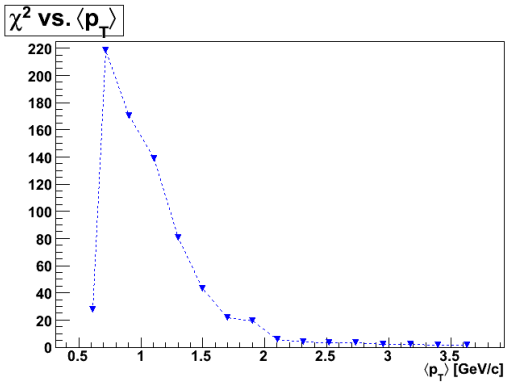

Figure 5.36: The χ^2/DOF of the fits as a function of $\langle\ p_T\ \rangle$.

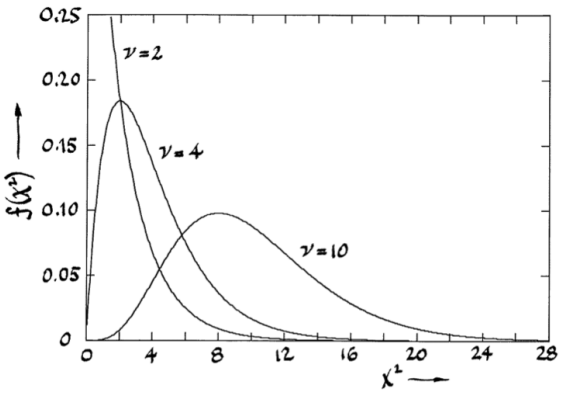

Figure 5.37: The χ^2 distribution for the three ν values, 2,4 and 10.

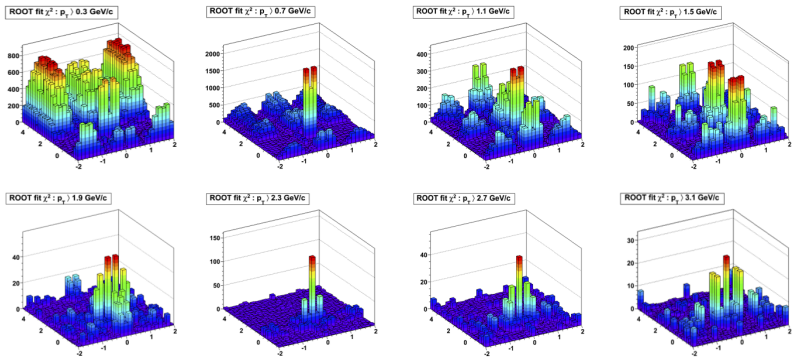

Figure 5.38: The χ^2 distribution from data modeling for eight selected p_T bins.

cuts from the fits to data. For all the p_T cuts, the χ^2 contribution is highest close to the origin since we corrected for the bins around (0,0). Except in the first two lowest p_T threshold bins ($p_T > 0.15$ and $p_T > 0.3$ GeV/c), the χ^2 distributions do not show a specific structure but rather randomly distributed. The χ^2 for the two lowest bins are driven by a saddle like structure seen on the away side, which we do not account for in our fit model. Even though possible model studies were carried out to address this away side correlation at low p_T, we fail to describe the observation in relation to a physical origin. We then looked into the residual distribution and computed the average residual contribution to each correlation structure and found that it is below a 3% level.

Chapter 6

Discussion

In this chapter we mainly focus on possible interpretations and model comparison studies to our data, in particular the parameters extracted from the momentum dependence of the di-hadron correlation structures. First we address the Fourier coefficients and show comparison studies to other independent measurements of v_n from the STAR experiment. Then we compare to predictions based on initial conditions and successive hydrodynamical evolution of the system and discuss in detail the implications for QGP formation and QGP medium properties in heavy ion collisions. Finally we address the remainder parameters and discuss possible jet modifications using the remainder width behavior and comparisons to p + p data. A possible link to calculating energy transport coefficient in the QGP based on the data at high $\langle p_T \rangle$ will be established. Other possible mechanisms are used to explain the remainder structure at lower $\langle p_T \rangle$.

6.1 Higher order Fourier coefficients

Comparison to other measurements from the STAR experiment

In order to test the reliability of the extracted higher order harmonics, v_n ($n = 2, 3, 4$) values were compared to an independent measurement from the STAR experiment [101].

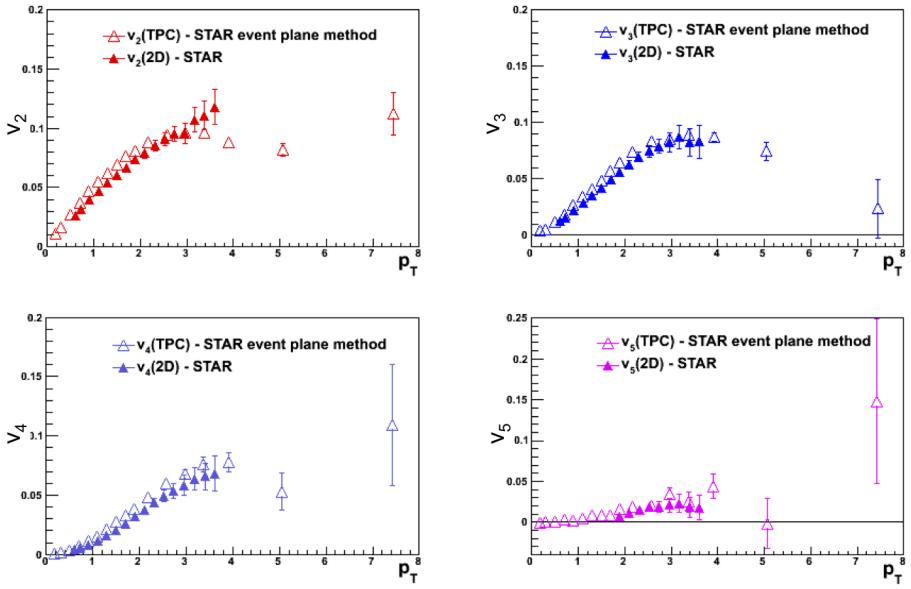

Figure 6.1: The comparison of extracted v_n coefficients to independent measurements from STAR.

Our model v_n parameters are not directly comparable to standard flow measurements from STAR. Measurements from di-hadron correlations need to be converted [82] using the following equation in order to be compared.

$$v_n(2D) = \sqrt{\frac{4\pi v_n(Fit)}{2(dN/d\eta d\phi)}} \tag{6.1}$$

In the above equation, $v_n(2D)$ represents the converted measure, $v_n(Fit)$ gives the extracted model fit value and $\frac{dN}{d\eta d\phi}$ is the charged particle distribution within the selected acceptance in the di-hadron correlation. The alternate method from STAR that we compare to correlates particles with reference to a reconstructed event plane, which is approximately the plane defined by the centers of the two heavy ions that collide.

$$v_n = \langle cos\, n(\phi - \Psi_R) \rangle \tag{6.2}$$

Equation 6.2 defines the v_n based on the event plane measurement [102]. Ψ_R is the reconstructed event plane or reaction plane (see figure 4.4). The event plane reconstruction is carried out using TPC charged tracks . Therefore, in order to suppress self correlations, and some of the non-harmonic correlation contributions, the measurement has been carried out in two hemispheres in $\Delta\eta$ with a 0.1 gap between the two. However, it is important to mention that correlations due to jet fragmentation still contribute to the extracted harmonic amplitudes in both cases at a few percent level [103]. Figure 6.1 shows good agreement between the two methods. This agreement confirms the reliability of the extracted parameters using di-hadron correlations.

Comparison to recent theoretical developments

In order to gain further insight into heavy ion collision physics, the extracted higher harmonic scaling relations have been compared to recent theoretical developments [104,105]. We first study the higher order Fourier harmonic scaling relation $\frac{v_n^{1/n}}{v_2^{1/2}}$ which is discussed in [100]. Ideal hydrodynamics predicts a value of $\simeq 0.5$ for the scaling relation $\frac{v_n^{1/n}}{v_2^{1/2}}$ [106]. However experiments support the relation $v_4 \simeq v_2^2$ as discussed in the references [107 - 110]. In these papers the discrepancy between ideal hydro prediction and experimental data have been attributed to the degree of thermalization in the QGP, elliptic flow fluctuations, eccentricity fluctuations in the initial geometry and viscous effects in the QGP. We compare to a recently developed theory which discusses the importance of fluctuations and the viscous evolution of the medium created in a heavy ion collision [118,119,120].

The extracted higher order harmonics were first transformed into $v_n(2D)$ using the prescription shown in equation 6.1. Then, as shown in figure 5.35, we produce the scaling relations using both v_3 and v_4 harmonics and find that the scaling relation holds for relatively low $\langle p_T \rangle$ and breaks at higher values. This exact behavior was predicted in [100] using a hydrodynamical evolution of the system with Glauber initial conditions. However, the important question to answer is what does the exact scaling ratio tells us. In figure 5.35, we also show the intercept value for both v_3 and v_4 scaling ratios. For $\frac{v_3^{1/3}}{v_2^{1/2}}$ it is 1.43 and for $\frac{v_4^{1/4}}{v_2^{1/2}}$ it is 1.49. In order to investigate the underlying physics mechanism that could generate these scaling ratio values, we compared to a very recent theoretical development based on CGC initial conditions and hydrodynamical flow [104,105].

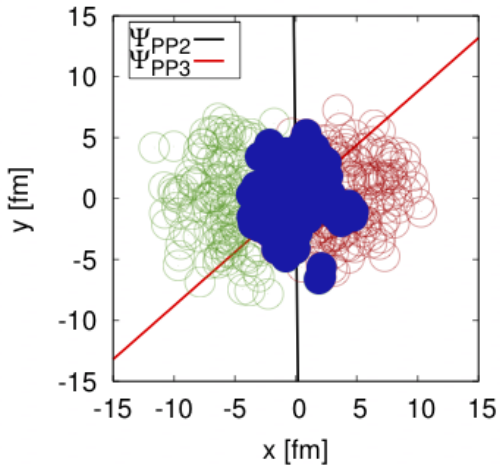

Figure 6.2: Green and red circles represents the nucleon distributions in a heavy ion collision using Glauber initial conditions which incorporates Woods-Saxon distributions to determine the initial nucleon positions. Blue blobs represents the energy distribution due to colliding nucleons. Ψ_{PP2} and Ψ_{PP3} depicts the event planes for ellipticity and triangularity.

In figure 6.2 the green and red circles represents the initial nucleon distribution determined using a Woods-Saxon potentials for incoming spectator nucleons (the nucleons which do not collide). The blue blobs represents the energy distribution due to the nucleons which have collided. At collision position, each nucleon is added to a 2D Gaussian energy density distribution with a width of $0.4\,fm$ which is a parameter in the model. Any two nucleons are assumed to collide if their relative transverse distance is less than $\sqrt{\sigma_{NN}/\pi}$ where σ_{NN} is the inelastic nucleon-nucleon cross section, which is $42\,mb$ at top RHIC energy of $\sqrt{S_{NN}} = 200\,GeV$. Further in figure 6.2, Ψ_{PP2} and Ψ_{PP3} denotes examples for ellipticity and triangularity axes. This Glauber initial condition model was improved very recently by coupling to color charge fluctuations using a modified CGC picture to incorporate quantum

fluctuations and followed by viscous hydrodynamical flow.

First, an Impact Parameter dependent saturation model (IP-Sat) [112,113] which incorporates high energy nuclear and nucleon wave functions has been combined with classical Yang-Mills description of glasma fields (CGC)[114 - 117] in heavy ion collisions. This improved model is called IP-Glasma model [104,105,118] which has the following properties.

- Nucleon positions are sampled using Woods-Saxon distribution
- Impact parameter dependent $Q_s^2(x, \mathbf{b}_\perp)$ is obtained for each nucleon by fitting IP-Sat model to deep inelastic scattering data from the HERA experiment
- The color charge squared per unit area, $g^2\mu^2(x, \mathbf{b}_\perp)$, is proportional to $Q_s^2(x, \mathbf{b}_\perp)$
- By adding all individual nucleon $g^2\mu^2(x, \mathbf{b}_\perp)$ at same x, the $g^2\mu^2(x, \mathbf{x}_\perp)$ is obtained for the nucleus where $x_\perp$ is the transverse position in the nucleus (see 6.3)

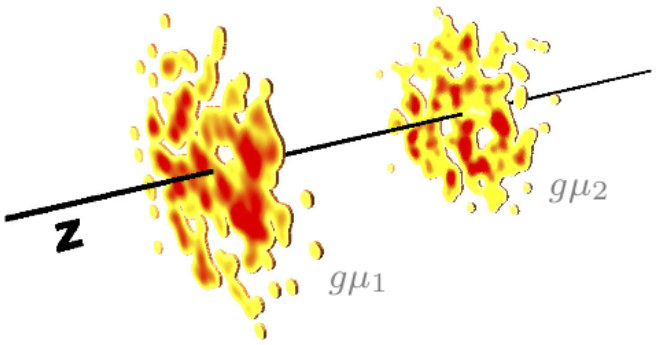

Figure 6.3: The color charge densities of incoming nuclei $g\mu$ for Au + Au collisions at 200 GeV. Higher densities are shown in red [118].

- Degree of correlation and fluctuation of the gluon fields in the incoming nuclei are shown in figure 6.4

- The characteristic correlation length is $1/Q_s$ thus allowing a finer granularity than the nucleon scale

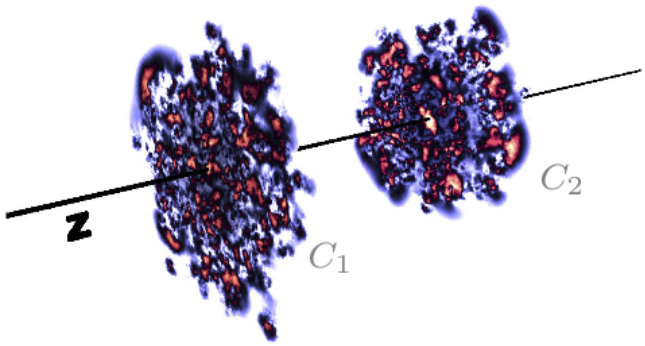

Figure 6.4: The degree of correlation and fluctuation in the gluon fields of the lead ions at $\sqrt{S_{NN}} = 2.76\,TeV$.

After the initial classical Yang-Mills (CYM) description ($\approx 0.2\,fm/c$) of this boost invariant configuration of gluon fields, the system is evolved using relativistic viscous hydro dynamics as prescribed in MUSIC [119 - 122] which is a 2 + 1D relativistic viscous hydrodynamical simulation. The hydrodynamical evolution requires the construction of the energy momentum tensor:

$$T^{\mu\nu}_{fluid} = (\epsilon + P)u^{\mu}u^{\nu} - Pg^{\mu\nu} + \Pi^{\mu\nu} \tag{6.3}$$

where ϵ is the energy density in the fluids rest frame, u^{μ} is the flow velocity, P is the local pressure using the equation of state at all transverse positions and $\Pi^{\mu\nu}$

is the shear viscosity. Solving the energy momentum tensor $T^{\mu\nu}_{CYM}$ for CYM description gives the initial conditions to the successive viscous hydrodynamical evolution considering energy momentum conservation ($\partial_\mu T^{\mu\nu} = 0$) and the equation of state. The equation of state used is $s95p\text{-}PCE$ which is derived using a hadron resonance gas model and fits to lattice QCD results [123]. Partial chemical equilibrium temperature at which the different species of particles been formed is set to below 150 MeV with the kinematic freeze out temperature at which the particles stop interacting set to 120 MeV. At the kinematic freeze out temperature, the Cooper-Frye prescription has been carried out for computing particle spectra [124].

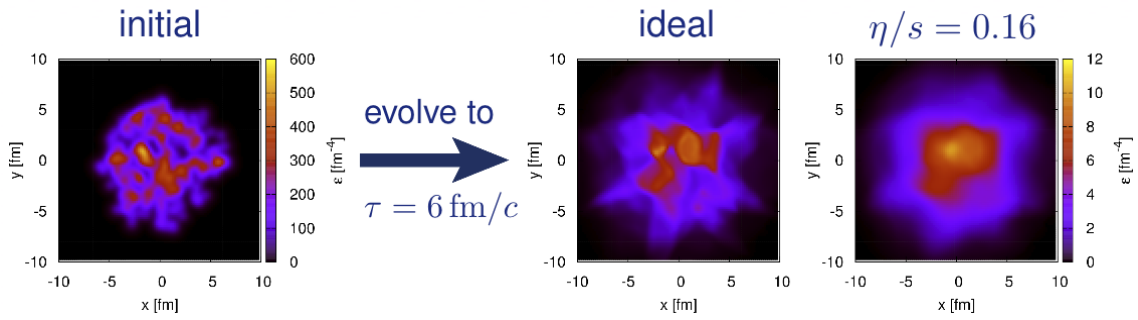

Figure 6.5: The evolution of initial energy density with and without viscous effects using the MUSIC simulation [111].

Figure 6.5 shows how the initial energy anisotropy propagates with and without viscous effects. As shown in figure 6.5, after 6 fm/c, ideal hydro evolution preserves much of the initial energy anisotropy compared to the viscous hydro evolution of the medium. A non-zero viscosity to entropy density ratio ($\eta/s \neq 0$) dampens the flow strength (the anisotropy transformation between the initial geometrical anisotropy and final state momentum space anisotropy) that is measured experimentally. Therefore the intercept value of scaling relations shown in figure 5.35 can be

used as a measure of the viscosity of the QGP medium.

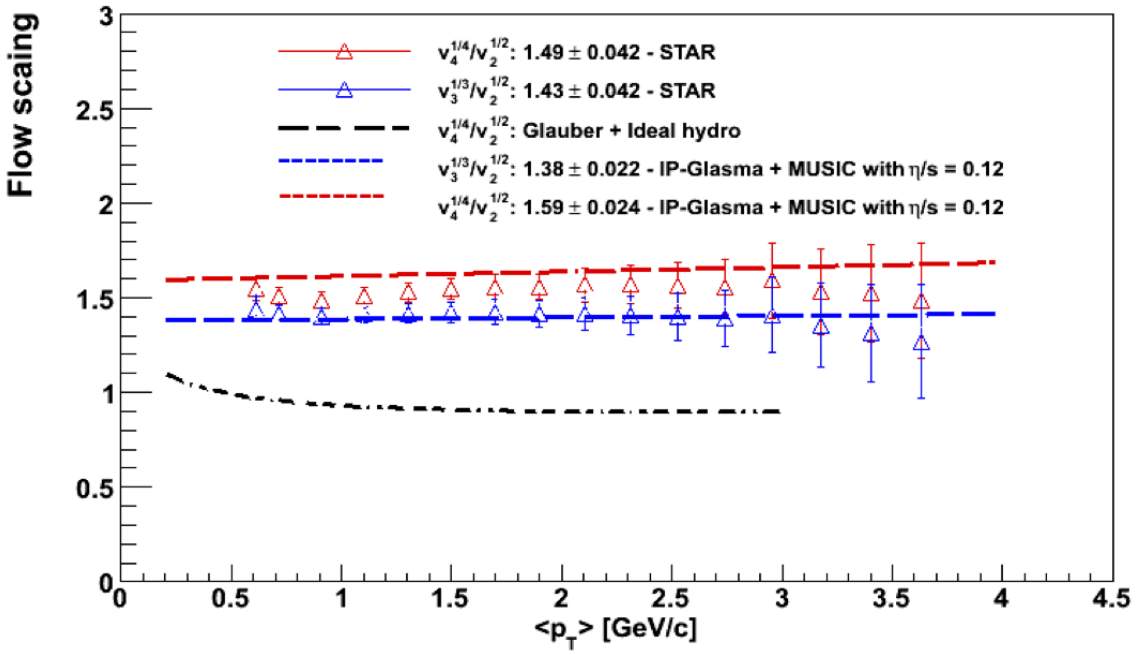

Figure 6.6: Hydro scaling relations using Au+Au 200 GeV data from STAR at 0-10% compared to IP-Glasma + MUSIC model calculations.

The figure 6.6 shows the scaling relation comparisons between data and theory. Deviations from the ideal hydro predictions are addressed based on initial state color charge fluctuations and viscous effects. The data agree with a η/s value of 0.12 which is larger than the predicted quantum limit of 0.08 [125,126] and within the predicted range 0.08 - 0.24 [127]. Additionally, shown in figure 5.31 is the summed harmonic amplitude evolution as a function of $\langle p_T \rangle$, from which we can deduce that the "ridge" correlation does not disappear at higher $\langle p_T \rangle$ rather reaches a minimum value.

6.2 Implications from the 2d Gaussian parameter evolution

The 2d Gaussian ("remainder") parameter evolution shown in figures 5.31 to 5.34 can be understood primarily via possible medium modified jet phenomena. Figures 5.31 and 5.32 show the remainder amplitude and $\Delta\eta/\Delta\phi$ width parameter behavior while figures 5.33 and 5.34 show the remainder widths compared to p + p data. It is noticeable from figure 5.32 that the widths of the remainder become symmetric above $\langle p_T \rangle \approx 2.5$ GeV/c. In the same $\langle p_T \rangle$ range, the amplitude of the remainder increases (open red symbols in figure 5.31). As discussed under figure 5.29 in section 5.4.2, the increase in the amplitude parameter in this range is understood due to sampling of collimated jet fragmentation correlation. The correlation strength in a narrow $\Delta\eta$x$\Delta\phi$ space is expected to increase as we increase the lower p_T cut. This is because a jet is a collimated distribution of partons around a leading hard scattered parton with more sub-leading partons closer in the coordinate space to the initial parton and having higher momentum compared to the ones further away from it. Therefore as a function of the lower p_T cut, the decrease in correlated pairs is less steep compared to the background pairs in this narrow $\Delta\eta$x$\Delta\phi$ region which is reflected in our correlation measure as an increase in the correlation strength (see figure 5.29). Below $\langle p_T \rangle \approx 2.5$ GeV/c, the remainder is asymmetric and more elongated in $\Delta\eta$. The amplitude of the remainder increases with decreasing $\langle p_T \rangle$ and is comparable to the summed harmonic amplitude in the $0.9 \leq \langle p_T \rangle \leq 2.1$ GeV/c range. However, as seen in figures 5.33 and 5.34 both $\Delta\eta$ and $\Delta\phi$ widths

are broader compared to the respective p + p widths and is approximately a factor of two above $\langle p_T \rangle \approx 2.5$ GeV/c. After all these observations have been taken into account, the interpretation of the remainder parameter evolution can be divided into two kinematic ranges. First we will discuss the parameters in the kinematic range below $\langle p_T \rangle \approx 2.5$ GeV/c in relation to recent theoretical developments [128,129] which relates to hydrodynamical evolution of QGP. Afterwards the kinematic range above $\langle p_T \rangle \approx 2.5$ GeV/c will be discussed in relation to medium modified jet phenomena and jet transport coefficient $\hat{q}$ in the QGP medium. Figure 6.7 shows a qualitative schematic of the remainder width modification with respect to p + p data.

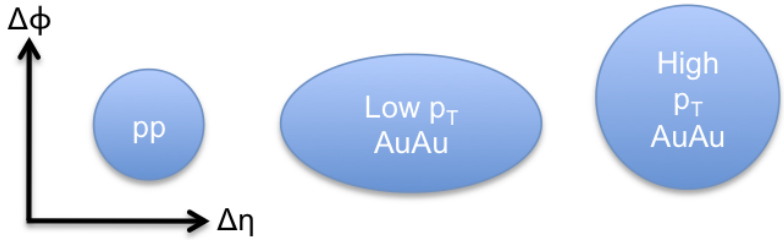

Figure 6.7: The qualitative remainder width modification with respect to p + p data at low (below $\langle p_T \rangle \approx 2.5$ GeV/c) and high (above $\langle p_T \rangle \approx 2.5$ GeV/c) p_T.

Implications below $\langle p_T \rangle \approx 2.5$ GeV/c

The three main candidates for explaining the $\Delta\eta$ elongated remainder are; modified jet phenomena [158,159], resonance production [165] and hydrodynamical phenomena. In the following, we will discuss two hydrodynamical model predictions [128,129] that reproduces qualitative trends in the data. At the present time, there are not any successful model predictions which describes the $\Delta\eta$ elongated remainder via modified jet phenomena or resonances.

The first hydrodynamical model studies the initial state fluctuation induced correlations which are localized in both transverse and longitudinal directions. Such initial state fluctuations are different to previously studied color charge fluctuations and only due to natural hydrodynamical fluctuations in the initial state which are caused by finite particle number effects which leads to local thermal fluctuations in the energy density and flow velocity in a given fluid cell [130]. A given fluid cell, which is also known as a local hot spot, is evolved using hydrodynamical equations in the flow background of the expanding medium. The fluctuations are introduced as additional stochastic terms to the energy-momentum tensor ($T^{\mu\nu}$) and current densities (J^{μ}) [130]. The correlation functions of these space-time dependent stochastic terms are then determined after evolved using fluid equations of motion. Main motivation to this study come from prior studies [131] which revealed that most of the two particle correlation features in azimuth angle difference ($\Delta\phi$) can be reproduced by the hot spots which are placed at a particular position in the transverse plane and evolved using hydrodynamics. The current study follows this work carefully and successfully includes the rapidity extension of the two particle correlation measurement. In essence, the early time (initial) microscopic space-time fluctuations are propagated via diffusion in the expanding medium and are still correlated at a macroscopic scale in the final state. Thus the long range correlation behavior in $\Delta\eta$ can be understood through natural hydrodynamical fluctuations in the initial state propagating in an expanding medium. The other important aspect of this study is that we can deduce the η/s value by an approach which is complementary to higher order harmonics.

Figure 6.8 shows the correlation function constructed in [130] with and without

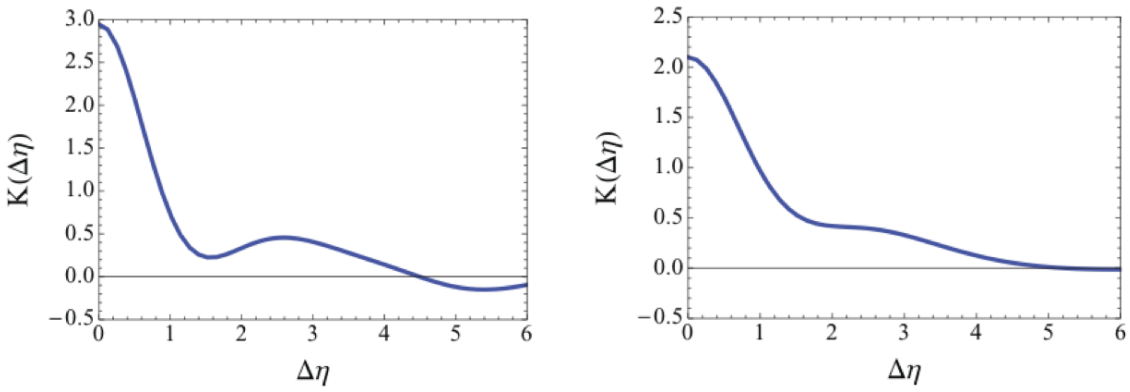

Figure 6.8: The correlation function K($\Delta\eta$) measured in $\Delta\eta$ without (left) and with (right) viscous effects in a hydrodynamical evolution [130].

viscosity effects. We observe a viscosity dependence in the $\Delta\eta$ extension of the di-hadron correlation.

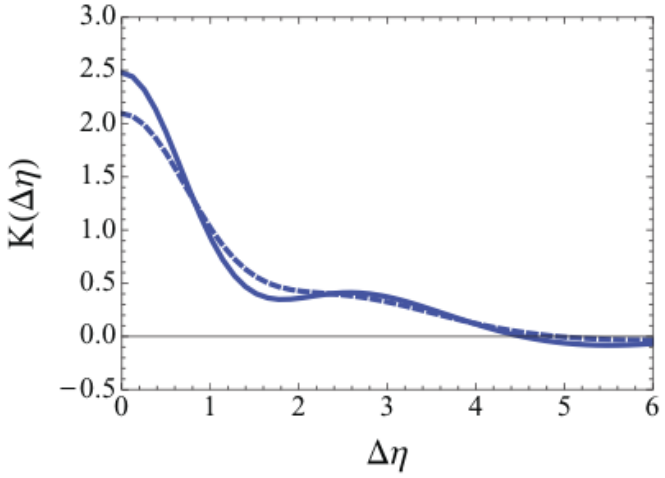

Figure 6.9: The comparison of correlation function K($\Delta\eta$) for the two viscosity values $\eta/s = 1/4\pi$ and $3/4\pi$ using solid and dashed curve respectively [130].

Figure 6.9 compares the correlation function K($\Delta\eta$) for the two η/s values $1/4\pi$ and $3/4\pi$ (0.08 - 0.24; the predicted range for η/s [127]). The calculation uses a kinematic freeze-out temperature (T_{fo}) of 150 MeV and the Cooper-Frye prescription

[124] to describe the final state particle spectra. Other important parameters used in the calculation are, the thermalization proper time ($\tau_0 = 0.5\ fm/c$) and freeze-out proper time ($\tau_{fo} = 10\ fm/c$).

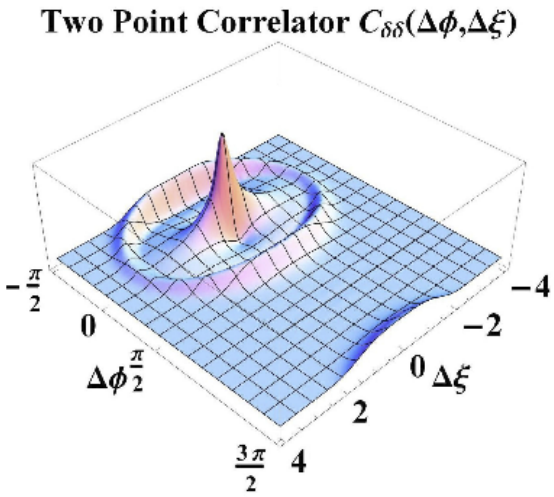

Figure 6.10: The two-particle correlation measured in $\Delta\phi$ and $\Delta\xi$ (space-time rapidity) by hydrodynamic propagation of initial state fluctuations [128].

Figure 6.10 shows the two-particle correlation structure in 2d using the above discussed hydro phenomena. Since the initial hot spots are propagated using hydrodynamics, a sound front is also evident in figure 6.10. Further improvements to this two dimensional correlation function are been carried out presently. Thus presently, we could only do a qualitative comparison with our "remainder" from which we can deduce the hydrodynamical expansion of initial state fluctuations could be a possible candidate in describing our "remainder" $\langle\ p_T \rangle$ evolution. We are currently working on getting an exact comparison to the theory.

The second hydrodynamical explanation is based on considering the effects of local

charge conservation at a late stage of evolution [129]. An event by event hydrodynamical calculation has been carried out in order to obtain the di-hadron correlation in $\Delta\eta - \Delta\phi$ with Glauber model initial conditions for transverse and longitudinal energy distributions. The prediction closely studies the previous work which shows the importance of the formation of charges at a late stage of the hydrodynamical evolution of the system [132 - 135]. Formation of such charges are argued to induce strong correlations between unlike-sign pairs in $\Delta\eta$ and $\Delta\phi$. The same mechanism has been proposed as the cause of $\Delta\eta$ dependence of the "ridge" correlation that is on top of a flow (higher order harmonic) modulation [136]. In this local charge conservation picture, the Glauber initial conditions are evolved using a 3 + 1D viscous hydrodynamical evolution with bulk and shear viscosity [137,138]. The initial entropy density is generated as coarse-grained distributions from GLISSANDO [139] with the freeze-out particle emission carried out using THERMINATOR [140]. Local charge conservation is implemented at the statistical emission stage of the THERMINATOR code with opposite charge particles are emitted in pairs from the same fluid element.

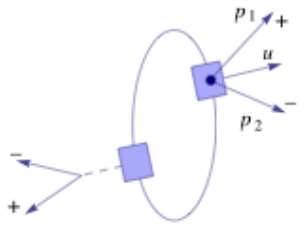

Figure 6.11: Charge conservation mechanism for resonance decay and local pair creation. u gives the collective flow velocity of the fluid cell and p_1, p_2 are the momenta of positive and negative charged particles in the pair respectively. The charged particle pair coming out from the dotted line represents resonance decay.

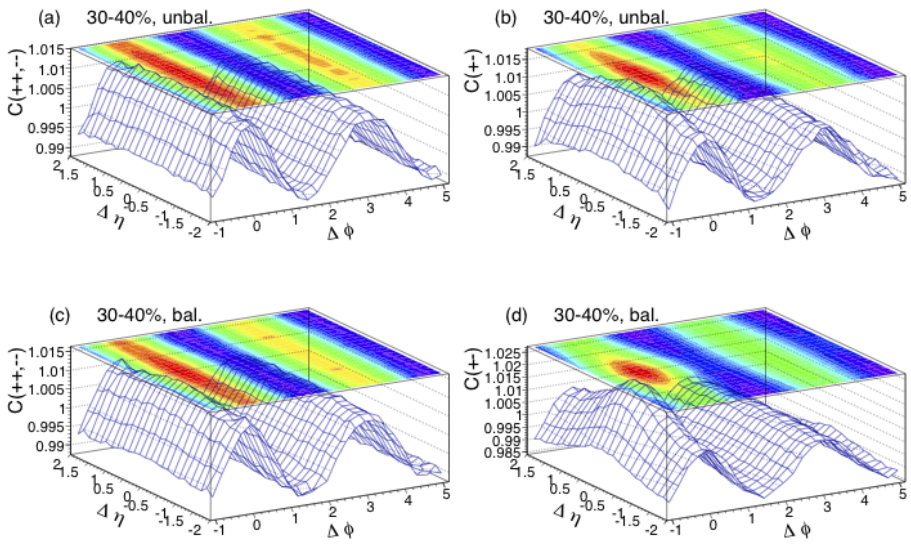

Figure 6.12: 2D correlation functions showing the local charge conservation effects. Top and bottom rows are without and with charge balancing respectively while left and right columns are for like-sign and unlike sign pairs respectively. The correlation functions are generated for 30-40% Au + Au collisions at $\sqrt{S_{NN}} = 200$ GeV and for charged particles with $0.2 < p_T < 2$ GeV with $T_{fo} = 150$ MeV.

As seen in figure 6.11, the local charge conserving charged particle pair experiences the same collective flow velocity u which collimates their motion. It is also to be noted that the calculation includes pairs from resonance decay cascades. A weak short range correlation peak can be observed in figure 6.12 top row, right panel, (unlike-sign correlation) compared to the left panel (like-sign correlation) due to resonance decay cascades. However, when local charge conservation is included (bottom row), the unlike-sign correlation measure is enhanced to give a significant peak structure compared to the like-sign measurement which is also comparable to what is observed in the experiment [141]. However, presently we can not directly compare the theory to our charge independent correlation structure since total momentum conservation need to be established in the theory. The qualitative correlation trend

shown in theory by incorporating hydrodynamical flow and local charge conservation is an indicative of possible explanation to our "remainder" with caveats been addressed in future. Furthermore, the local charge conservation theory can also be used as an independent measurement to extract the η/s value in QGP.

Implications above $\langle p_T \rangle \approx$ 2.5 GeV/c

The other extensively studied QGP property is the energy loss in the medium. We provide a novel experimental measure towards energy loss calculations by extracting the "remainder" width broadening in comparison to p + p data. The evidence we have for a factor of two broadening of the "remainder" above $\langle p_T \rangle \approx 2.5$ GeV/c could be used in energy transport coefficient($\hat{q}$) calculations in QGP. In the following we discuss in detail how our measurement could potentially deduce $\hat{q}$ in the QGP.

Under sections 1.4.2 and 1.4.3 we briefly discussed energy loss in the QGP medium using the R_{AA} measurement. In a R_{AA} measurement (see figure 1.10 and equation 1.3), the particle yield in a heavy ion collision is compared to the corresponding yield in a p + p collision as a function of p_T. If R_{AA} measures a value of one, that means in a heavy ion collision the particle yield in that p_T bin is comparable to p + p which implies that no medium effect has taken place. However figure 1.10 shows R_{AA} values less than one for central Au + Au collisions. This observation implies that the relative yield of particles at high p_T is suppressed, which is indicative of early stage partons interacting with the medium and loosing their energy to the medium. Even though in principle this interaction should increase the yield of particles ($R_{AA} > 1$) at some low p_T value with respect to p + p collisions, due to limited acceptance in

pseudo-rapidity we loose particles in STAR TPC thus influencing the R_{AA} measurement at low p_T for Au + Au collisions. However, at high p_T the pseudo-rapidity acceptance has a negligible influence since the hard scattered partons travel in the transverse direction and thus will be detected mostly at mid-rapidity. If we now consider the p_T range above 2.5 GeV/c from figure 1.10 where partonic energy loss dominates (as opposed to lower p_T where the effect is convoluted with Cronin effect and gluon shadowing), it is evident that the yields are suppressed by a factor of five. Traditionally, the energy loss mechanism in QGP medium has been divided into elastic scattering[142-144] and medium-induced gluon radiation [145-150]. Figure 6.13 shows a typical example of the different contributions to the π^0 suppression spectrum. Energy loss models compute the energy transport coefficient $\hat{q}$ in order to quantify the average energy transfer between the medium and the traversing parton. Therefore the energy transport coefficient $\hat{q}$ is also known as the jet energy transport coefficient.

The equations 6.4 and 6.5 describe the radiative energy loss using GLV [153] and BDMPS [152] descriptions respectively.

$$\Delta E_{GLV} \propto \alpha_s^3 C_R \frac{1}{A_\perp} \frac{dN^g}{dy} L \tag{6.4}$$

$$\langle \Delta E \rangle_{BDMPS} \propto \alpha_s C_R \langle \hat{q} \rangle L^2 \tag{6.5}$$

Here, α_s is the strong coupling constant, $\frac{dN^g}{dy}$ is the gluon density per unit rapidity, $A_\perp$ is the transverse area, C_R is the Casimir operator and L is the path length of a parton in the QGP medium. In BDMPS model, the energy loss is characterized by

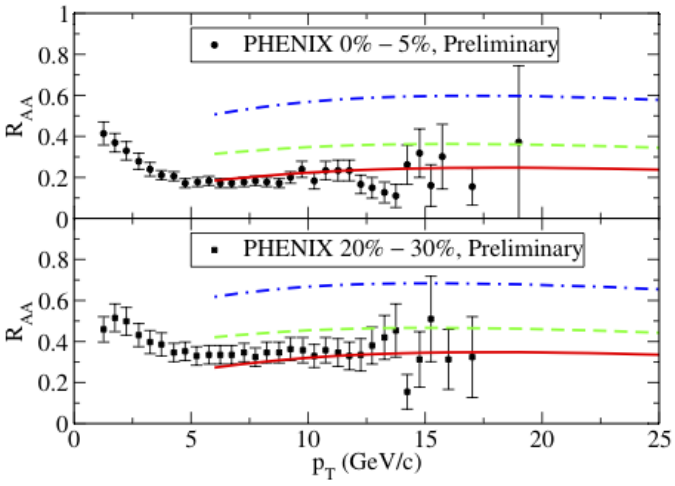

Figure 6.13: Neutral pion suppression factor in central and mid-central 200 GeV Au + Au collisions from PHENIX collaboration compared to theory calculations. Here the dashed dotted curve represents collisional, dashed curve represents radiative and solid curve represents both energy loss mechanisms taken into consideration [151].

the jet transport coefficient $\hat{q}$ where as GLV model considers the initial gluon density $\frac{dN^g}{dy}$. Defining $\hat{q}$ formally requires the number density density ρ of the constituents in the medium (partons). A more formal definition can be written as,

$$\hat{q} = \rho \int d^2q_\perp q_\perp^2 \frac{d\sigma}{d^2q_\perp} \tag{6.6}$$

where $q_\perp$ is the transverse momentum transfer (in the x-y plane) and $\frac{d\sigma}{d^2q_\perp}$ is the differential scattering cross section of the parton in the medium.

Figure 6.14 shows a schematic of a hard scattered parton traversing the QGP formed in a heavy ion collision. The parton shower of the jet on top of the schematic does not interact with the medium if it is emitted from the surface of the QGP. However, if a jet is formed inside the QGP, it vastly complicates the dynamics of

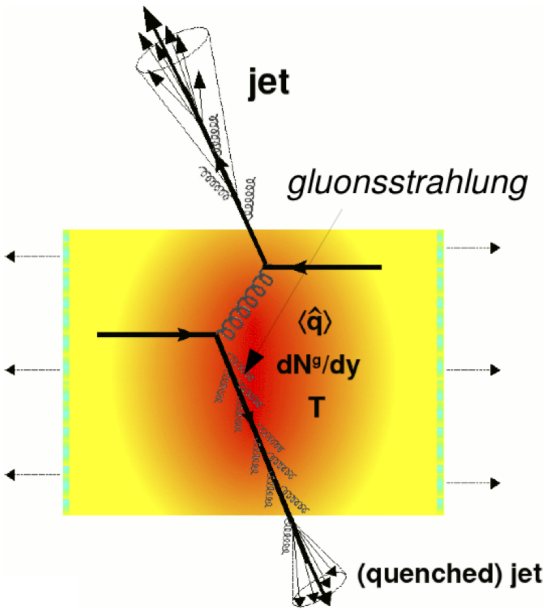

Figure 6.14: A schematic of radiative energy loss in a hard scattered jet. Some of the the relevant physical quantities which drives the energy loss, T, $\hat{q}$ and gluon density are notified [David d'Enterria (MIT)].

the QGP and jets. The jets which interacted with the medium as such are called quenched jets and our measurement indicates a broadening of quenched jets with

respect to unmodified jets in p + p collisions where a QGP is not formed. The model computations shown in figures 6.15 and 6.16 successfully address the observed R_{AA} measurements but they do not converge to a common $\hat{q}$ value. The GLV calculation gives a range for $\hat{q}$ that is 0.35 - 0.85 GeV^2/fm for $dN^g/dy = 900$ with the corresponding BDMPS value at 5 GeV^2/fm. In fact due to many theoretical uncertainties, $\hat{q}$ ranges from 0.3 - 20 GeV^2/fm [155-157]. We propose our measurement, namely the width comparison between the Au + Au remainder and p + p, in order to better extract $\hat{q}$ for the QGP. However this requires theoretical descriptions [158-160] using jet shape modification at high p_T in heavy ion collisions. In the following we will

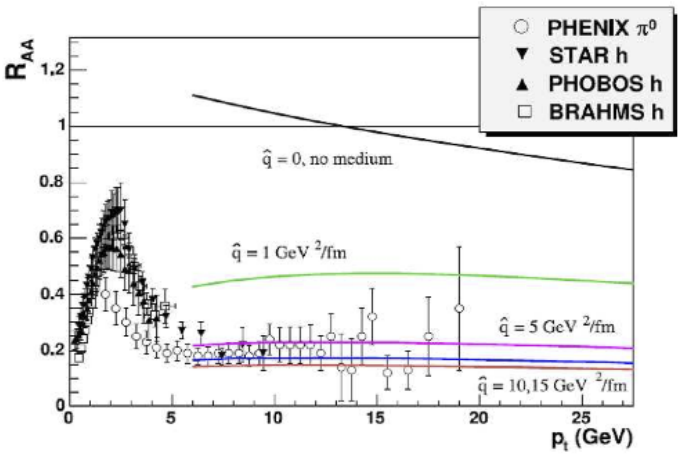

Figure 6.15: BDMPS models fits to the π^0 and charged hadron R_{AA} as a function of $\hat{q}$. A $\hat{q}$ value of 5 GeV^2/fm corresponds to a $\frac{dN^g}{dy}$ of 900.

discuss two model studies which are of great relevance to our suggested measurement.

The previously discussed GLV model has been extended [158,159] in order to describe the jet shape modification. The R_{AA} measurements for jets in [158] are indicative of a factor of two modification of the jet widths in heavy ion collisions. R_{AA} calculations using a fixed jet cone radius 0.4 are shown in figure 6.17. The calculations are carried out using a minimum parton energy of 0 GeV for Pb+Pb collisions at LHC for three different centralities which are characterized by the impact parameter b. For comparison purposes with STAR, we focus on the relevant total transverse jet energy $E_T \approx 30$ GeV. At this total jet energy, we can deduce that the R_{AA} value is roughly a factor of two suppressed in central collisions ($\approx 0.7/0.35$). From figure 6.18 top panel we can see that by approximately doubling the cone radius 0.4 (symmetric broadening of the width), a comparable value to the peripheral suppression factor

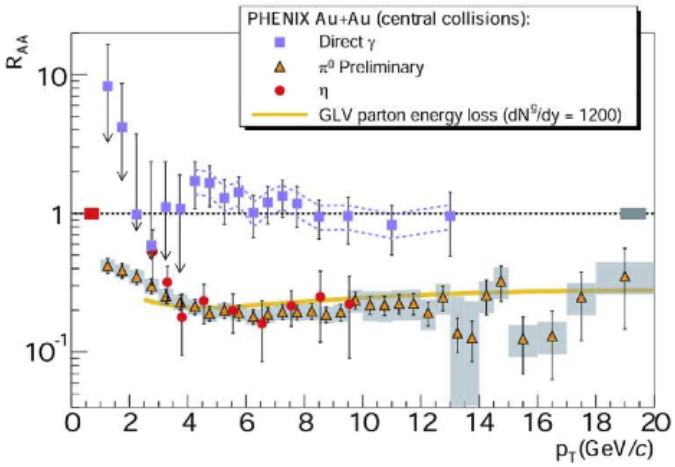

Figure 6.16: GLV model comparison to π^0 R_{AA} for central Au + Au 200 GeV data from PHENIX. R_{AA} for η and direct γ is also shown without model comparisons.

(0.7) can be achieved. Thus a symmetrically broaden jet by an approximately a factor of two in comparison to p + p collisions could be expected in central heavy ion data at $E_T \approx 30$ GeV. The bottom panel indicates that with increasing minimum energy cut off the R_{AA} decreases. The minimum cut off value needs to be at $p_T > 2.3$ GeV/c in order to compare with our experimental values. Finally, figure 6.19 shows the differential jet shape expectations in vacuum and medium using GLV model for STAR energies. We observe a much greater radius value r for the jets traversing a medium as one would expect. Currently we are discussing with the theorists to obtain more qualitative estimates for the differential jet shapes in order to compare to our experimental values. Ultimately we expect to estimate the jet energy transport coefficient $\hat{q}$ of the QGP via the corresponding $\frac{dN^g}{dy}$ values from the GLV model.

Next, we briefly discuss the second model study in [160] which uses an extension

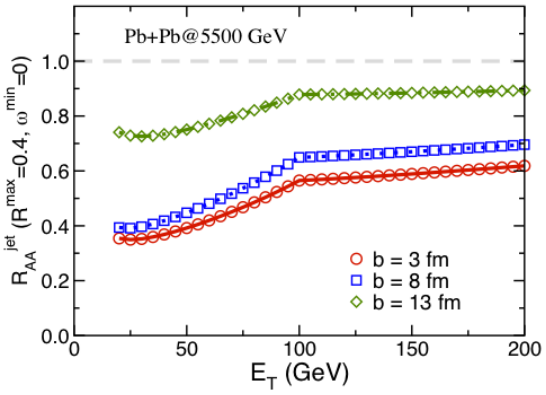

Figure 6.17: Nuclear modification factor as a function of total transverse jet energy E_T for three centralities in Pb + Pb collisions at a fixed jet cone radius of 0.4 and a minimum parton energy of 0 GeV. Impact parameter b=13 and b=3 corresponds to peripheral collisions (p + p reference) and central (0-10%) Pb + Pb collisions respectively [158].

of the BDMPS energy loss model in order to extract $\hat{q}$ of the QGP. Figure 6.20 illustrates the mechanism which is implemented in the model in order to calculate jet broadening and corresponding energy loss. As seen in figure 6.20, the collective flow fields in the medium could impose characteristic modifications to the high p_T parton fragmentation. The parton energy loss mechanism is expanded by considering flow induced, oriented momentum transfer. Asymmetric multiplicity and energy distributions for jets in $\eta - \phi$ plane have been calculated and shown in figure 6.21. The basic idea behind the calculation is to deduce the gluon energy distribution that results from fragmenting the initial scattered parton and couple the momentum transfer to flow fields in the medium. An example calculation has been carried out using, a total transverse jet energy of E_T=100 GeV, a path length L of 6 fm, a momentum transfer per scattering center μ of 1 GeV/c, a collective flow effected momentum transfer q_0 of 1 GeV/c, a jet cone radius of 0.3 and the strong coupling of α_s=1/3. It is also

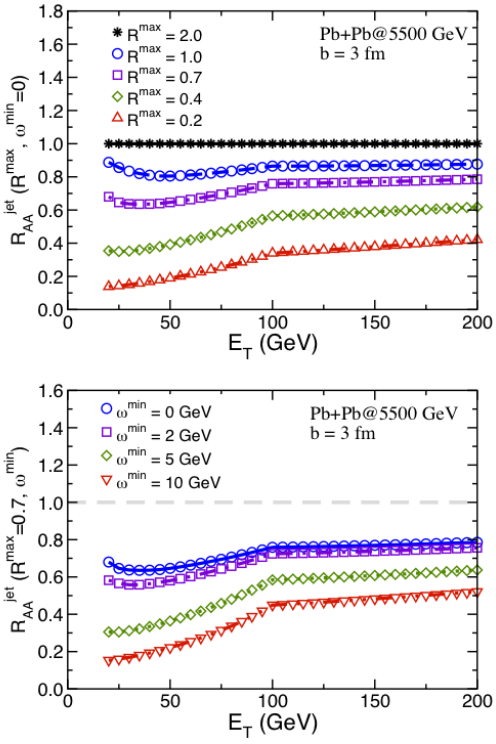

Figure 6.18: Nuclear modification factor as a function of E_T for central Pb + Pb collisions. Top: Varying the jet cone radius at a fixed minimum parton energy 0 GeV. Bottom: Varying the minimum parton energy at a fixed jet cone radius 0.7.

shown that in general the reconstructed jet axis (the symmetry axis of the jet cone) gets shifted in the direction of the flow field. However, we are interested in looking at the multiplicity distribution of the fragmented the initial parton which is shown in figure 6.21. The effects seen in the multiplicity distributions are as expected from the model prediction. For both $\alpha^{'}$=0 and $\pi/4$ cases, the observed negative multiplicity yield is due to the interaction between jet fragments and flow fields in the strongly coupled medium. It is discussed in the model that the long tails give rise to elongation in $\Delta\eta$ correlation. Also the $\alpha^{'}$=0 case gives a slightly higher yield as compared to the $\alpha^{'}=\pi/4$ case. It is also evident that as one increases the lower

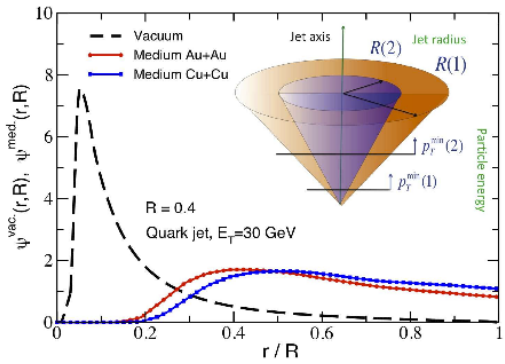

Figure 6.19: The differential jet shape calculation in vacuum and medium (Cu + Cu and Au + Au) at 200 GeV for STAR. A fixed jet cone radius of 0.4 and E_T of 30 GeV has been used [159].

p_T/energy cut off for the partons, the yield closer to the jet axis slightly reduces. For the $\alpha^{'}=\pi/2$ case, the multiplicity distribution is symmetric as one would expect due to a much smaller influence from the medium interaction. In order to extract the $\hat{q}$ value of the QGP, the modified gluon distribution information is coupled to the BDMPS jet energy transport coefficient formula using the new formalism adopted in the prediction. It seems that this effect could not only explain the broadening at high p_T but also the anisotropy ($\Delta\eta$ elongation) of the remainder at lower p_T.
In order to compare to the experimental measure, though, the prediction needs to evaluate the jet multiplicity distribution using the relevant kinematic cuts and reproduce the appropriate jet shape. After producing the jet multiplicity distribution the corresponding gluon energy distribution can be used in the modified BDMPS formalism to extract the QGP jet energy transport coefficient $\hat{q}$.

In summary, we were able to map and expand the kinematic boundaries that have been studied in previous triggered di-hadron correlation analyses in the 0-10%

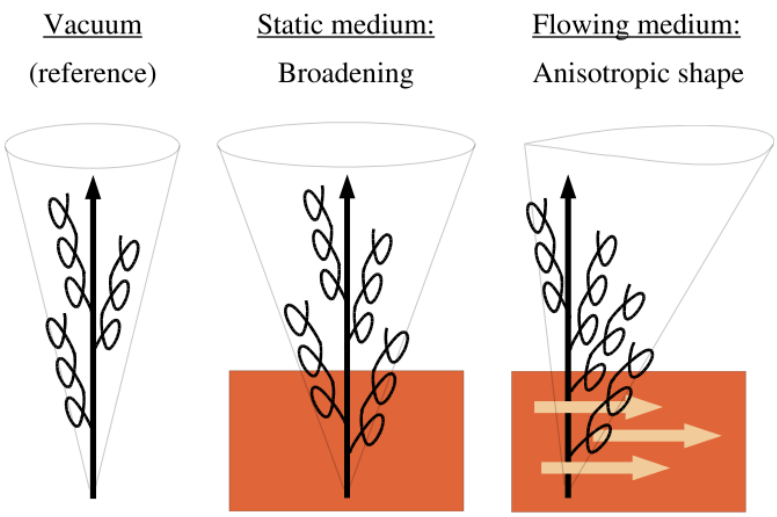

Figure 6.20: A schematic of a jet traversing a). in vacuum b). in a medium which is comoving with the jet's rest frame c). in a medium which is boosted perpendicularly to the rest frame of the jet. The distribution of radiated parton multiplicity under the influence of a comoving QGP medium is shown.

centrality bin using Au+Au 200 GeV data from the STAR experiment. We found a smooth evolution of di-hadron correlation structures as a function of $\langle p_T \rangle$ and reproduced the high p_T structure from a $\langle p_T \rangle$ value of approximately 2.3 GeV/c on. For the first time, the near side correlation structure was modeled using a Fourier series that consist of terms up to n=5 and a 2d Gaussian structure to model the remaining structure after subtracting out the summed Fourier series contribution. The Fourier series terms extract possible initial state energy density fluctuation correlation contributions in heavy ion collisions. We studied the Fourier series terms n$\geq$2 by comparing to an independent analysis from the STAR experiment, based on single particle measurements with respect to the reaction plane, and observed excellent agreement. Then we focused on characterizing medium properties of the QGP by extracting a value for the shear viscosity (eta/s). Our results are consistent

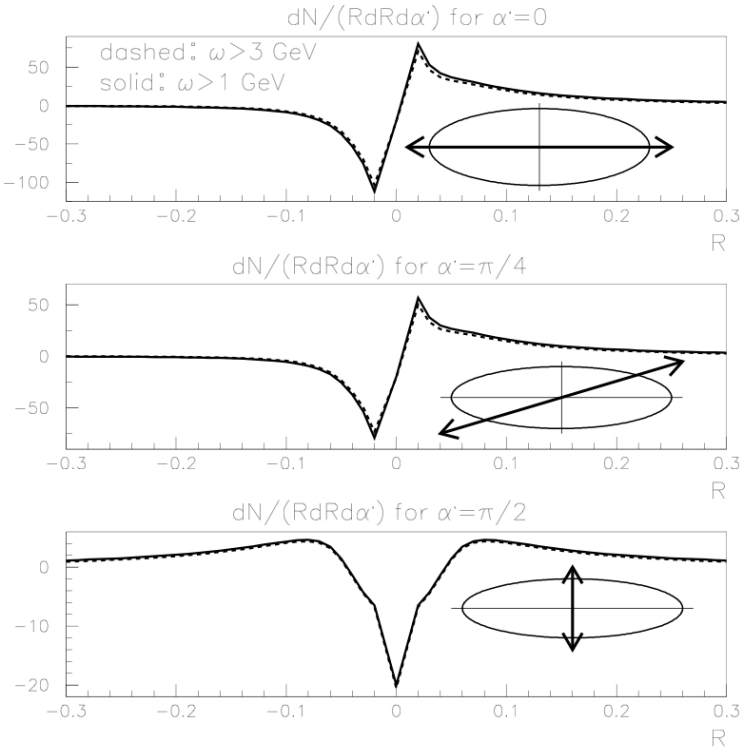

Figure 6.21: The jet multiplicity distribution for different cuts in $\eta - \phi$ plane for two low momentum cut off values, $w > 3$ GeV/c and 1 GeV/c. The flow field acts in the direction of the beam line.

with a hydrodynamics based model that uses an eta/s value of 0.12, which is within the anticipated range (0.08 024) for a near perfect liquid close to the quantum limit. The summed higher order terms indicate the long-range correlation strength reaches a minimum at high p_T but might not fully disappear.

For the second part of our analysis we focused on the remainder in two distinct kinematic regions in $\langle\ p_T \rangle$. The region below $\langle\ p_T \rangle \approx 2.5$ GeV/c was discussed in relation to two possible scenarios that use hydro-dynamical description of QGP. Indications are that the asymmetry in the remainder can be attributed to either

initial conditions pushed by bulk flow or jets deflected in the bulk medium. We are currently working on obtaining exact predictions for our kinematic selections from the theory groups in order to compare the remainder width parameters. The region above $\langle\, p_T \rangle \approx 2.5$ GeV/c clearly indicates evidence for symmetric (in angular space) jet broadening. Again, we are anticipating quantitative input from theory to our width measurements in order to estimate the jet transport coefficient in QGP. The sum of the extracted medium properties can be tested against any theory that derives the relation between eta/s and jet energy transport coefficient.

Bibliography

[1] Bohr, Henrik and H.B Nielsen, Nuclear Physics B 128, 275 (1977)

[2] http://www.particleadventure.org

[3] G. Steigman, Ann. Rev. Nucl. Part. Phys. 57, 463 (2007)

[4] M. Harrison, T. Ludlum, S. Ozaki, Nuclear Instruments and Methods in Physics Research A 499, 235 (2003)

[5] D. Scott, arXiv:astro-ph/0510731 (2005)

[6] Coles, P (2001). *Routledge Critical Dictionary of the New Cosmology*. Routledge, London

[7] E. Komatsu et.al., Astrophysical Journal Supplement 180, 330 (2009)

[8] E. Menegoni et.al., Physical Review D 80, 087302 (2009)

[9] Edward W. K. and Michael S. T. (1994). *The Early Universe*, p. 447. Westview press, New York, New York

[10] D. Samtleben et.al, Ann. Rev. Nucl. Part. Sci. 57, 245 (2007)

[11] J.D. Bjorken, FERMILAB-Pub-82/59-THY

[12] M. Gyulassy and M. Plumer, Phys. Lett. B 243, 432 (1990); R. Baier et al., Phys. Lett. B 345, 277 (1995)

[13] R. Baier, D. Schiff and B.G. Zakharov, Annu. Rev. Nucl. Part. Sci. B 50, 37 (2000)

[14] X. N. Wang and M. Gyulassy, Phys. Rev. Lett. 68, 1480 (1992); X. N. Wang, Phys. Rev. C 58, 2321 (1998)

[15] E. Wang and X. N. Wang, Phys. Rev. Lett. 89, 162301 (2002); F. Arleo, Phys. Lett. B 532, 231 (2002)

[16] STAR, J. Adams et al., arXiv:nucl-ex/0306024 (2003)

[17] W. Cassing, K. Gallmeister and C. Greiner, arXiv:hep-ph/0311358 (2003)

[18] Cronin et al., Phys. Rev. D 11, 3105 (1975)

[19] Peter Jacobs, Eur. Phys. J. C 43, 467 (2005)

[20] STAR, J. Adams et al., arXiv:nucl-ex/0501016 (2005)

[21] N. Borghini, P.M. Dinh and J.-Y. Ollitrault, Phys. Rev. C 62, 034902 (2000)

[22] STAR, J. Adams et al., arXiv:nucl-ex/0411003 (2004)

[23] J. D Bjorken, Phys. Rev. D 27, 140 (1983)

[24] B. Tomasik, U.A. Wiedemann and U. Heinz, CERN report TH-215 (1999), arXiv:nucl- th/9907096 (1999)

[25] Peter Jacobs, eConf. C020805, TTH05 (2002)

[26] A. Franz, et al., Nucl. Instrum. Methods A 566, 54 (2006)

[27] R. Middleton, Nuclear Instruments and Methods 214, 139 (1983)

[28] S. Zhang and L. Ahrens. Booster gold beam injector efficincy and beam loss. In S. Myers et al, editor, EPAC 98: Sixth European Particle Accelerator Conference, p. 2149-2151. AIP Conference Proceedings New York, American Institute of Physics (1998)

[29] H. Hahn et al., Nucl. Instrum. Meth. A 499, 245 (2003)

[30] Cegpa, "Brookhavens Linear Accelerator", Brookhaven National Laboratory, May 15, (2003). http://www.bnl.gov/bnlweb/facilities/LINAC.html

[31] Cegpa, "Alternating Gradient Synchrotron", Brookhaven National Laboratory, May 15, (2003). http://www.bnl.gov/bnlweb/facilities/AGS.html

[32] H. Hahn et al., Nucl. Instrum. Meth. A 499, 245 (2003)

[33] RHIC Design Manual (1990-2000), http://www.agsrhichome.bnl.gov/AGS/Accel/Reports

[34] J. H. Lee, Notes from Workshop on Thermalization and Chemical Equilibration in Heavy Ions Collisions at RHIC, BNL (2001)

[35] B. B. Back et al., Nucl. Instrum. Meth. A 499, 603 (2003)

[36] STAR, K. H. Ackermann et al., Nucl. Instrum. Meth. A 499, 624 (2003)

[37] H. S. Matis, R. L. Brown, W. Christie, W. R. Edwards, R. Jared, B. Minor and P. Salz, Nucl. Instrum. Meth. A 499, 802 (2003)

[38] STAR, D. Reichhold et al., Nucl. Instrum. Meth. A 499, 792 (2003)

[39] STAR, F. Bergsma et al., Nucl. Instrum. Meth. A 499, 633 (2003)

[40] F. S. Bieser et al., Nucl. Instrum. Methods A 499, 766 (2003)

[41] STAR, C. Adler et al., Nucl. Instrum. Meth. A 499, 778 (2003)

[42] STAR trigger public page: www.star.bnl.gov/public/trg/

[43] L.V. Gribov, E.M. Levin, and M.G. Ryskin, Phys. Rept. 100, 1 (1983)

[44] A.H. Mueller and J.W. Qiu, Nucl. Phys. B 268, 847 (1986)

[45] LBL online archive: http://www.lbl.gov/Science-Articles/Archive/star/

[46] Particle Data Group. Eur. Phys. J. C15, 1 (2000)

[47] F. Sauli, Technical Report CERN 77-09, CERN (1977)

[48] M. Anderson et.al., Nucl. Instrum. Meth. A 499, 659 (2003)

[49] New State of Matter created at CERN, www.info.web.cern.ch/Press/PressReleases/Releases2000/PR01.00EQuarkGluonMatter.html

[50] M. Stephanov, K. Rajagopal, E. Shuryak, Phys. Rev. D 60 114028 (1999)

[51] STAR, J. Adams et al., Phys. Rev. C 71, 064906 (2005)

[52] STAR, J. Adams et al., J. Phys. G 32, 37 (2006)

[53] K. Pearson, Phil. Trans. Royal Soc. 187, 253 (1896)

[54] T. A. Trainor, R. J. Porter, D. J. Prindle, J. Phys. G 31, 809 (2005)

[55] T. A. Trainor and D. T. Kettler, arXiv:hep-ph/0704.1674 (2007)

[56] A. Einstein, Ann. Phys. 17, 549 (1905)

[57] D. J. Prindle and T. A. Trainor, J. of Phys. Conf. Ser. 27, 118 (2005)

[58] Daugherity, MS (2008), 'Two Particle Correlations in Ultra Relativistic Heavy Ion Collisions: A study of new state of matter created at RHIC', PhD thesis, University of Texas at Austin, Austin, Texas, USA

[59] M. Miller et al., Ann. Rev. Nucl. Part. Sci. 57, 205 (2007)

[60] R. L. Ray and M. Daugherity, arXiv:nucl-ex/0702039 (2007)

[61] S. Voloshin and Y. Zhang, Z. Phys. C 70, 665 (1996)

[62] Michael L. Miller et al., Ann. Rev. Nucl. Part. Sci. 57, 205 (2007)

[63] Derek Teaney and Li Yan, Phys. Rev. C 83, 064904 (2011)

[64] M. Luzum and J.-Y. Ollitrault, Phys. Rev. Lett. 106, 102301 (2011)

[65] M. Luzum and J.-Y. Ollitrault et al., Phys. Rev. C 83, 064901 (2011)

[66] M. Luzum and J.-Y. Ollitrault et al., Phys. Rev. Lett. 108, 252302 (2012)

[67] S. Mohapatra et al., arXiv:nucl-th/1203.3410v1 (2012)

[68] ATLAS, G. Aad et al., Phys. Rev. C 86, 014907 (2012)

[69] B. Andersson, et al., Phys. Rep. 97, 31 (1983)

[70] M. Lisa et al., Ann. Rev. Nucl. Part. Sci 55, 357 (2005)

[71] Guo-Liang Ma and Xin-Nian Wang, Phys. Rev. Lett. 106, 162301 (2011)

[72] B. Alver and G. Roland, Phys. Rev. C 81, 054905 (2010)

[73] B. Schenke, S. Jeon, C. Gale, arXiv:hep-ph/1009.3244 (2010)

[74] Rene Brun and Fons Rademakers, Nucl. Inst. and Methods A 389, 81 (1997)

[75] Ishihara, A (2004), 'Large Scale Two Particle Correlation Structures in Au + Au Collisions at $\sqrt{S_{NN}} = 130GeV$: A study of new state of matter created at RHIC', PhD thesis, University of Texas at Austin

[76] Peter Jacobs, Eur. Phys. J. C 43, 467 (2005)

[77] Joern Putschke et.al., J. Phys. G 34, S679 (2007)

[78] D. Magestro, talk given at Hard Probes (2004)

[79] L. Ray and M. Daugherity, J. Phys. G: Nucl. Part. Phys. 35, 125106 (2008)

[80] R. J. Porter and T. A. Trainor, J. of Phys. Conf. Ser. 27, 98 (2005)

[81] M. Lisa, et al., Ann. Rev. Nucl. Part. Sci. 55, 357 (2005)

[82] T. A. Trainor and D. T. Kettler, arXiv:hep-ph/0704.1674 (2007)

[83] T. Ludlam and L. McLerran, What have we learned from the Relativistic Heavy Ion Collider?, Phys. Today 56N10, 48 (2003)

[84] L. McLerran, arXiv:hep-ph/0804.1736 (2008)

[85] L. V. Gribov, E. M. Levin, and M. G. Ryskin, Phys. Rept. 100, 1(1983)

[86] A. H. Mueller and J.-w. Qiu, Nucl. Phys. B 268, 427 (1986)

[87] J. P. Blaizot and A. H. Mueller, Nucl. Phys. B 289, 847 (1987)

[88] L. D. McLerran and R. Venugopalan, Phys. Rev. D 49, 2233 (1994); arXiv:hep-ph/9309289 (1993)

[89] L. D. McLerran and R. Venugopalan, Phys. Rev. D 49, 3352 (1994); arXiv:hep-ph/9311205 (1993)

[90] Moschelli, G (2010), 'Two Particle Correlations and The Ridge in Relativistic Heavy Ion Collisions: A study of new state of QCD matter', PhD thesis, Wayne State University

[91] L. McLerran, Prog. Theor. Phys. Suppl. 187, 17 (2011)

[92] G. Moschelli and S. Gavin, arXiv:nucl-th/0910.3590 (2009)

[93] G. Moschelli, S. Gavin and L. McLerran, arXiv:nucl-th/0806.4718 (2008)

[94] L. C. De Silva, arXiv:nucl-ex/0910.5938 (2009)

[95] E. Schnedermann, J. Sollfrank and U. W. Heinz, Phys. Rev. C 48, 2462 (1993)

[96] STAR, A. Iordanova, O. Barannikova and R. S. Hollis, Int. J. Mod. Phys. E 16, 1800 (2007)

[97] F. Retiere and M. A. Lisa, Phys. Rev. C 70, 044907 (2004)

[98] L. C. De Silva, arXiv:nucl-ex/1112.1111v1 (2011)

[99] L.C. De Silva, arXiv:nucl-ex/1209.4941 (2012)

[100] C. Gombeaud et al., Phys. Rev. C 81, 014901 (2010)

[101] STAR, Y. Pandit, arXiv:nucl-ex/1210.5315 (2012)

[102] A. M. Poskanzer and S. A. Voloshin, Phys. Rev. C 58, 1671 (1998)

[103] STAR, C. Adler et al., Phys. Rev. C 66, 034904 (2002)

[104] B. Schenke and P. Tribedy et.al, Phys. ReV. Lett. 108, 252301 (2012)

[105] B. Schenke and P. Tribedy et.al, arXiv:nucl-th/1209.6330 (2012)

[106] N. Borghini and J. Y. Ollitrault, Phys. Lett. B 642, 227 (2006)

[107] STAR, J. Adams et al., Phys. Rev. Lett. 92, 062301 (2004)

[108] PHENIX, H. Masui, Nucl. Phys. A 774, 511 (2006)

[109] STAR, B. I. Abelev et al., Phys. Rev. C 75, 054906 (2007)

[110] PHENIX, S. Huang, J. Phys. G 35, 104 (2008)

[111] B. Schenke, Quark Matter 2012, Washington, DC

[112] J. Bartels, K. J. Golec-Biernat, and H. Kowalski, Phys. Rev. D 66, 014001 (2002)

[113] H. Kowalski and D. Teaney, Phys. Rev. D 68, 114005 (2003)

[114] A. Kovner, L. D. McLerran, and H. Weigert, Phys. Rev. D 52, 6231 (1995)

[115] Y. V. Kovchegov and D. H. Rischke, Phys. Rev. C 56, 1084 (1997)

[116] A. Krasnitz and R. Venugopalan, Nucl. Phys. B 557, 237 (1999); Phys. Rev. Lett. 84, 4309 (2000); 86, 1717 (2001)

[117] T. Lappi, Phys. Rev. C 67, 054903 (2003)

[118] B. Schenke, P. Tribedy, and R. Venugopalan, Phys. Rev. C 86, 034908 (2012)

[119] B. Schenke, S. Jeon, and C. Gale, Phys. Rev. C 82, 014903 (2010)

[120] B. Schenke, S. Jeon, and C. Gale, Phys. Rev. Lett. 106, 042301 (2011)

[121] B. Schenke, S. Jeon, and C. Gale, Phys. Lett. B 702, 59 (2011)

[122] B. Schenke, S. Jeon, and C. Gale, Phys. Rev. C 85, 024901 (2011)

[123] P. Huovinen and P. Petreczky, Nucl. Phys. A 837, 26 (2010)

[124] F. Cooper and G. Frye, Phys. Rev. D 10, 186 (1974)

[125] G. Policastro, D. T. Son and A. O. Starinets, Phys. Rev. Lett. 87, 081601 (2001)

[126] P. Kovtun, D. T. Son, and A. O. Starinets, Phys. Rev. Lett. 94, 111601 (2005)

[127] M. Luzum and P. Romatschke, Phys. Rev. C 78, 034915 (2008)

[128] Todd Springer and Mikhail Stephanov, arXiv:nucl-th/1210.5179v1 (2012)

[129] Piotr Bozek and Wojciech Broniowski, arXiv:nucl-th/1210.4315v1 (2012)

[130] J. Kapusta, B.Muller and M. Stephanov, Phys. Rev. C 85, 054906 (2012)

[131] P. Staig and E. Shuryak, Phys. Rev. C 84, 044912 (2011)

[132] S. A. Bass, P. Danielewicz, S. Pratt, Phys. Rev. Lett. 85, 2689 (2000)

[133] S. Jeon, S. Pratt, Phys. Rev. C 65, 044902 (2002)

[134] P. Bozek, Phys. Lett. B 609, 247 (2005)

[135] M. M. Aggarwal, et al., Phys. Rev. C 82, 024905 (2010)

[136] P. Bozek, W. Broniowski, Phys. Rev. Lett. 109, 062301 (2012)

[137] P. Bozek, Phys. Rev. C 85, 034901 (2012)

[138] P. Bozek, Phys. Rev. C 81, 034909 (2010)

[139] W. Broniowski, M. Rybczynski, P. Bozek, Comput. Phys. Commun. 180, 69 (2009)

[140] M. Chojnacki, A. Kisiel, W. Florkowski, W. Broniowski, Comput. Phys. Commun. 183, 746 (2012)

[141] G. Agakishiev, et al., arXiv:nucl-ex/1109.4380 (2011)

[142] J. D. Bjorken, Fermilab preprint Pub-82/59-THY (1982)

[143] E. Braaten and M. H. Thoma, Phys. Rev. D 44, 2625 (1991)

[144] S. Peigné and A. Peshier, Phys. Rev. D 77, 114017 (2008)

[145] M. Gyulassy and X.-N. Wang, Nucl. Phys. B 420, 583 (1994)

[146] R. Baier, Y. L. Dokshitzer, A. H. M'uller, S. Peigné, and D. Schiff, Nucl. Phys. B 483, 291 (1997); ibid. 484, 265 (1997)

[147] M. Gyulassy, P. Levai, and I. Vitev, Phys. Rev. Lett. 85, 5535 (2000); Nucl. Phys. B 571, 197 (2000); ibid. 594, 371 (2001)

[148] P. B. Arnold, G. D. Moore, and L. G. Yaffe, JHEP 0011, 001 (2003); ibid. 0305, 051 (2003)

[149] N. Armesto, C. A. Salgado, and U. A. Wiedemann, Phys. Rev. D 69, 114003 (2004); Phys. Rev. C 72, 064910 (2005)

[150] B. G. Zakharov, JETP Lett. 63, 952 (1996); ibid. 64, 781 (1996); ibid. 65, 615 (1997); ibid. 73, 49 (2001); ibid. 78, 759 (2003)

[151] G. Qin et al., Phys. Rev. Lett. 100, 072301 (2008)

[152] Eskola, Honkanen, Salgado and Weidemann, Nucl. Phys. A 747, 511 (2005)

[153] M. Gyulassy, P. Levai and I. Vitev, Phys. Lett. B 594, 371 (2001)

[154] J. Lajoie, Braz. J. Phys. vol. 37, no. 2C, June (2007)

[155] F. Arleo, JHEP 0211, 044 (2002)

[156] K. J. Eskola, H. Honkanen, C. A. Salgado and U. A. Wiedemann, Nucl. Phys. A 747, 511 (2005)

[157] R. Baier and D. Schiff, JHEP 0609, 059 (2006)

[158] I. Vitev et al., JHEP 0811, 093 (2008)

[159] I. Vitev et al., Phys. Rev. Lett. 104, 132001(2010)

[160] Nstor Armesto et al., Phys. Rev. C 72, 064910 (2005)

[161] A. Majumder et al., Phys. Rev. Lett. 99, 192301 (2007)

[162] H.-U. Bengtsson, Computer Physics Commun. 31, 323 (1984)

[163] N. Borgini, PoSLHC07, 013 (2007)

[164] S. Hands, Contemp. Phys. 42, 209 (2001)

[165] E. Oset et al., Eur. Phys. J. A 44, 431 (2010)

[166] The Hebrew University of Jerusalem:
http://www.phys.huji.ac.il/˜paul/files/eras_of_universe.jpg

[167] DashLB: http://zewex.blogspot.com/2010/09/doppler-effect.html

[168] RIKEN BNL: http://www.riken.jp/engn/r-world/info/release/news/2003/aug/index.html

[169] Feng, A (2008), 'Di-hadron Azimuthal Correlations Relative to Reaction Plane in Au + Au Collisions at $\sqrt{S_{NN}} = 200$ GeV', PhD thesis, Central China Normal University, Wuhan, CHINA

[170] Berger, J (2003), 'Anti-Proton to Proton Ratio in Au+Au Collisions at STAR', PhD thesis, Johann Wolfgang Goethe-University, Frankfurt, Germany

[171] Ulery, JG (2007), 'Two and Three Particle Jet-like correlations', PhD thesis, Purdue University, Indiana, USA